

UCSF

UC San Francisco Electronic Theses and Dissertations

Title

Implementation of Parallel Imaging Techniques for Lipid Unaliasing and Faster Acquisition for Improving Spatial Characterization of Magnetic Resonance Spectroscopic Imaging of Gliomas

Permalink

<https://escholarship.org/uc/item/4xx472qw>

Author

Ozturk Isik, Esin

Publication Date

2007-03-29

Peer reviewed|Thesis/dissertation

Implementation of Parallel Imaging Techniques for Lipid Unaliasing and Faster Acquisition
for Improving Spatial Characterization of Magnetic Resonance Spectroscopic Imaging of
Gliomas

by

Esin Ozturk Isik

DISSERTATION

Submitted in partial satisfaction of the requirements for the degree of

DOCTOR OF PHILOSOPHY

in

Bioengineering

in the

GRADUATE DIVISION

of the

UNIVERSITY OF CALIFORNIA, SAN FRANCISCO

AND

UNIVERSITY OF CALIFORNIA, BERKELEY

Copyright 2007

by

Esin Ozturk Isik

Dedicated to
Aysel and Muzaffer Ozturk
and
Cem Cemal Isik

Acknowledgements

To Sarah Nelson, for accepting me into the Bioengineering program as a student in her laboratory, being my mentor and role model, guiding me at every level of my Ph.D. study, teaching me so much about being a good researcher and supporting all my decisions in my personal life,

to Janine Lupo and Suchandrima Banerjee, for being great friends and sharing lots of laughter, research and ideas for the past five years,

to Michael Lee, for always supporting and advising me not only about research but life in general,

to Yan Li, for being like a sister, sharing Caltrain rides and ideas,

to Jason Crane, for providing support in my research and his friendship,

to Joseph Osorio, Inas Khayal, Radhika Srinivasan, Ilwoo Park, Rebeca Choy, Forrest Crawford, Suja Saraswathy, Pieter Pels, Kate Hammond, Paul Di Camillo, Pamela Jackson, Helene Ratiney, Matt Zierhut, Colleen Mcgue and Wei Bian, for creating a friendly and peaceful yet fun work environment,

to Meredith Metcalf, Cornelius von Morze, Roland Krug, Julio Gamio-Caraballido, Tim Dunn and Jeffrey Berman, for their help in various steps of my study and friendship,

to Annette Chan, Joonmi Oh, Xiaojuan Li and Aubrey Lau, for helping me adjust to my new lab with their warm welcome and support,

to Sue Noworolski, for her help in preparing for my qualifying exam with her smart insight of MR theory and her friendship,

to Duan Xu and Albert Chen, for their help with pulse sequence development,

to Eric Han, for his helpful insights into the imaging system,

to Sharmila Majumdar and Soonmee Cha, for sitting in my quals committee and reading my thesis always with a positive attitude and smile,

to Dan Vigneron, for being my advisor in the Bioengineering program and sitting in my quals committee,

to John Kurhanewicz and Bruce Hasegawa, for teaching me about MR spectroscopy and radionuclide imaging, for their discussions during my qualifying exam preparation, and participating in my quals committee,

to Andrea Pirzkall and Susan Chang, for their help with clinical questions, useful discussions, and support,

to Bert Jimenez, for our fun history discussions, organizing the scans for my studies and his friendship,

to Niles Bruce and Evelyn Proctor, for their help in making the patient scans possible,

to my parents, Aysel and Muzaffer Ozturk, and my sister, Eda, for their love, encouragement and support no matter how far away we have been,

and to my husband, Cem Cemal Isik, who brightens my life with his continuous love, friendship and smile,

THANK YOU.

Grant funding for this thesis project was provided by the UC Discovery grants LSIT01-10107 and ITL-BIO04-10148 funded in conjunction with GE Healthcare, and NIH grants R01 CA059880, P50 CA97257 and P50 CA9729.

Abstract

Implementation of Parallel Imaging Techniques for Lipid Unaliasing and Faster Acquisition for Improving Spatial Characterization of Magnetic Resonance Spectroscopic Imaging of Gliomas

by

Esin Ozturk Isik

Magnetic resonance imaging (MRI) tools have been commonly utilized in the management of patients diagnosed with gliomas. Functional and metabolic MRI techniques have been proposed to add information regarding the tissue characteristics and biochemistry for better tumor localization, treatment planning and follow up of the disease. Magnetic resonance spectroscopic imaging (MRSI) is a metabolic imaging technique used to analyze brain tissue chemistry.

MR spectroscopic and diffusion imaging were utilized to study the spatial characteristics of grade 3 gliomas. The contrast enhancing regions appeared to be the most malignant tumor area in contrast enhancing patients, and choline to NAA index (CNI) greater than four regions appeared to be the most malignant focus in the non-enhancing patients.

The presence of lipids within MR spectra in sub-regions of tumor may indicate cellular membrane breakdown due to cell death. Another potential source of lipids is from subcutaneous fat that may be aliased into the spectral field of view due to chemical shift artifact and low bandwidth of the selection pulses. It is therefore important to

identify the origins of lipid resonances, either artifact or from pathologic state, for accurate assessment of the disease state. A post-processing method based on the sensitivity encoding (SENSE) technique was developed to reduce lipid contamination in the spectra to increase the spectral quantification accuracy.

The major limitation of acquiring spectral data for gliomas is the long data acquisition time. The possibility of combining ellipsoidal sampling with two parallel imaging techniques, SENSE and generalized autocalibrating partially parallel acquisitions (GRAPPA), was investigated using simulations. Two fast data acquisition schemes, SENSE and ellipsoidal SENSE, were developed to scan patients at 3T within 9 and 4.5 minutes, respectively. Both SENSE and ellipsoidal SENSE sampling resulted in clinically interpretable spectra with high correlation to the ellipsoidal sampling.

The results of this dissertation suggest that magnetic resonance spectroscopic imaging is an important technique for spatially characterizing brain tumors that can be acquired in a shorter time to obtain equivalent disease related information. It is expected that shorter scan times will result in less patient discomfort and motion artifacts, and will increase the scanner throughput.

Approved by Sarah J. Nelson, Dr. rer.Nat.



3/23/07
date

Table of Contents

Acknowledgements.....	iv
Abstract.....	vii
List of Tables	xii
List of Figures.....	xiv
1 . Introduction.....	1
2 . Background	5
Neuroanatomy.....	5
<i>Brain Gross Anatomy.....</i>	5
<i>Cell Types of the Brain</i>	8
<i>Blood Brain Barrier.....</i>	9
<i>Brain Tumors</i>	9
Magnetic Resonance Imaging.....	11
<i>NMR Magnetization.....</i>	12
<i>Excitation and Signal Detection</i>	14
<i>Relaxation</i>	16
<i>Signal Localization</i>	18
<i>Pulse Sequences</i>	20
Spin Echo Imaging.....	20
Gradient Echo Imaging.....	22
<i>MR Image Contrast.....</i>	23
<i>MR Imaging of Brain Tumors.....</i>	25
Magnetic Resonance Spectroscopic Imaging	27
<i>MRSI Principles.....</i>	27
Chemical Shift	28
Spin Coupling	29
<i>MRSI Data Acquisition</i>	30
Point Resolved Spectroscopy (PRESS)	30
Chemical Shift Selective (CHESS) Pulses	31
Spectral Spatial Pulses and Very Selective Suppression (VSS) Pulses.....	32
Band Selective Inversion with Gradient Dephasing (BASING).....	33
<i>MRSI Data Reconstruction</i>	35
<i>MRSI Peaks for Brain Tumors.....</i>	36
3 . Spatial Characteristics and Correlations of Newly Diagnosed Grade 3 Gliomas Using MRI, 3D MR Spectroscopic Imaging, and Diffusion Tensor Imaging.....	40
Rationale.....	40
Materials and Methods	42
<i>Diffusion Tensor Imaging.....</i>	42
<i>Patient Population</i>	44
<i>Data Acquisition</i>	45
<i>Data Reconstruction</i>	45

<i>Regions</i>	46
<i>Statistical Analysis</i>	46
Results.....	48
<i>Tumor Spatial Extent and Coverage</i>	48
<i>Overlap of Anatomical Tumor Regions and Metabolically Abnormal Areas</i>	49
<i>Spectral and Diffusion Parameters within Anatomical Tumor Regions</i>	49
<i>Spectral and Diffusion Parameters within Metabolically Abnormal Areas</i>	55
<i>Spectral and Diffusion Parameter Correlations</i>	57
Discussion.....	58
4 . Unaliasing Lipid Contamination for MR Spectroscopic Imaging of Gliomas at 3T Using SENSE	62
Rationale.....	62
Theory.....	63
<i>Sensitivity Encoding (SENSE)</i>	63
<i>Chemical Shift Artifact and Lipid Aliasing at 3T</i>	69
<i>Lipid Unaliasing Using SENSE</i>	70
Methods	73
<i>Data Acquisition</i>	73
<i>Data Simulations</i>	75
<i>Data Processing</i>	75
Results.....	78
Discussion.....	82
5 . Quantitative 3D SENSE MRSI in Comparison to Ellipsoidal MRSI of Gliomas at 3T	89
Rationale.....	89
Materials and Methods	90
<i>Data Acquisition</i>	90
<i>Data Reconstruction and Analysis</i>	91
Results.....	92
Discussion.....	98
6 . Simulated Ellipsoidal SENSE and Ellipsoidal GRAPPA MRSI of Gliomas at 3T	100
Rationale.....	100
Materials and Methods	100
<i>Generalized Autocalibrating Partially Parallel Acquisitions (GRAPPA)</i>	100
<i>Data Acquisition and Preparation</i>	101
<i>Data Processing and Analysis</i>	102
Results.....	105
Discussion.....	109
7 . Ellipsoidal SENSE with Effective 9 Fold Scan Time Reduction for Small FOV 3D MR Spectroscopic Imaging of Glioma Patients at 3T	111
Rationale.....	111
Materials and Methods	112

<i>Data Acquisition</i>	112
<i>Data Reconstruction and Analysis</i>	114
Results.....	116
Discussion.....	121
8 . Summary	123
References	127

List of Tables

Table 2.1. WHO Classification Criteria for Astrocytomas.....	10
Table 2.2. T1 and T2 relaxation values for the gray and white matter at 1.5 T and 3T.....	17
Table 2.3. Image contrast of a spin echo sequence based on TE and TR.....	24
Table 2.4 Brain metabolites' chemical structures and chemical shifts.....	37
Table 3.1. Differences of spectral and diffusion parameters between NAWM, CEL, and NEL.....	51
Table 3.2 Differences of lactate between NAWM, CEL and NEL, and between NAWM and CNI abnormal regions.....	54
Table 3.3. Differences of spectral and diffusion parameters in NAWM and CNI ≥ 2 regions.....	55
Table 3.4. Correlations of diffusion and spectral parameters.....	57
Table 4.1. Total normalized lipid heights from the aliased and unaliased simulated spectra.....	80
Table 5.1 Time and g factor corrected median SNR ratios of the full and regularized and unregularized SENSE and ellipsoidal spectra in the volunteers.....	94
Table 5.2. Median Cho/NAA values in the regions, and the p values of the Cho/NAA difference between NAWM and FL and NAWM and CE regions for the patients.....	96
Table 5.3. Median ratio of the median values of Cho, Cr and NAA in FL versus NAWM, and CE versus NAWM regions as calculated from the ellipsoidal and SENSE spectra and their correlations for the patients.....	97
Table 6.1. SNR values of the spectral metabolites for the original, GRAPPA and SENSE ellipsoidal datasets for the patients.....	105
Table 6.2. SNR ratios of the metabolites calculated from the original, SENSE and GRAPPA ellipsoidal spectra for the patients.....	105
Table 6.3. Geometry factor values for the SENSE reconstruction in tumor and normal regions for the patients and the whole PRESS box region for volunteer and phantom.....	106
Table 6.4. Number of voxels that have an absolute lipid height bigger than the absolute NAA height for the three different data types in the normal regions.....	106

Table 6.5. Median Cho/NAA values within the normal and tumor regions for patients, and within the whole PRESS box for the volunteer and phantom data as calculated from the original, GRAPPA and SENSE spectra.	107
Table 6.6. Spearman rank correlation coefficient values for the Cho/NAA ratio correlation in the normal and tumor regions between original and GRAPPA and original and SENSE spectral results.	107
Table 7.1. The effect of regularization in terms of SNR, median Cho/NAA and the number of lipid contaminated voxels for the simulated patient data.	116
Table 7.2. The SNR of metabolites and average SNR ratio of the ellipsoidal and ellipsoidal SENSE along with the median g factor values and expected SNR ratio for empirical volunteer and patient data.	117
Table 7.3. Median Cho/NAA ratios for ellipsoidal and ellipsoidal SENSE spectra, the Spearman rank correlation coefficient and corresponding p-value of this ratio over the whole PRESS box, and the number of lipid contaminated voxels.....	118

List of Figures

Figure 2.1. Main anatomical sections of the brain.....	5
Figure 2.2. FID signal and its Fourier transform.	15
Figure 2.3. The relaxation curves for the transverse and longitudinal magnetization. .	17
Figure 2.4. Spin echo pulse sequence timing diagram.....	21
Figure 2.5. Gradient echo pulse sequence timing diagram.....	22
Figure 2.6. Example proton density (a), T1 (b) and T2 (c) weighted MR images.	24
Figure 2.7. T1 post-contrast (a) and T2 weighted (b) images of a patient diagnosed with glioma.	26
Figure 2.8. PRESS pulse sequence.	30
Figure 2.9. A CHESS pulse with the PRESS sequence.....	32
Figure 2.10. The VSS pulses with spectral spatial pulses.....	33
Figure 2.11. Dual BASING scheme incorporated into the PRESS sequence.....	34
Figure 2.12. Typical normal and tumor spectra for brain tissue.....	38
Figure 2.13. T1 weighted MR image along with the spectra located at the white grid for a glioma patient.....	38
Figure 2.14. Lipid and lactate presence within a brain tumor.	39
Figure 3.1. Diffusion weighted spin echo sequence diagram.	42
Figure 3.2. The regions analyzed for grade 3 gliomas.....	47
Figure 3.3. Box plots of median spectral peak heights for all the patients.....	50
Figure 3.4. Box plots of median CNI values for all the patients.	50
Figure 3.5. Box plots of median normalized ADC and ANI values for all the patients.....	51
Figure 3.6. Presence of lactate within the spectra of a grade 3 oligoastrocytoma.	53
Figure 3.7. Box plots of median lactate levels.....	53
Figure 4.1. The coil sensitivity images of a brain slice acquired by the eight channel head coil.....	64

Figure 4.2. Aliasing scheme for SENSE data acquisition.	66
Figure 4.3. Aliasing concept in an MR image.	66
Figure 4.4. Example of the lipid aliasing problem in MR spectra.....	71
Figure 4.5. Example of lipid unaliasing for a voxel..	72
Figure 4.6. A slice from the coil sensitivity images before (a) and after (b) the coil sensitivity map correction.	77
Figure 4.7. Geometry factor maps before (a) and after (b) masking the object region, and after the full coil sensitivity map correction (c).....	79
Figure 4.8. An example simulated spectra before (a) and after (b) lipid unaliasing.....	81
Figure 4.9. Lipid unaliasing for the phantom case.....	82
Figure 4.10. Lipod unaliasing example for a glioma patient.	83
Figure 5.1. MR spectra acquired by ellipsoidal sampling and SENSE with R=4.	93
Figure 5.2. Median signal to noise ratios of the major brain metabolites calculated from the three different spectra in the volunteers.....	94
Figure 5.3. Linear fit of the NAA intensities calculated from a volunteer’s SENSE versus full spectra.....	95
Figure 5.4. MR spectra of a patient diagnosed with glioblastomamultiforme acquired with the ellipsoidal and SENSE sampling.	98
Figure 6.1. The k -space sampling patterns for the ellipsoidal, ellipsoidal SENSE, and ellipsoidal GRAPPA approaches.	103
Figure 6.2. SENSE, original and GRAPPA ellipsoidal spectra for a phantom.	108
Figure 6.3. SENSE , original and GRAPPA ellipsoidal spectra for a glioma patient.	109
Figure 7.1. Sampling schemes for the ellipsoidal and ellipsoidal SENSE for a $16 \times 16 \times 8$ k - space array..	113
Figure 7.2. Median Cho to NAA ratio for the patients within normal and tumor regions as calculated from ellipsoidal and ellipsoidal SENSE spectra.....	119
Figure 7.3. Ellipsoidal and ellipsoidal SENSE spectra of a volunteer.....	120
Figure 7.4. Ellipsoidal and ellipsoidal SENSE spectra of a glioma patient.....	121

1 . Introduction

Brain cancer is a debilitating disease with median survival of about 1 year for the highest grade lesions (1). The incidence rate of brain tumors is increasing with an estimated 20,500 new cases of primary brain tumors detected each year in the United States alone (1). Ninety percent of primary brain tumors in adults older than 45 are gliomas, which originate from the glial cells that are the support cells for neurons. Gliomas usually infiltrate into the adjacent normal brain tissue, making it impossible to demarcate their margins. Improved localization and characterization of brain tumors are vital for selecting the most effective treatment, which includes surgical resection, radiation therapy and chemotherapy, and guiding the extent and/or focus of the therapy.

Magnetic resonance imaging (MRI) is the most commonly used clinical imaging technique for localizing brain tumors. Pre- and post-contrast T1 weighted imaging and T2 weighted fluid attenuated inversion recovery (FLAIR) are the two common types of magnetic resonance (MR) imaging sequences used for tumor localization. Tumor is usually seen as a hypointense area in the T1-weighted images before the intravenous injection of a contrast agent, such as gadolinium diethyltriaminepentaacetic acid (Gd-DTPA). After the contrast administration, Gd-DTPA can leak into the areas of the brain where the blood-brain barrier (BBB) is disrupted, resulting in hyperintense regions due to the shortening of T1 of the tissue. T2 weighted FLAIR images reveal hyperintensity in areas of tumor, edema and necrosis due to increased water content. Although these MR images are highly sensitive in tumor detection, the true margin of

tumor border may be difficult to assess especially in infiltrative tumors such as glioma. In addition to having poorly defined margins, gliomas are known to be heterogeneous, and it is important to predict the most malignant portion of the lesion to direct surgery or radiation therapy. It is also necessary to identify tumor regions that extend beyond contrast enhancement or T2 hyperintensity, in order to take them into account for treatment planning.

Molecular imaging techniques have been proposed to provide information that will help in better localizing and characterizing gliomas. Volumetric MRI and three dimensional MR spectroscopic imaging (3D-MRSI) are non-invasive techniques that provide both high resolution anatomical images of the brain and metabolic maps for better tumor localization and quantitative assessment of the brain metabolism. The combination of MRI and MRSI has been suggested as being more effective in tumor localization, staging, assessment of progression and treatment planning and response than MR imaging alone. Long echo time 3D-MRSI provides arrays of spectra for *in vivo* brain applications that are characterized by three major metabolite peaks in healthy brain tissue: namely the singlets of choline (Cho), total creatine (Cr) and N-acetyl aspartate (NAA). An increase in the level of choline provides a marker for excessive cell growth or cell membrane turnover. The peak due to creatine and phosphocreatine reflects bioenergetics processes due to their role as a phosphate recipient or donor for ATP or ADP, and is thought to represent the energetic status of the cell. NAA is the most abundant amino acid in brain that is synthesized in neurons, and is hypothesized to have a role in the removal of intracellular water from neurons. NAA is an indicator of the neuronal viability that is usually observed to be smaller in

the tumors than in the areas of normal brain. Singlet lipid and doublet lactate peaks are two other resonances that can be observed in the disease state. Lactate is a byproduct of anaerobic glycolysis, and is expected to be present in areas with poor oxygenation. Lipid is present in the lipid bilayer of the cell membrane in normal brain cells, as well as in the bone marrow of skull, and adipose tissue of the scalp. Lipid that is observed in the spectra may indicate cellular membrane breakdown due to necrosis.

The wider availability of high field scanners and multi-channel radiofrequency (RF) surface coils have increased the sensitivity and accuracy of MR imaging and spectroscopy of brain tumors through higher signal-to-noise ratio (SNR) and improved spectral resolution. Increased spectral dispersion at high field results in less overlap between different peaks and simplifies the appearance of the spectrum. Besides the increase in SNR due to the higher field strength, surface coils receive the MR signal from a smaller area and at a closer distance to the anatomy thereby decreasing noise and resulting in higher SNR. Increased SNR can also be projected to improved spatial or temporal resolution. An issue to be addressed concerning the surface coils is their inhomogenous reception profile which drops sharply with the distance to the coil. Reconstruction of MR image or spectral data acquired with multi-channel RF coils requires a weighted combination algorithm that takes into account the spatially varying coil sensitivity profiles. These coil sensitivity maps can be acquired as low resolution proton-density weighted MR images of the anatomy of interest from each coil element using a fast imaging sequence and then incorporated into the reconstruction routines.

The goal of this project was to apply magnetic resonance imaging and spectroscopic imaging techniques to understand the characteristics of gliomas and

produce new means of acquiring and reconstructing spectroscopic data for faster and more accurate imaging. This thesis is divided into eight main chapters consisting of

Chapter 2, which provides background material for brain anatomy and tumors and MR imaging and spectroscopic imaging principles;

Chapter 3, which explains the application of MR imaging and spectroscopic imaging tools to understand the regional characteristics of Grade 3 gliomas (2);

Chapter 4, which describes a novel application of a parallel imaging technique called SENSE to reduce the lipid contamination in spectral images for more accurate quantification (3);

Chapter 5, which details the acquisition and reconstruction of fast spectroscopic images using the SENSE theory and its application to gliomas and compares the results to the clinically accepted fast ellipsoidal spectroscopic imaging (4,5);

Chapter 6, which describes simulation studies of two novel fast spectroscopic data acquisition and reconstruction methods called ellipsoidal SENSE and ellipsoidal GRAPPA based on the combination of ellipsoidal sampling and two parallel imaging theories (6);

Chapter 7, which describes the clinical application of the ellipsoidal SENSE method for acquiring three dimensional spectroscopic imaging of the brain tumor patients in less than five minutes, and compares it to the clinically accepted ellipsoidal spectroscopic imaging (7,8); and

Chapter 8, which summarizes all the results of this study, its impact on clinical patient management and proposes future work that may be relevant.

2 . Background

This chapter provides basic information about neuroanatomy and brain tumors followed by a review of the fundamental principles of magnetic resonance imaging (MRI) and magnetic resonance spectroscopic imaging (MRSI). The application of MRI and MRSI for imaging brain tumors is also discussed.

Neuroanatomy

Brain Gross Anatomy

The brain is the most important organ of our body despite its small size of only around 1400 grams. It controls our thoughts, memory, emotions, motor activities, and many body processes. The brain is highly vascular receiving 25% of the cardiac output and 1000 cc blood through the brain arteries every minute. The brain is composed of 3 main sections; the cerebrum, cerebellum and the brain stem. The cerebrum is divided into two lateral hemispheres and each hemisphere contains 4 main anatomical sections that are the frontal lobe, parietal lobe, occipital lobe and the temporal lobe. Figure 2.1 shows the main anatomical structures of the brain.

The frontal lobe is located anterior to the central sulcus, and is the center for higher cognitive functions like emotions, behavior, planning, and problem solving. The frontal lobe hosts the primary motor area and premotor area that control movement. Another important area of the frontal lobe is the Broca's area, which is the motor area for speech.

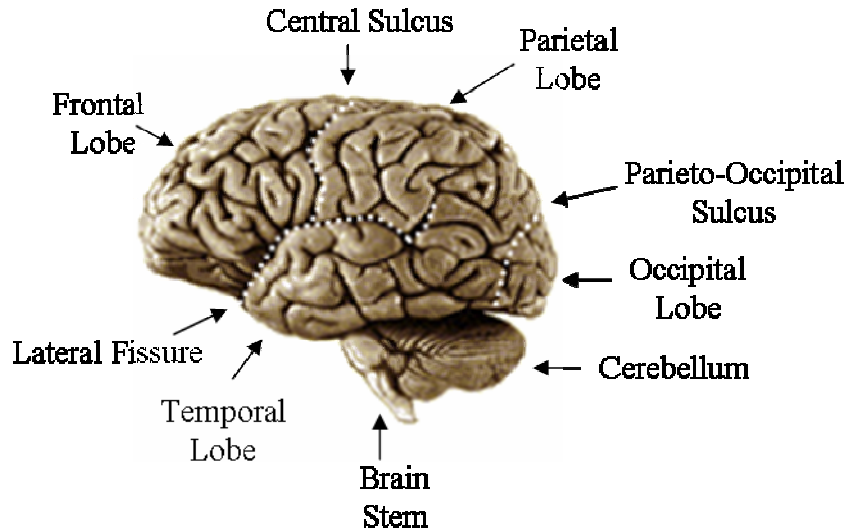


Figure 2.1. Main anatomical sections of the brain. Adapted from Canadian Institutes of Health Research: Institute of Neurosciences, Mental Health and Addiction, http://thebrain.mcgill.ca/flash/a/a_01/a_01_cr/a_01_cr_ana/a_01_cr_ana.html (9).

Two parietal lobes are located between the frontal lobe and occipital lobe posterior to the central sulcus on the two hemispheres of the brain. The parietal lobe hosts the primary sensory area that controls the general body sensation. Two temporal lobes are located ventral to the lateral fissure. The temporal lobe hosts the gyri of Heschl, which is the primary auditory area and the Wernicke's area, which is involved in the comprehension of spoken language. The occipital lobe is located at the posterior side of the brain, and it hosts the primary visual area.

The cerebellum is located between the occipital lobe and the brain stem, and takes a role in the initiation, control and integration of motor activity, as well as the balance and posture. The cerebellum is also thought to take part in the modulation of thought, planning, learning, memory and language. The brain stem is the lower part of the brain adjoining the spinal cord. The brain stem is divided into three main sections called the midbrain, pons and the medulla oblongata. The midbrain is located at the rostral part

of the brain stem. The midbrain is involved in functions such as the vision, hearing, eye movement, and body movement. The pons contains the nerve fibers connecting two sides of the cerebellum, and it takes a role in coordinating movements involving right and left sides of the body. The medulla oblongata is located adjacent to the spinal cord and transmits ascending and descending nerve fibers between the spinal cord and the brain. The medulla oblongata also controls respiration, heart contraction, artery dilation, sneezing, swallowing and vomiting.

The brain is protected by three barriers which are from outside to inside the skull, meninges and cerebrospinal fluid (CSF). The bony skull is the main protection against trauma to the brain. The meninges are composed of three layers which are the dura mater, arachnoid mater and pia mater. The dura mater is a tough, fibrous connective tissue that has three parts called the falx cerebri, tentorium cerebelli and falx cerebelli separating the components of the brain. The falx cerebri separates the two cerebral hemispheres. The tentorium cerebelli is a fold of the dura mater that is stretched over the cerebellum like a tent and separates the posterior part of the brain from the cerebellum. The falx cerebelli separates the two cerebellar hemispheres at the inferior surface. The arachnoid mater is the middle layer of the meninges, and the pia mater is a thin membrane surrounding the brain that hosts the blood vessels of the brain. The final barrier of the brain is the cerebrospinal fluid, which is a clear and colorless fluid, which protects and cushions the brain. The CSF collects the waste from the nerve and glial cells and also maintains the composition of the extracellular fluid of the brain. Another role of the CSF is the transmission of hormones and neurotransmitters.

Cell Types of the Brain

Nerve and glial cells are the two main groups of cells found in the brain. The nerve cells, or neurons, are the structural and functional unit of the nervous system. The glial cells are the metabolic and structural support unit of the nervous system. It is estimated that there are 10 times as many glial cells as the neurons (10). A neuron has a cell body and its processes which are called axon and dendrites, respectively. The neuronal cell body sizes vary from 4 to 125 μm depending on the location of the nerve cell (10). The axon and dendrites take parts in the conduction of electric impulses via ion movement between neurons, supplying the network of communication.

The glial cells are grouped into four types, which are the astrocytes, oligodendrocytes, ependymal cells and microglia. The astrocytes are the largest glial cells and their processes attach to and completely cover the outer surface of capillaries and the pia mater. The oligodendrocytes take a role in the production of a lipoprotein called 'myelin' that covers the axons in some nerve cells. The myelin functions as an electrical insulator and ensures efficient nerve conduction. The parts of the brain that have myelinated nerve cells appear white and are called the 'white matter'. On the contrary, the cortex of the brain contains mostly the nerve cell bodies without myelination and appears gray. These parts of the brain are called the 'gray matter'. The ependymal cells line the central canal of the spinal cord and the ventricles of the brain. The microglia are the macrophages of the central nervous system, and they get activated in the event of a destructive lesion to clean the cell debris.

Blood Brain Barrier

The blood brain barrier (BBB) is a barrier between the brain tissue and the blood capillaries that protects the brain by restricting the entry of molecules to the brain. This barrier blocks all molecules except those that cross cell membranes by means of lipid solubility such as oxygen, carbon dioxide, ethanol and steroid hormones and those that are allowed in by specific transport systems such as sugars and some amino acids. The blood brain barrier is composed of capillary endothelial cells with tight junctions in between them, capillary basement membrane and the astrocytic foot processes adjacent to the capillary.

Brain Tumors

A brain tumor, which is any intracranial mass either created by an abnormal growth of cells that are local to the brain or by metastasizing from cancers located in other organs, is a life-threatening disease with an estimated 20,500 new occurrences every year within the United States alone (1). There is no screening system available for diagnosing brain tumors in the early stages. Brain tumors are typically diagnosed after the patient develops some symptoms including headaches, seizures, cognitive or personality changes, eye weakness, nausea or vomiting, speech disturbances, or memory loss. The survival of the patients is dependent on their age and the type and location of the tumor. It is estimated that approximately 12,740 people will die from these malignant tumors in 2007 and the median survival for the highest grade of the brain tumors is only a year (1).

Metastatic brain tumors occur in 10 to 15% of persons with cancer and are the most common type of brain tumors (1). Primary brain tumors originate from the cells

of the brain including neurons (neuroblastoma, ganglioneuroblastoma and ganglioneuroma), glial cells (astrocytoma, oligodendroglioma and ependymoma), myelin producing Schwann cells (schwannoma), meninges (meningioma), pituitary gland (pituitary tumors) and the pineal gland (pineal tumors). Ninety percent of primary brain tumors in adults older than 45 are gliomas, which originate from the glial cells that are the support cells for neurons. The astrocytoma that originates from star shaped astrocytes is the most common type of gliomas. The oligodendroglioma is another common type of gliomas originating from oligodendrocytes. The oligodendrogliomas have better prognosis than astrocytomas because they are chemo-sensitive. Temozolomide, which is a chemotherapy drug that interferes with the DNA in cancer cells and prevents their growth, has been shown to prolong the survival in oligodendrogliomas (11).

The astrocytomas are histologically categorized into four grades according to World Health Organization (WHO) II classification system. Table 2.1 lists the criteria that are used for this classification.

Table 2.1. WHO Classification Criteria for Astrocytomas.

	WHO II Grade	Criteria
pilocytic astrocytoma	I	none of the criteria satisfied
astrocytoma	II	one criterion: usually nuclear atypia
anaplastic astrocytoma	III	two criteria: usually nuclear atypia and mitosis
glioblastoma multiforme	IV	three or four criteria: usually nuclear atypia, mitosis and necrosis

The pilocytic astrocytoma is slow growing and its borders are well defined. It most often occurs in children and it is considered benign. The grade II astrocytoma grows

faster than grade I tumors and its borders are usually not well defined. Grade II astrocytomas usually have nuclear atypia and they are non-invasive. The anaplastic astrocytoma grows faster than grade II tumors and it has mitosis and nuclear atypia. Grade III astrocytomas are invasive. The glioblastoma multiforme is the most malignant and invasive astrocytoma, and necrosis is the defining factor of grade IV astrocytomas.

At present, brain tumors are treated by surgery, radiation therapy and chemotherapy used either individually or in combination. Treating brain tumors with chemotherapy is difficult, because the blood brain barrier blocks the entry of most chemotherapeutic agents into the brain. Temozolomide is such an exception that can cross the BBB. Also, the blood brain barrier is broken in some tumors allowing some entry of the drugs. The standard treatment for grade I and II astrocytomas is surgery to resect as much of the tumor as possible. If there is remaining tumor or if the tumor is inoperable then chemotherapy and/or radiation therapy are given. For small children, chemotherapy is preferred over radiation therapy to avoid damage to the developing brain. The high grade tumors (grade III and IV) are treated with surgery followed by radiation therapy or a combination of radiation therapy and chemotherapy.

Magnetic Resonance Imaging

Improved localization and characterization of brain tumors are vital for selecting the most effective treatment and guiding the extent and focus of the therapy. Magnetic resonance imaging (MRI) is a non-invasive tomographic imaging technique that has been commonly used for imaging the brain tumors. Magnetic resonance imaging is

based on the NMR phenomenon observed in bulk matter by Felix Bloch and Edward Purcell in 1946. Paul Lauterbur later developed spatial information encoding principles, originally called zeugmatography, in 1972 which enabled image formation using NMR signals. This section will briefly describe the NMR signal generation, signal detection, some parameters affecting the signal intensity and the MR image formation. For more information about the MR theory, the readers can consult to references (12-14).

NMR Magnetization

Magnetic resonance imaging is based on a fundamental property of nuclei of atoms which states that nuclei with odd atomic weights and/or atomic numbers possess an angular momentum J called 'spin'. Nuclei with an odd mass number have half integral spin, an even mass number and even charge number have zero spin and an even mass number but an odd charge number have integral spin. The nucleus of the hydrogen atom, which has only one proton, is an example nucleus with $\frac{1}{2}$ spin. A nucleus that has a nonzero spin rotates around its own axis creating a microscopic magnetic field around it called a 'nuclear magnetic dipole moment', μ . The magnitude of this dipole moment is related to the spin as

$$\mu = \gamma J , \quad (2.1)$$

where γ is a physical constant known as the 'gyromagnetic ratio'. The gyromagnetic ratio is equal to $42577400 \text{ HzT}^{-1}$ for the proton. The direction of μ is arbitrary in the resting state resulting in no net magnetic field from the object.

It is possible to create a macroscopic magnetic field from an object by aligning up the spin vectors. This can be accomplished by placing the object inside a strong external static magnetic field, B_0 . In the presence of a strong magnetic field, spins precess about the axis of the B_0 direction with a known angular frequency called Larmor frequency, ω_0 , which is estimated as

$$\omega_0 = \gamma B_0. \quad (2.2)$$

Nuclei of ^1H and ^{31}P resonate at 42.58 MHz and 11.26 MHz respectively in the presence of a 1T field strength.

The spins of a $\frac{1}{2}$ spin system take two possible orientations in the presence of a B_0 , which are parallel or anti-parallel to the field. There is an energy difference between these two states that can be calculated as

$$\Delta E = h\gamma B_0, \quad (2.3)$$

where $h = 6.626 \times 10^{-34}$ Js is the Planck's constant.

The anti-parallel state requires a higher energy, and it is less preferred. As a result, a slightly higher number of spins are found in the parallel to the field state. The relative number of spins between the upper and lower energy states can be calculated as

$$\frac{N_{up}}{N_{down}} = e^{(-\Delta E/kT)}, \quad (2.4)$$

where $k = 1.381 \times 10^{-23}$ JK⁻¹ is the Boltzman's constant, T is the temperature of the spin system in Kelvin (K) (T=310 K for the body temperature), N_{up} is the number of spins that are aligned parallel and N_{down} is the number of spins that are aligned anti-parallel to the external magnetic field.

Although there is a small difference between the number of spins in the parallel and anti-parallel state, the population difference between the two spin states is enough to generate a detectable magnetization, M , that can be estimated as

$$M = \frac{\gamma^2 \hbar^2 B_0 N}{4kT}, \quad (2.5)$$

where N is the total number of spins.

The amplitude of the magnetization is directly proportional to the spin density and the strength of the external magnetic field. Effectively, about three in a million protons in an object at 1T field strength is activated for generation of the nuclear magnetic resonance (NMR) magnetization (12) that is used to produce high definition MR images of the body, and this number is tripled at 3T.

Excitation and Signal Detection

An oscillating magnetic field or so called radiofrequency (RF) field, $B_1(t)$, rotating in the same manner as the precessing spins can be generated by an RF coil to excite the spins and establish a coherent phase among these randomly precessing spins. The radiation energy is set to be equal to the energy difference between the spin states to create a coherent transition of spins from one state to another. Accordingly, the carrier frequency of this oscillating field, ω_{rf} , is set to be equal to the Larmor frequency. The direction of $B_1(t)$ is set perpendicular to the B_0 field. The B_0 axis will be denoted as the z axis or the longitudinal axis and the transverse direction will be called the xy axis in the rest of this chapter. The application of the $B_1(t)$ field in a perpendicular direction induces a torque on the magnetization causing M to rotate away from the static magnetic field, and results in a transverse magnetization that can be detected according

to Faraday's law of induction (13). The frequency of rotation away from the B_0 axis in the presence of B_1 can be calculated as

$$\omega_1 = \gamma B_1. \quad (2.6)$$

The angle between the tipped magnetization and B_0 is called the 'flip angle', α , and it is estimated as

$$\alpha = \int_0^{\tau} \omega_1(t) dt, \quad (2.7)$$

where τ is the duration of the RF pulse. It is common to use RF pulses that would result in 90° and 180° flip angles in MR.

The same RF coil used to generate the rotating B_1 field can be used to detect the precessing magnetization (13). The sum of the precessing transverse magnetization over the volume of the object is recorded as the MR signal. The signal detected after the application of an RF pulse is called 'free induction decay' (FID). The FID signal can be transferred into frequency domain by applying the Fourier transform. Figure 2.2 shows an example FID signal and its Fourier transform.

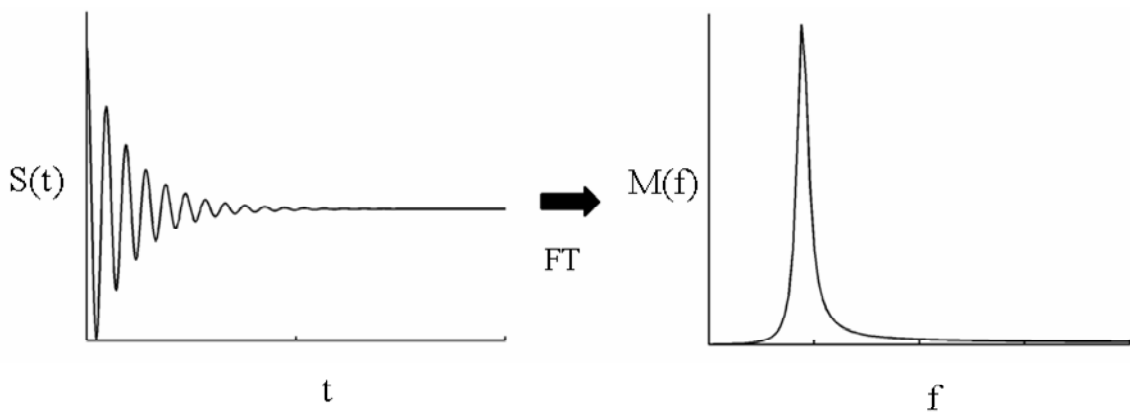


Figure 2.2. FID signal and its Fourier transform.

Relaxation

An RF pulse is turned on only for a few microseconds to milliseconds and it generates a B1 field that is much weaker than the B₀ field. Following the excitation of the spins using an RF pulse, the spins gradually lose their phase coherence and relax back to their thermal equilibrium. This results in a decay of the detectable magnetization amplitude along the xy axis and a simultaneous regrowth of the magnetization along the z axis. Time dependent amplitude of M is estimated using the Bloch equation as

$$\frac{dM}{dt} = \gamma M \times B - \frac{M_x i + M_y j}{T_2} - \frac{(M_z - M_z^0)k}{T_1}, \quad (2.8)$$

where M_z^0 is the magnetization value at the presence of B₀ only. T₁ is spin-lattice relaxation time constant that measures the time for the magnetization to grow back to 63% of its original value along the z axis. T₂ is the spin-spin relaxation time constant that measures the time for the transverse magnetization to decay to 37% of its value after the application of the RF pulse. Bloch equation can be divided into two components to estimate the magnetization intensity in the longitudinal and transverse planes as

$$\frac{dM_z}{dt} = -\frac{M_z - M_0}{T_1}, \text{ and} \quad (2.9)$$

$$\frac{dM_{xy}}{dt} = -\left(\frac{1}{T_2} + i\omega_0\right)M_{xy}. \quad (2.10)$$

The solution of these two differential equations result in the evolution of the magnetization in time as

$$M_{xy}(t) = M_{xy}^0 e^{-t/T_2} e^{-i\omega_0 t}, \text{ and} \quad (2.11)$$

$$M_z(t) = M_0(1 - e^{-t/T_1}). \quad (2.12)$$

Figure 2.3 shows a schematic representation of the transverse and longitudinal magnetization relaxation in time.

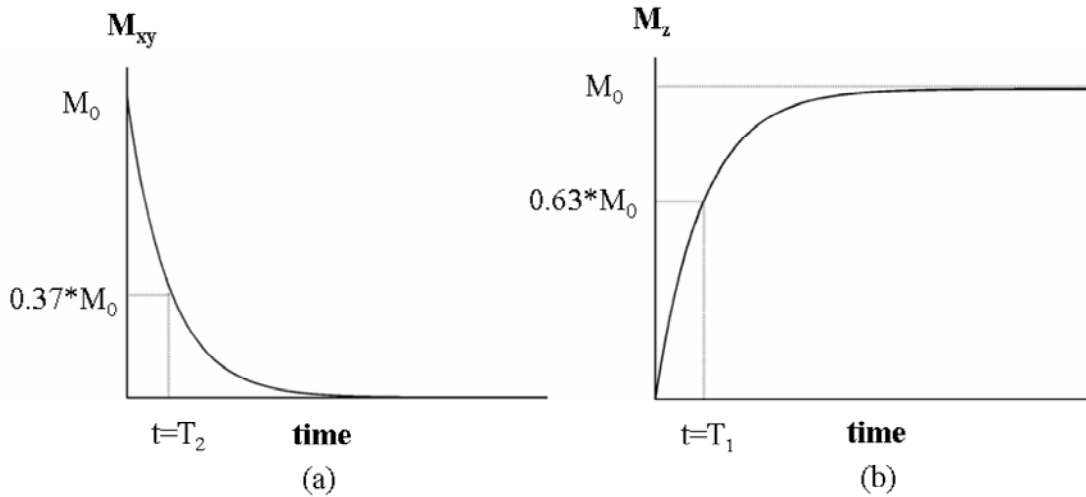


Figure 2.3. The relaxation curves for the transverse (a) and longitudinal (b) magnetization.

The relaxation constants T_1 and T_2 vary depending on the tissue type. Table 2.2 lists the measured T_1 and T_2 values for the gray and white matter at 1.5 T and 3T (15-17).

Table 2.2. T1 and T2 relaxation values for the gray and white matter at 1.5 T and 3T.

		White Matter	Gray Matter
T1	1.5T	756 ms	1200 ms
	3T	832 ms	1331 ms
T2	1.5T	80 ms	110 ms
	3T	69 ms	99 ms

The white matter was observed to have lower T1 values than gray matter, because there is a higher degree of orientation in white matter and the anisotropy of the macromolecular structures might result in an increase in efficiency of dipolar relaxation mechanisms (18). Also, white matter has lower T2 values than the gray matter due to increased blood content in the gray matter. Higher field strengths result in higher T₁ and shorter T₂ values. Higher energy exchange is required between the nuclei and the surrounding lattice at higher frequencies, and it results in longer T₁ relaxation time at higher field strength. The transverse relaxation might also be more efficient at higher field strength due to increased field inhomogeneities resulting in lower T₂ values (19).

Signal Localization

MR images are a representation of the localized magnetization vector across the imaged object. Another small magnetic field that varies with spatial position called ‘gradient field’ is used for MR localization. In the presence of such a gradient field, the spins at different locations experience a slightly different magnetic field resulting in spatial variation in resonant frequency across the object. As a result of this differential magnetic field, the frequency of the spins vary at different locations as

$$\omega(z) = \omega_0 + \Delta\omega(z) = \gamma(B_0 + G_z z), \quad (2.13)$$

where G_z is the gradient field strength along the z direction. The transverse magnetization equation can be rewritten to include the effect of a gradient as

$$M_{xy}(t) = M_{xy}^0 e^{-t/T_2} e^{-i\omega_0 t} e^{-i\gamma \int_0^t G_z r dt}. \quad (2.14)$$

The use of gradients to establish a relation between the position of spins and their precessional frequency is called ‘frequency encoding’ (14). If a gradient field is applied for certain duration and then turned off to result in a phase variation across the object, it is called ‘phase encoding’ of the spins. The time integral of a gradient field multiplied by $\gamma/2\pi$ is called the spatial frequency variable ‘ k ’ along that direction. A collection of varying gradient strengths result in different k values that are collectively referred to as the ‘ k -space’.

An RF pulse can be used in conjunction with a gradient to excite only the spins in a given range of frequencies. The position of the selected slice is determined by the center frequency of the RF pulse. The bandwidth of the RF pulse, which is the range of frequencies contained within the RF pulse, and the gradient strength determine the slice thickness as

$$\Delta z = \frac{\Delta\omega}{\gamma G_z}, \quad (2.15)$$

where $\Delta\omega$ is the bandwidth of the RF pulse and G_z is the applied gradient strength along the z direction.

After the slice selection, the localization in the transverse plane is achieved by further application of the gradients. A phase encoding gradient is turned on along y direction to create phase variations at different locations, and it results in one k_y value. After the phase encoding gradient is turned off, a frequency encoding gradient along the x direction is turned on simultaneously with the MR signal collection. This gradient is often called a ‘readout gradient’. The readout gradient causes the frequency differ at varying spatial locations, and every signal time point acquires a different k_x value. After the readout is completed, the phase encoding gradient amplitude is

changed to generate another k_y value, and the same readout gradient is applied once more time. This procedure is repeated until enough spatial frequency values are sampled to fill up the k -space.

The MR signal can be demodulated to remove the carrier frequency factor $\exp(-i\omega_0 t)$ and written as a function of k_x and k_y in time as

$$S(k_x, k_y, t) = \iint M_{xy}^0 e^{-t/T_2} e^{-i2\pi(k_x(t)x + k_y(t)y)} dx dy. \quad (2.16)$$

The magnetization value at different spatial locations can be estimated by a 2D Fourier transform of this MR signal.

Pulse Sequences

The gradient field and inherent field inhomogeneities result in differential phase across the object. It is possible to subject the spins to multiple RF and gradient pulses to manipulate the magnetization vector and the phase distribution of spins. The application of multiple RF and gradient pulses to create a specific form of NMR signal is called a ‘pulse sequence’. The pulse sequences can be designed to remove space-variant phase shifts momentarily to create a phase coherence resulting in a stronger NMR signal, called ‘echo’. This section will briefly describe two basic MR pulse sequences resulting in spin echoes and gradient echoes.

Spin Echo Imaging

The spin echo imaging uses a 90° RF pulse and a 180° RF pulse to refocus the spin phases. A 90° RF pulse is first applied to the spin system, and this pulse rotates

the magnetization into the transverse plane. After the 90° pulse is turned off, spins start to dephase due to field inhomogeneities. At time τ after the 90° RF pulse, a 180° RF pulse is applied to the spins. This pulse rotates the magnetization by 180° about the transverse axis that it is applied along. Effectively, the 180° pulse negates the spin phases. The spins continue to dephase after the 180° pulse is turned off. At time 2τ , the spins rephase, and produce a strong signal called ‘spin echo’. Figure 2.4 shows the timing diagram for a spin echo sequence. The echo time (TE), which is the time of the echo formation, and the repetition time (TR), which is the time between two consecutive 90° pulses, are also shown in Fig. 2.4. The echo time corresponds to 2τ in the preceding description.

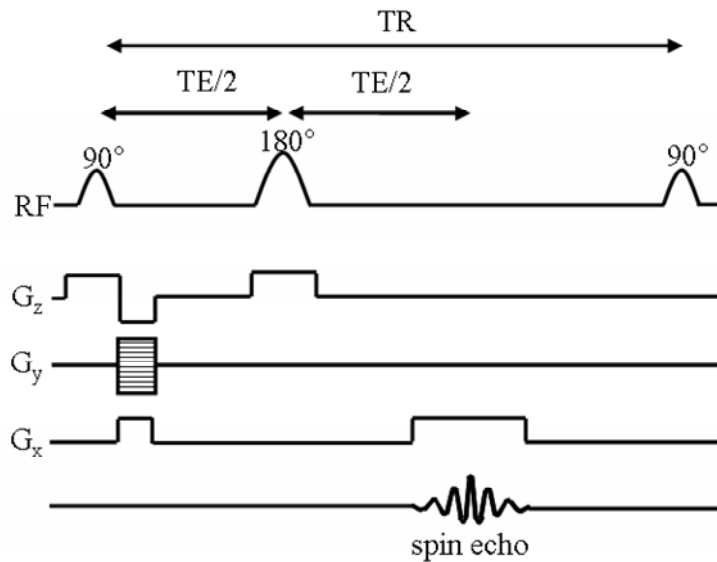


Figure 2.4. Spin echo pulse sequence timing diagram.

The amplitude of the spin echo signal, A_E , is estimated as,

$$A_E = M_{xy}^0 (1 - e^{-TR/T_1}) e^{-TE/T_2} . \quad (2.17)$$

Gradient Echo Imaging

The gradient echo imaging uses gradients that are reverse in polarity to refocus the spin phases. The gradient echo imaging does not require a 90° RF pulse to start the pulse sequence. After an RF pulse with a flip angle α applied along with slice select gradient phase encoding gradient is applied along one of the transverse axes, y . A gradient pulse in the other transverse axes, x , is applied for a time of $TE/2$. The spins start dephasing as a result of this gradient pulse. At time $TE/2$, the gradient polarity is reversed, and it starts unwinding the phase spins acquired. As a result of the polarity change, the spins precessing at a slower frequency start precessing at a higher frequency. After $TE/2$ passes from the gradient reversal, the spins regain coherence, and form a strong signal called 'gradient echo'. Figure 2.5 shows the timing diagram of a simple gradient echo sequence.

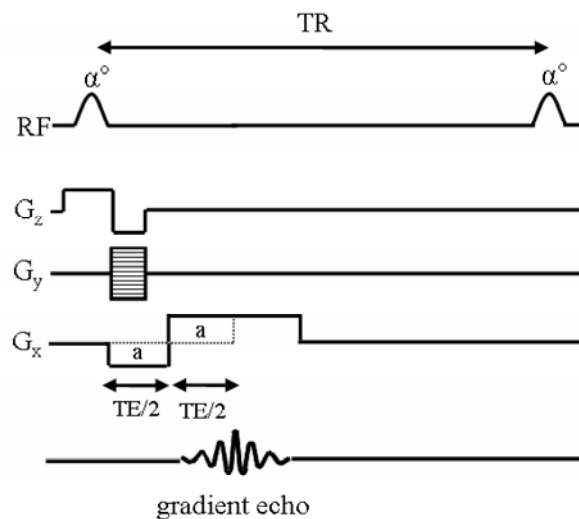


Figure 2.5. Gradient echo pulse sequence timing diagram.

The amplitude of the gradient echo signal, A_E , is estimated as,

$$A_E = \frac{M_z^0 (1 - e^{-TR/T_1})}{1 - \cos \alpha e^{-TR/T_1}} \sin \alpha e^{-TE/T_2} . \quad (2.18)$$

MR Image Contrast

MR image intensity is a multi parameter function depending on the proton density, T1 and T2 of the imaged tissue as well as the data acquisition parameters like the sequence type, TE, TR and the flip angle. The intrinsic tissue properties cannot be adjusted to increase the MR image contrast, but the sequence parameters can be modified to achieve a desired contrast or weighting in the MR image.

For the spin echo imaging, a long TR would result in the factor $(1 - \exp(-TR/T_1))$ approach 1, removing the T1 weighting. Similarly, a short TE would result in the factor $(\exp(-TE/T_2))$ approach 1, and would remove the T2 weighting. So, a short TE and long TR can be used for diminishing the T₁ and T₂ effects remaining the proton density as the main factor in the resulting echo. To achieve a T1 weighted MR image, TR can be chosen appropriately short and TE can be set short. For a T2 weighted MR image, both TE and TR can be set long. A TR value of less than 500 ms is considered to be short, and greater than 1500 ms is considered to be long for spin echo sequences (12). A TE value of less than 20 ms is considered as short. Table 2.3 lists the proper TE and TR combinations for desired image contrasts for spin echo imaging.

Table 2.3. Image contrast of a spin echo sequence based on TE and TR.

	TE	TR
Proton density weighted	short	long
T1 weighted	short	short (appropriate)
T2 weighted	long (appropriate)	long

For gradient echo imaging, the T2 weighting is adjusted similarly with the spin echo imaging. However, T1 weighting is mainly controlled with the flip angle for gradient echo imaging. For small flip angles, $\cos(\alpha)$ would approach to 1, resulting in a cancellation of the T1 terms on the denominator and numerator of the gradient echo equation. As the flip angle increases it results in a significant T1 contribution in the signal, and T1 weighting can be further adjusted by varying the repetition time.

Figure 2.6 shows examples of proton density weighted, T1 weighted and T2 weighted images of an axial slice of the human brain.

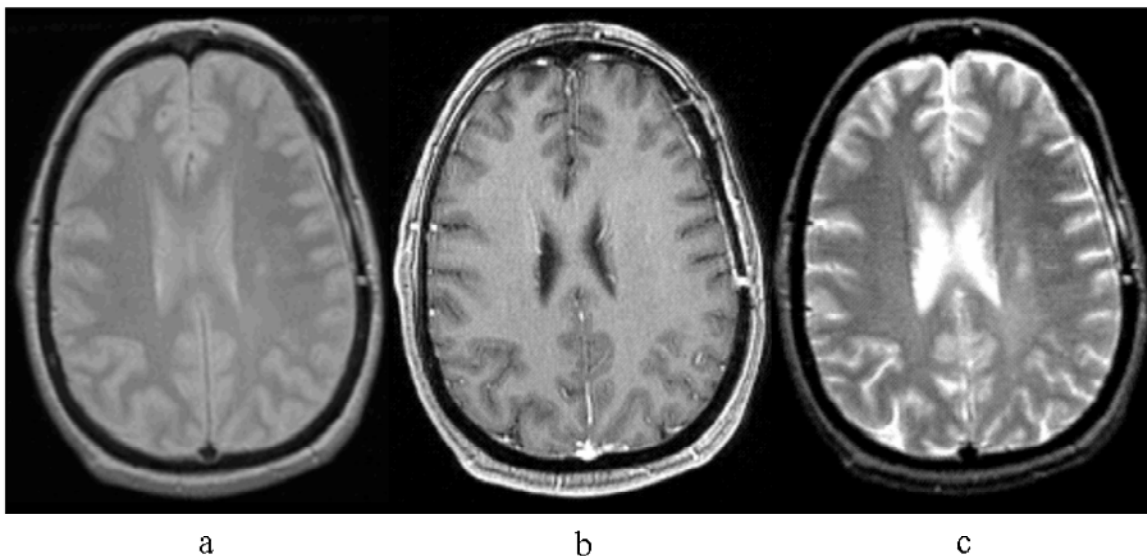


Figure 2.6. Example proton density (a), T1 (b) and T2 (c) weighted MR images.

The soft tissues have small spin density variation, so the image contrast is the least in the proton density weighted image. In the T1 weighted image, white matter has the highest intensity followed by the gray matter and cerebrospinal fluid. The white matter has the shortest T1 values resulting in the highest signal intensity according to the MR signal equation. T2 weighted image has the highest intensity in cerebrospinal fluid followed by the gray matter and white matter. The white matter has the lowest T2 values, resulting in the fastest signal relaxation in the transverse plane, and lowest signal intensity accordingly.

MR Imaging of Brain Tumors

Pre- and post-contrast T1 weighted imaging and T2 weighted fluid attenuated inversion recovery (FLAIR) are the two common types of magnetic resonance (MR) imaging sequences used for tumor localization. The gadolinium diethyltriaminepentaacetic acid (Gd-DTPA) is a common contrast agent used in MR imaging. Tumor is usually seen as a hypointense area in the T1-weighted images before Gd-DTPA injection. After the contrast administration, Gd-DTPA leaks into the areas of the brain where the blood-brain barrier is disrupted, resulting in hyperintense regions due to the shortening of T1. T2 weighted FLAIR images are acquired with an inversion recovery spin-echo sequence. The inversion recovery spin-echo sequence starts with an additional 180° RF pulse tipping the magnetization into the $-z$ axis. The magnetization starts relaxing back to its thermal equilibrium. After an inversion time, T_I , the 90° RF pulse is applied followed by the regular spin echo sequence. The magnetization that is at $z=0$ at time T_I does not experience the 90° RF pulse, and can

not have a contribution at the resulting spin echo. This technique is commonly used to suppress the signal coming from the CSF in brain tumor imaging to allow for a better differentiation of edema. T2 weighted FLAIR images show low intensity at the CSF locations, and hyperintensity in the areas of tumor, edema, and necrosis due to increased water content. Figure 2.7 shows a post-contrast T1 weighted and T2 weighted images of a brain tumor. The central part of the tumor is cystic with high fluid content.

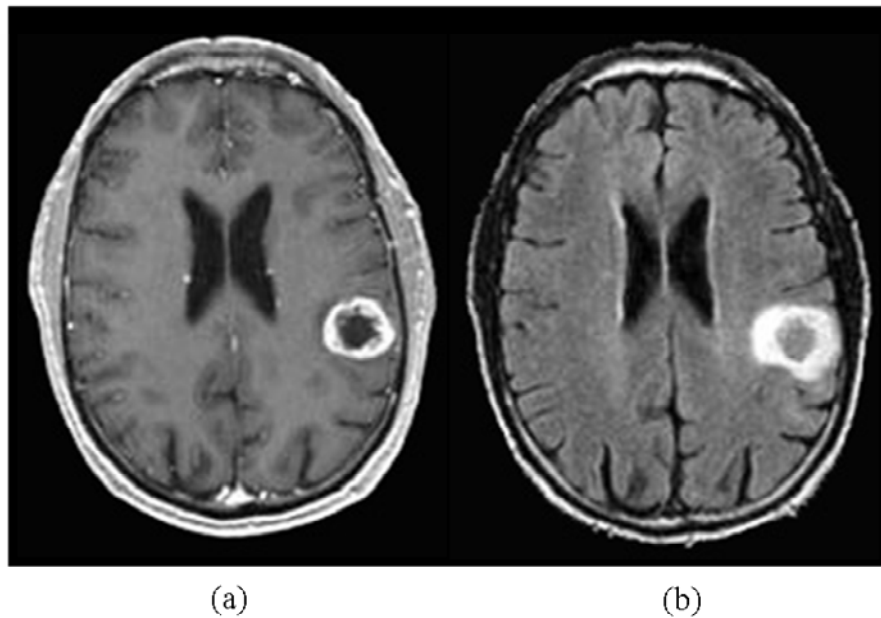


Figure 2.7. T1 post-contrast (a) and T2 weighted (b) images of a patient diagnosed with glioma.

Although magnetic resonance imaging (MRI) is highly sensitive in tumor detection(1), the true margin of tumor border may be difficult to assess especially in infiltrative tumors such as glioma. This is in part due to infiltrative growth pattern of gliomas into adjacent normal brain tissue, and therefore they often do not have grossly

or macroscopically definable margins. Physiological or functional MR imaging techniques like MR spectroscopic imaging, diffusion weighted imaging or perfusion weighted imaging are investigated to better the diagnostic capability of MRI and the treatment planning and the prognosis of patients.

Magnetic Resonance Spectroscopic Imaging

Three dimensional MR spectroscopic imaging (3D-MRSI) is a non-invasive technique that provides metabolic maps of the brain for quantitative assessment of brain metabolism (20). The combination of MRI and MRSI has been suggested to be more effective in tumor localization(20-23), staging (24,25), assessment of progression (20,25-29), and treatment planning (20,27,30-34) and response (20,35-38) than MR imaging alone. This section will describe the principles and data acquisition and reconstruction of spectroscopic imaging and its use for brain tumors.

MRSI Principles

MR spectroscopic imaging is based on the principle that not all protons in a molecule have resonance at the same frequency (39). There are two main basic principles behind the formation of an MR spectroscopic signal, called a 'spectrum'. The chemical shift is the reason multiple frequency components are observed within the signal from a single location. The spin coupling is the phenomenon that controls the multiplicity of the spectral peaks causing a split peak appearance. These two concepts will be briefly discussed.

Chemical Shift

The magnetic field experienced by a proton is influenced by multiple factors. Electron clouds around protons are known to create minimal magnetic fields opposing the main one, and reduce the protons' exposed magnetic field. This effect is known as the 'shielding' of electrons. The protons of the a molecule placed in a magnetic field might experience slightly different field strengths due to the variation in the electron environment, leading to different resonance frequencies, ω , defined as,

$$\omega = \gamma B_o (1 - \sigma), \quad (2.19)$$

where σ is the chemical shielding factor. The frequency differences expressed as relative differences are known as 'chemical shifts' (40). The frequency of a shielded proton is dependent on B_0 . It is possible to form an absolute frequency scale independent of the magnetic field strength called 'parts per million' (ppm). The ppm value for a proton resonating at a frequency ω_0 is defined as

$$ppm = \frac{\omega_0 - \omega_{ref}}{\omega_{ref}} \times 10^6, \quad (2.20)$$

where ω_{ref} is the reference frequency of tetramethylsilane (TMS) defined to be at 0 ppm and it is also same with the frequency of the spectrometer system. For example, the resonant frequency of fat protons differ from the protons of water by 225 Hz at 1.5 T and 450 Hz at 3T, but this difference is 3.5 ppm in both cases. The normal way of displaying MR spectra is to plot high ppm values on the left, and low ppm values on the right.

Spin Coupling

Another factor affecting the frequency of a proton in a molecule is the other protons in the vicinity of the proton of interest. The electronegative groups on the molecule neighboring the proton of interest also attract the electrons around the proton, resulting in less electron shielding and an increase in its frequency. This interaction between neighboring spins is called 'spin coupling' or 'J-coupling'. Not only neighboring protons affect the frequency of a given proton, they also cause multiple absorptions or multiple peaks from a single proton which is called 'spin-spin splitting'. The number of peaks for a proton is proportional to the number of protons connected by two or three bonds to the proton being observed. The spin-spin splitting can be explained by the $n+1$ rule in its most simplistic form. This rule states that protons that have n neighboring protons have $n+1$ peaks as a result of their interactions. For example, the propane which has a molecular structure of $\text{CH}_3\text{-CH}_2\text{-CH}_3$ would have three peaks (triplet) for the methyl (CH_3) groups because of the two protons on the methylene (CH_2) group. Similarly, the methylene group would have seven peaks (septet) because of the six neighboring protons of the methyl groups. The frequency difference between the multiple peaks of a proton would be same, and it depends on the coupling interaction between the spin groups. This constant frequency difference is called a 'J coupling constant'. In a linear carbon chain the $n+1$ rule is strictly obeyed if the neighboring proton coupling constants are all the same (39). The spectra that can be interpreted using the $n+1$ rule are called a 'first-order spectra'. However, in cases where the protons have strong coupling it results in a so called 'second order spectra' and its splitting patterns, intensities and number of peaks cannot be explained by the

simple $n+1$ rule. A more detailed spectral analysis is used for such spectra, and the reader can consult to reference (39) for more information on this topic.

MRSI Data Acquisition

Point Resolved Spectroscopy (PRESS)

Point resolved spectroscopy (PRESS) is a localization technique for acquiring spectral images of a specified location within the tissue of interest (41). PRESS utilizes three consecutive 90° , 180° and 180° slice selective RF pulses applied along with gradient pulses in three orthogonal directions. Figure 2.8 shows a schematic representation of the PRESS pulse sequence.

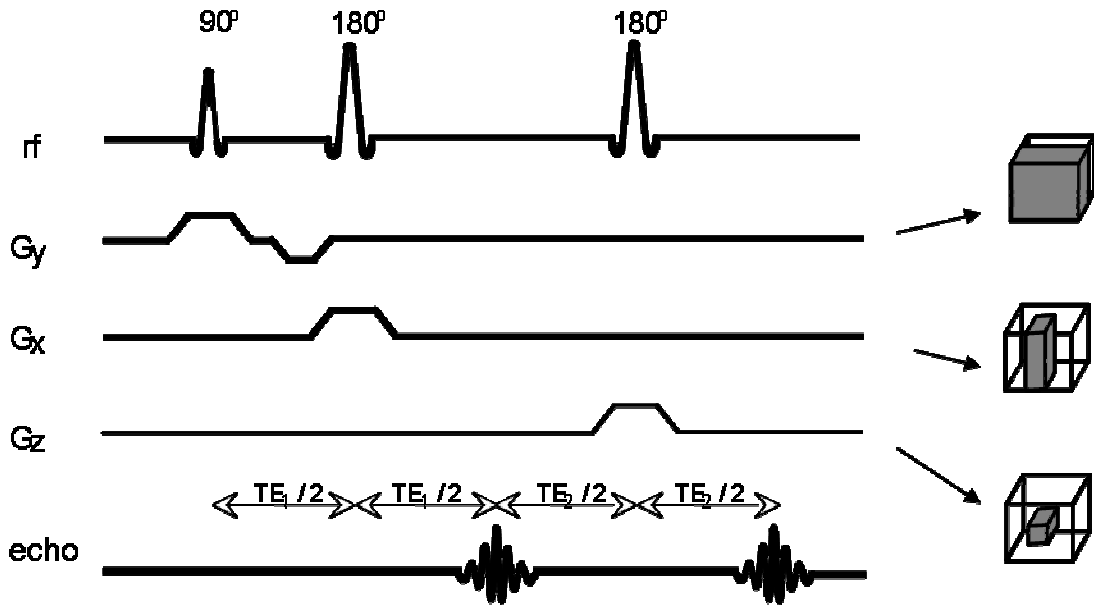


Figure 2.8. PRESS pulse sequence.

The first 90° RF pulse and its gradient along y excites the spins resonating at a certain frequency within a slice of tissue. The first 180° RF pulse and its gradient along x are applied at a time $TE_1/2$ after the 90° pulse, and it excites the spins located within a slice along x, and rephases the spins located only at a column located at the intersection of the previously excited slice y and the current slice x. An echo is formed at a time TE_1 after the 90° pulse due to the effects of the 90° and 180° pulses, and it is not sampled. The second 180° pulse is applied at a time $TE_2/2$ after the first 180° pulse with its gradient along z. This pulse excites the spins located within a slice along z, and rephases the spins located only at the intersection of all three selected slices. The final echo is formed at a time $TE_2/2$ after the second 180° RF pulse. This echo is sampled and processed to form a spectral image of the voxel at the intersection of all three excited slices.

Chemical Shift Selective (CHESS) Pulses

Chemical shift selective (CHESS) pulses (42) are 90° single frequency selective excitation pulses followed by big dephasing gradients. The procedure leaves the spin system in a state where no net magnetization of the component resonating at the selected frequency is retained. The other components resonating at different frequencies than the selected frequency remain entirely unaffected in the form of z-magnetization. Subsequent 90 degree excitation pulse of the pulse sequence only excites the frequencies which have z-magnetization. The resulting image or spectra contain minimal signal intensity for the suppressed frequency component. CHESS pulses are commonly used for water suppression in MR spectroscopy, and water or fat

suppression in MR imaging. Figure 2.9 shows a schematic representation of a CHESS pulse before the PRESS localization.

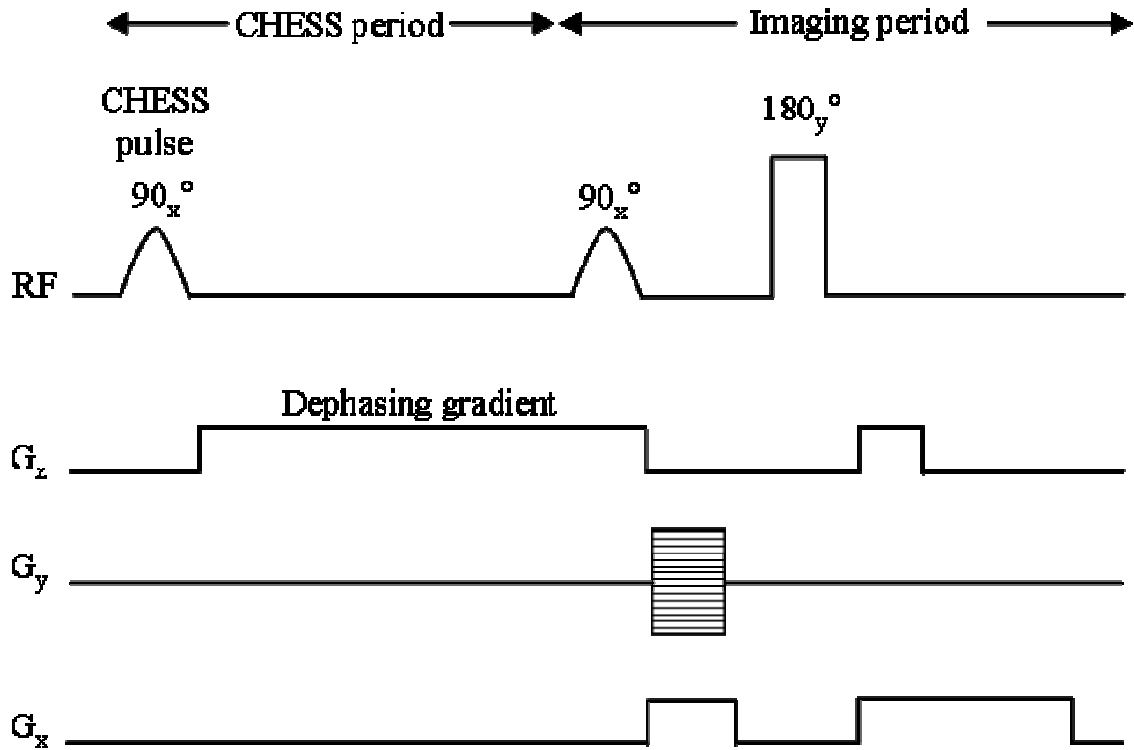


Figure 2.9. A CHESS pulse with the PRESS sequence.

Spectral Spatial Pulses and Very Selective Suppression (VSS) Pulses

Spectral spatial pulses (43) are a more recent group of RF pulses which can selectively excite both a restricted spatial region when applied in conjunction with a magnetic field gradient as well as a restricted frequency band. This band of frequencies can be adjusted to exclude frequencies that belong to the unwanted spectral components like lipid and/or water.

Very selective suppression (VSS) pulses (44) are short quadratic-phase spatial suppression pulses. Short trains of VSS pulses are used to provide improved spatial

suppression with reduced dependence on B1 and T1. VSS pulses have very sharp excitation profile. The passband of VSS pulses is very high on the order of 6 kHz, which results in reduced chemical shift artifact for MR spectroscopy. Figure 2.10 shows a schematic representation of VSS pulses applied along with spectral spatial pulses.

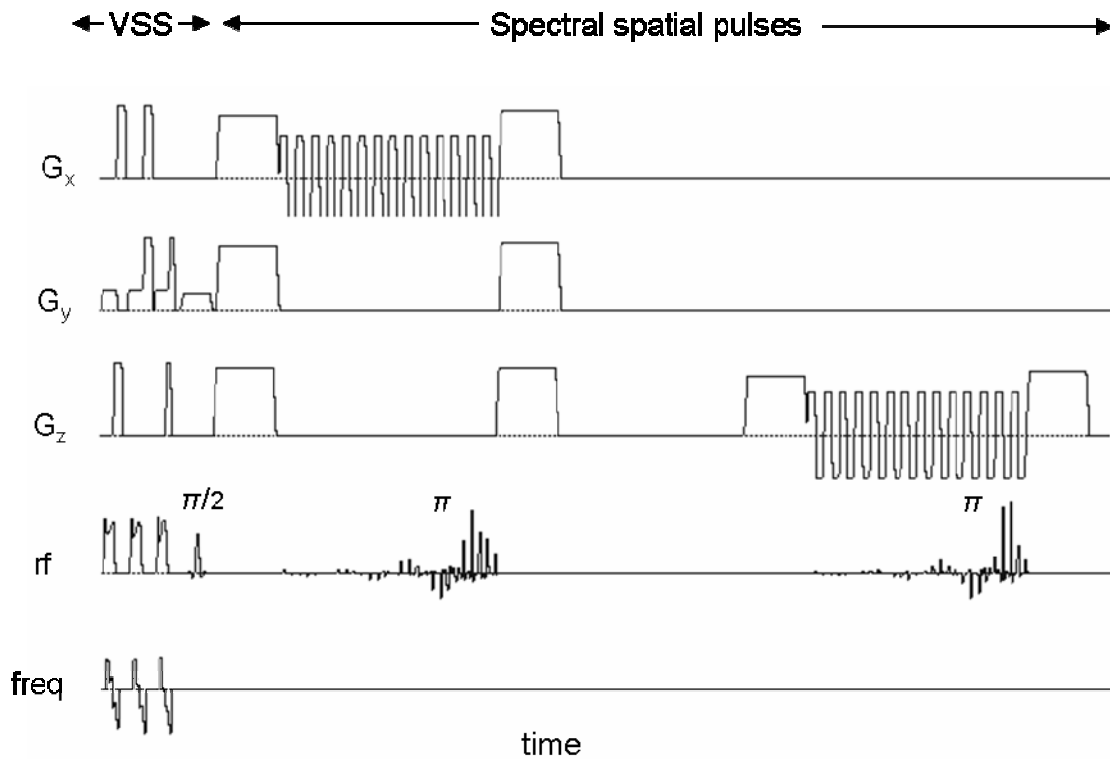


Figure 2.10. The VSS pulses with spectral spatial pulses.

Band Selective Inversion with Gradient Dephasing (BASING)

Band selective inversion with gradient dephasing (BASING) involves the application of a frequency-selective 180° pulse coupled with crusher gradients of opposite polarity that cause dephasing of flipped spins and remove any net magnetization from the target spin. It was originally developed to suppress water and

lipids for MR spectroscopy (45). Dual BASING pulses that has two such pulses are used for lactate editing (46). Lactate editing requires two separate data acquisitions. The lactate molecule has one methyl doublet at 1.3 ppm and a methine quartet at 4.1 ppm. The dual BASING pulses can control the phase of the methyl doublet of lactate independently of TE by adjusting the time in between the dual BASING pulses when the methine quartet is placed within the BASING inversion band. In the first acquisition, BASING inversion band is placed to include the methine quartet and the time between the dual pulses is adjusted to TE/2 resulting in an upright lactate methyl doublet. In the second acquisition, methine quartet is excluded from the inversion band and the TE is adjusted to be an odd multiple of $1/J$, resulting in an inverted lactate methyl doublet. The sum of these two spectra results in zero lactate, and their difference results in twice the amount of lactate. Figure 2.11 shows the dual BASING scheme incorporated into the PRESS sequence.

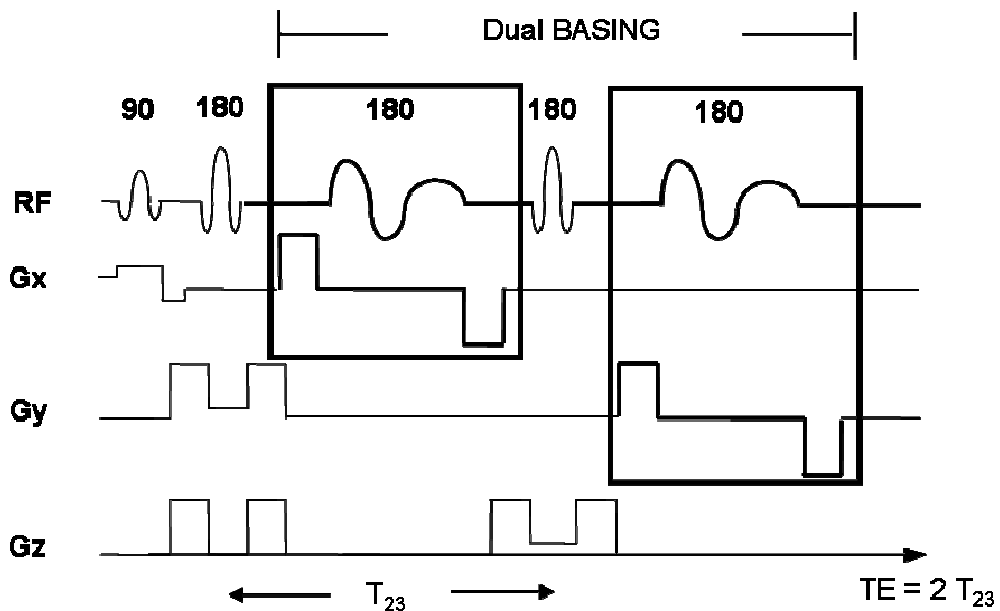


Figure 2.11. Dual BASING scheme incorporated into the PRESS sequence.

MRSI Data Reconstruction

After the MRSI signal is acquired, it is processed by a multi-step automated procedure (47) composed of routines for reconstruction and correction of the spectral data for frequency, phase and baseline distortions, and final estimation of the parameters for the peaks of interest. The analysis is initiated by apodizing the FIDs in the time domain with a Lorentzian or a Gaussian filter, followed by fast Fourier transformation (FFT) from the time to the frequency domain. Data acquisition parameters are extracted from the header of the reference MR images for accurate registration of the spectra to the anatomical images and for correct interpretation. Discrete Fourier transformation (DFT) is applied to the data to generate a 3D array of spectra on a rectangular grid based on the coordinate system of the reference anatomical images. The center of the grid is spatially shifted to reduce the partial voluming effects around the edges of the excited region and to maximize the full tissue voxels.

Frequency shifts are corrected for each spectrum based on a peak descriptor file, which includes the expected locations and linewidths of spectral peaks. A statistical peak finding routine is applied to the magnitude data (47) to locate the frequencies of each peak of the spectrum. The frequency shift for each peak is estimated as the difference between the peak location found by the algorithm and the location given in the peak descriptor file. The mean of the frequency shifts of all the peaks is applied to the spectrum as the estimated frequency correction.

An automatic phase correction algorithm is used to find the value that maximizes the area of the real part, while minimizing the area of the imaginary part of

the spectrum. Baseline removal routine assumes that the spectra are a sum of the peaks, baseline, residual water, and random noise, and iteratively separates these components. The algorithm isolates the data points that corresponded to the spectral peak regions by using the locations and linewidths given in the peak descriptor file at the first iteration. Variations of the peak parameters for the given data are inspected, and used for further iterations.

After the baseline correction, peak locations and heights are determined by searching for a maximum in each of the peak regions. Peak heights are estimated and areas are calculated by integrating over the peak regions given in the peak descriptor file in the real part of the spectrum.

MRSI Peaks for Brain Tumors

Long echo time 3D-MRSI for *in vivo* brain applications provides arrays of spectra that are characterized by three major metabolite peaks in healthy brain tissue; namely the singlets of choline (Cho), total creatine (Cr) and N-acetyl aspartate (NAA). In tumor tissue lactate and lipid peaks might also be observed. Table 2.4 displays the chemical structures of the brain metabolites and their ppm locations.

Choline is an essential nutrient that is mainly obtained in the form of phospholipids in the diet. It is required for the synthesis of the neurotransmitter acetylcholine and phosphatidylcholine, a major constituent of the cell membrane. An increase in the levels of choline provides a marker for excessive cell growth or cell membrane turnover. The peak of creatine and phosphocreatine reflects bioenergetics processes due to their role as a phosphate recipient or donor for ATP or ADP, and is thought to represent the energetic status of the cell. NAA is the most abundant amino

acid in brain that is synthesized in neurons, and is hypothesized to have a role in the removal of intracellular water from neurons. NAA is an indicator of the neuronal viability that is usually observed to be significantly lower in tumors than regions of normal brain. Figure 2.12 shows a typical normal and tumor spectra of the brain tissue at the top and bottom rows, respectively.

Table 2.4 Brain metabolites' chemical structures and chemical shifts

	Chemical Structure	Chemical Shift (ppm)
Choline	$OH-CH_2-CH_2-N-(CH_3)_3$	3.2
Creatine	$ \begin{array}{c} \sigma \\ \\ O=C-CH_2-N-C-NH_3 \\ \quad \\ CH_3 \quad NH \end{array} $	3.0
N-acetyl aspartate	$ \begin{array}{c} \sigma \qquad \qquad \qquad \sigma \\ \qquad \qquad \qquad \\ O=C-CH-CH_2-C=O \\ \\ NH \\ \\ C=O \\ \\ CH_3 \end{array} $	2.0
Lactate	$ \begin{array}{c} \sigma \\ \\ O=C-CH-CH_3 \\ \\ OH \end{array} $	1.3
Lipid	$ \begin{array}{c} O \\ \\ CH_2-O-C-(CH_2)_n-CH_3 \\ \\ O \\ \\ CH_2-O-C-(CH_2)_n-CH_3 \\ \\ O \\ \\ CH_2-O-C-(CH_2)_n-CH_3 \end{array} $	1.3

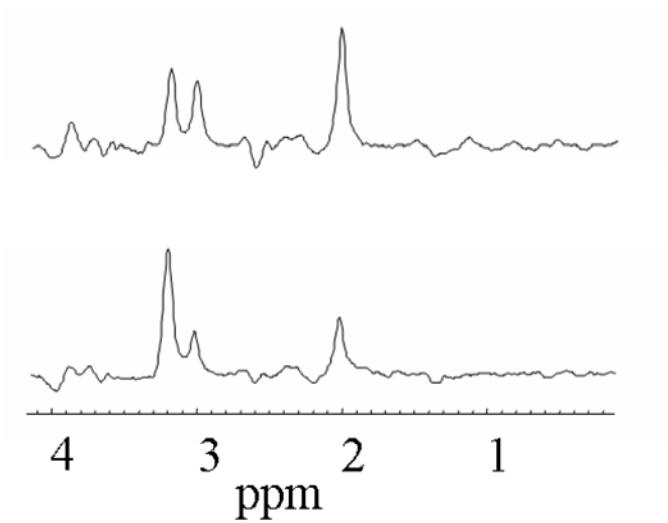


Figure 2.12. Typical normal and tumor spectra for brain tissue.

Figure 2.13 displays the T1 weighted MR image and an array of spectral voxels displaying tumor spectra with high Cho and low NAA levels for a glioma patient.

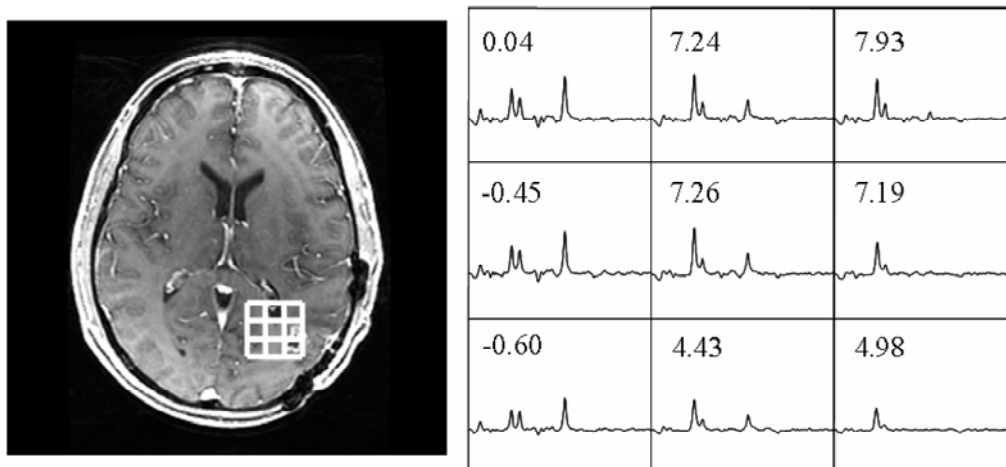


Figure 2.13. T1 weighted MR image along with the spectra located at the white grid for a glioma patient.

Singlet lipid and doublet lactate peaks can be observed in the disease state. Lactate is a byproduct of anaerobic glycolysis, and is expected to be present in tumor areas as a result and indicator of poor oxygenation. Lipid is present in the lipid bilayer of the cell membrane in brain cells, and presence of lipid in the spectra might indicate cell membrane breakdown and a more aggressive tumor phenotype. Figure 2.14 shows another glioma patient's T1 weighted MR image and the spectra from four voxels within the contrast enhancement that displays high lactate or lipid levels.

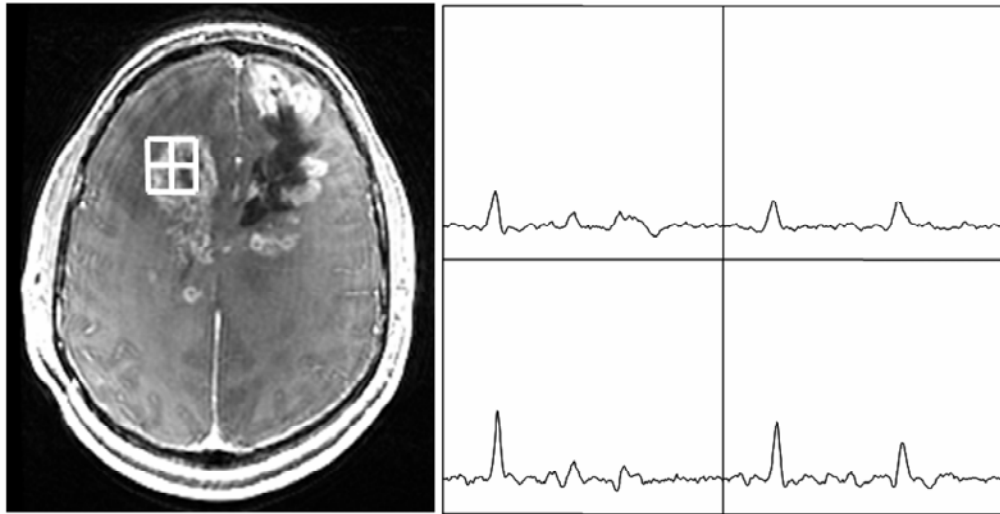


Figure 2.14. Lipid and lactate presence within a brain tumor. T1 weighted MR image is shown on the left and the spectra from the white grid is shown on the right.

3 . Spatial Characteristics and Correlations of Newly Diagnosed Grade 3 Gliomas Using MRI, 3D MR Spectroscopic Imaging, and Diffusion Tensor Imaging

This chapter studies the spatial characteristics of grade 3 gliomas using MR spectroscopic and diffusing imaging. The correlations of spectroscopic and diffusion parameters are also calculated and discussed.

Rationale

Following surgical resection high grade glioma patients undergo concurrent radiation/chemotherapy and continue chemotherapy afterwards. Despite recent developments in surgical techniques and postoperative treatment, the prognosis for patients with a high-grade glioma remains very poor with a median survival of 33.5 months and progression free survival of 15.8 months for patients with grade 3 astrocytomas (48). It is desirable to understand the characteristics of high grade gliomas using MR imaging techniques to more effectively plan the treatment to increase patient quality of life and survival.

In the current study, we have combined 3D MR spectroscopic and diffusion tensor imaging parameters to study the regional characteristics and correlations of treatment naïve grade 3 gliomas to understand the spatial tumor extent especially in the cases where the tumor is predominantly nonenhancing. To our knowledge there has been no study that looked into spectroscopic and diffusion correlations and characteristics in

different regions of newly diagnosed grade 3 gliomas in detail. For a previous study of patients with newly diagnosed grade 3 gliomas, the lesions were reported to have higher ADC, and lower ANI values than normal appearing white matter (NAWM) due to the presence of infiltrative tumor (24). The same study noted similar creatine levels within grade 3 tumor areas compared to NAWM areas indicating well oxygenation, but there were also a small number of voxels observed to have lactate and lipid peaks which may indicate regional hypoxia and microscopic necrosis. In another study conducted by Catalaa et al., newly diagnosed grade 3 lesions were observed to have significantly higher Cho, higher ADC, and lower ANI values in both the contrast enhancing and nonenhancing tumor regions compared to NAWM (49). Another study conducted by Li et al. reported the presence of significant lactate and lipid peaks within grade 3 glial tumor areas with volumes varying from 0.1 cc to 11.8 cc (24). A positive correlation was also observed between volumes of lactate and lipid abnormality and CE.

Our previous studies that were conducted on a different population of grade 3 glioma patients showed that 95% of the patients exhibited metabolically abnormal extensions beyond the T2 hyperintense areas and indicated that the T2 hyperintensity did not discriminate all tumor areas (33). Contrast enhancing volumes were also observed to be vastly smaller than the volumes of metabolically abnormal regions. Another finding was that the metabolically active and anatomically defined tumor areas did not coincide. In the current paper, we have also studied the overlap of anatomical tumor regions and metabolically abnormal regions, and the characteristics of spectral and diffusion parameters within both of these regions to see whether

additional information is obtained by spectroscopic imaging. Correlations of the diffusion and spectral parameters within these sub-tumor regions were also calculated, and their impact upon the understanding of regional tumor characteristics were discussed.

Materials and Methods

Diffusion Tensor Imaging

Diffusion tensor imaging (DTI) is another MR sequence that has been proposed as adding tissue structural information to the anatomical MR imaging. Figure 3.1 displays a simplified diffusion weighted spin echo sequence diagram.

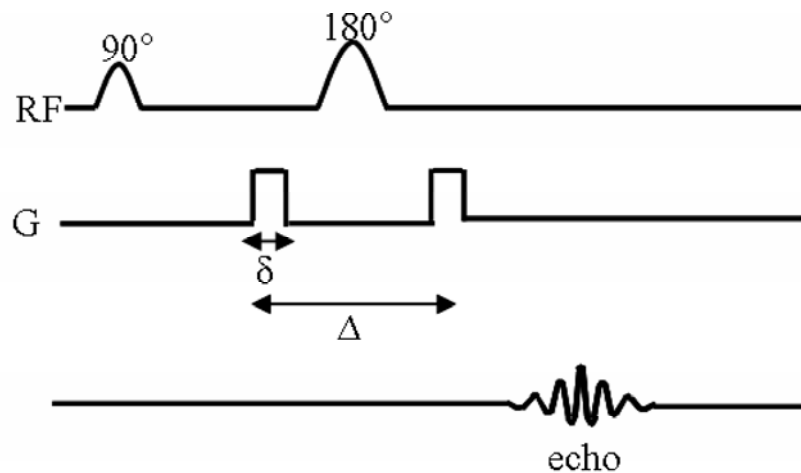


Figure 3.1. Diffusion weighted spin echo sequence diagram.

Two diffusion gradients identical in amplitude and width, δ , are separated by time Δ , and applied symmetrically about the 180° pulse. The stationary spins will gain two opposing phases due to the symmetrical diffusion gradients that will cancel each other

out. On the other hand, spins that are diffusing throughout time Δ will gain different phases because of varying gradient fields in the original and target locations that will sum up to a net phase. As a result, the diffusing spins will dephase faster causing a signal reduction. A reference scan is also acquired without any diffusion gradients. The relation between the reference signal and signal in the presence of diffusion gradients is estimated by the formula

$$\frac{S}{S_0} = e^{-(G\gamma\delta)^2 D(\Delta-\delta/3)}, \quad (3.1)$$

where D is the diffusion coefficient.

A diffusion tensor matrix is formed from the diffusion coefficients along multiple directions. This matrix is solved for its eigenvalues and eigenvectors, which then are used in the computation of the apparent diffusion coefficient (ADC) and fractional anisotropy (ANI) as (50)

$$ADC = \lambda_1 + \lambda_2 + \lambda_3 / 3, \text{ and} \quad (3.2)$$

$$ANI = \sqrt{1/6} \sqrt{\frac{\sum_{n=1}^3 (ADC - \lambda_n)^2}{\sum_{n=1}^3 \lambda_n^2}}, \quad (3.3)$$

where λ are the eigenvalues of the diffusion tensor matrix.

DTI has been used to examine disruptions in the integrity of white matter tracts and changes in water content or cellularity. ADC values are an indicator of the range of free water diffusion, and have been shown to increase in brain tumors within the solid tumor region and surrounding edema regions (24,49,51-53). Several studies have been conducted to survey the ability of ADC values to differentiate tumor infiltrated edema of gliomas and vasogenic edema of metastases and meningiomas, but no

significant differences have been noted (53-56). ANI values are markers of the directionality of water diffusion and have been shown to decrease in brain tumors due to the disruptions of the brain tissue architecture, both in solid tumor and regions of edema (24,49,53,55,57).

Inverse correlations have been reported between the ADC and tumor proliferation through the analysis of Ki-67 labeling index (58), cell density(59), tumor cellularity (60), and malignancy (52) for mixed populations of brain tumors. In another study that was conducted on a mixed population of grade 2 and 3 glioma patients, a positive correlation between ADC values and total tumor cell number, and a negative correlation between ANI and total tumor cell number have been reported (61). Correlations between spectroscopic and diffusion parameters have also been investigated in the literature. Inverse correlations between Cho and ADC were shown for a mixed grade patient population (62) and a patient population with grade IV gliomas (49). Another recent study presented a positive correlation between ANI and NAA, with both parameters decreasing from the surrounding edema to the center of the tumor (57).

Patient Population

Thirty-two patients (17 male, 15 female, 21 astrocytomas, 6 oligodendrogliomas, 5 oligoastrocytomas, age (median±std) = 36±12) who were newly diagnosed with a Grade 3 glioma according to WHO II classification were scanned on a 1.5 T GE Signa EchoSpeed scanner (GE Medical Systems, Milwaukee, WI) prior to biopsy and

surgery. All the patients provided informed consent for participating in the study, based on a protocol approved by the Committee on Human Research at our institution.

Data Acquisition

The MRI protocol included an axial T2-weighted FSE sequence (TR = 3000 ms, TE = 105 ms, matrix size = 192x256x120, field of view = 195x260x180 mm, slice thickness = 1.5 mm), and post-Gd-DTPA T1-weighted SPGR sequence (TR = 34 ms, TE = 3 ms, 35° flip angle, matrix size = 192x256x124, field of view = 195x260x186 mm, slice thickness = 1.5 mm). 3D MRSI data were referenced on the SPGR images using Point Resolved Spectroscopic (PRESS) (41) volume localization with spectral spatial pulses (43) and very selective suppression (VSS) (44) outer volume suppression bands (TR = 1000 ms, TE = 144 ms, matrix size = 12x12x8, field of view = 120x120x80 mm, 1 cc nominal spatial resolution). Spectral data from 9 patients were acquired with J-difference lactate editing that allowed separate lactate and lipid quantification (46). DTI sequences with six gradient directions were acquired in the axial planes with a b value of 1000 s/mm² (TR = 5000ms, TE = 105 ms, matrix size = 256x256x40, field of view = 440x440x84 mm, slice thickness = 2.1 mm).

Data Reconstruction

3D MRSI data were quantified offline to estimate the levels of Cho, Cr, NAA, combined lactate and lipid (LL) for regular spectra, and separate lactate (Lac) and lipid levels for lactate-edited spectra using in-house software described in detail in a previous report (47). Spectral values were normalized relative to the noise levels of the right hand end of the spectra. Choline to NAA index (CNI) (29), which defines the

distance between the levels of Cho and NAA for a given voxel and a regression line fit to the Cho and NAA values in the normal voxels in a given subject, were calculated for each voxel of all the patients. CNI values increase as a result of a reduction in NAA and/or an increase in Cho. DTI images were quantified to calculate the ADC and ANI maps using in house software. Diffusion maps were resampled to the resolution of spectral data and normalized relative to the mean of the voxels in normal appearing white matter (NAWM) to form maps of nADC and nANI.

Regions

Regions of contrast enhancement (CEL) and T2 hyperintensity (T2) were defined manually by tracing the borders of the abnormality on SPGR and FSE images using an interactive in-house software package. The non-enhancing lesion (NEL) was defined as the regions of T2 hyperintensity which excluded the contrast enhancement. Metabolically abnormal regions were defined as the voxels that had CNI values greater or equal to 2 based on previous results (24). CNI maps were then used to automatically generate three regions with distinct levels of metabolic abnormality, which were $2 \leq \text{CNI} < 3$ (CNI2), $3 \leq \text{CNI} < 4$ (CNI3), and $\text{CNI} \geq 4$ (CNI4) respectively. Figure 3.2 shows an example of the regions analyzed for this study.

Statistical Analysis

A total of 7852 voxels of data were considered from the PRESS localized volumes, including 1573 from the NEL, 561 from the CNI2, 305 from the CNI3, 509

from the CNI4, 46 from the CEL, and 48 from NAWM. A single median value was calculated for each spectral or diffusion parameter within a given region of interest.

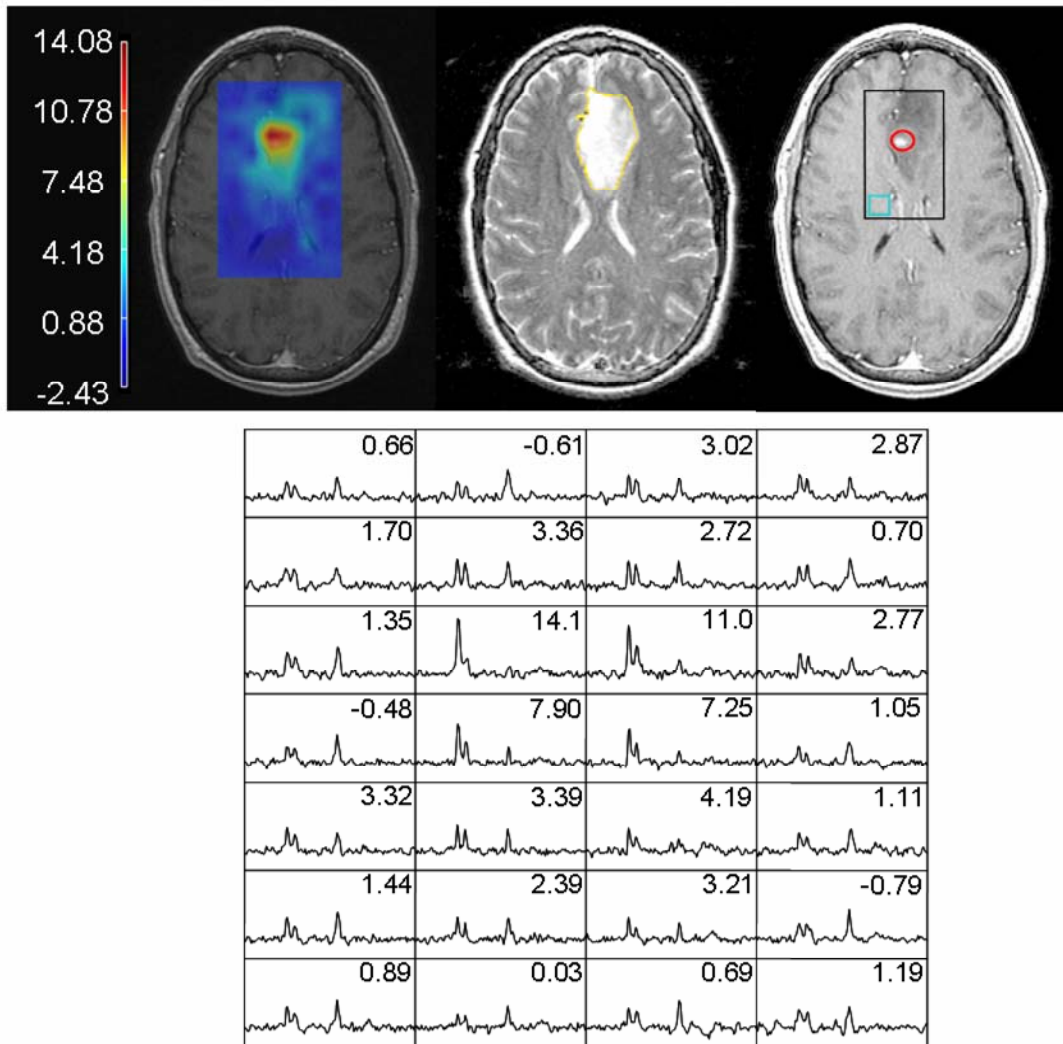


Figure 3.2. Forty year old male patient diagnosed with a left frontal grade 3 astrocytoma. Images from left to right display the distribution of CNI values, the FSE image with the NEL region (yellow), and T1 weighted post-Gd SPGR image with the CEL(red), NAWM(blue), and an axial representation of the MRSI excited region (black box). Spectra from the black box are shown at the bottom with the corresponding CNI values displayed in each voxel.

A Wilcoxon sign rank test was applied to detect paired significant differences of medians of spectral or diffusion values between the tumoral regions and NAWM for all of the patients. Anatomical and metabolic lesion parameters were not compared

with each other, because these regions were not necessarily mutually exclusive. The median values reported in tables 3.1-3.3 were calculated from the medians of all the patients who exhibited a given region. Wilcoxon sign rank tests were conducted only on those patients who had both of the regions being compared. It is necessary to note that the median values of the data used in each sign rank test were similar to the median values reported in the tables. Spearman rank correlation coefficients were calculated to detect correlations of diffusion and spectral parameters within the regions of interest. Correlation of spectral or diffusion parameters within their respective groups were not calculated due to possible statistical dependency. P values of less than 0.05 were considered significant, and values between 0.05 and 0.10 were considered trends. No formal adjustments were made for multiple comparisons.

Results

Tumor Spatial Extent and Coverage

All the grade 3 patients included in this study exhibited a T2 hyperintense lesion. Median NEL coverage within the PRESS box was $56.3 \pm 13.9\%$ (median \pm std) (min = 30%, max = 93.9%). Eighteen out of thirty-two patients exhibited contrast enhancement on the SPGR images obtained after the injection of Gd-DTPA. Five of these patients showed minimal CE, and their contrast enhancing regions were not taken into account in this analysis. In twelve out of the remaining thirteen patients, the spectroscopic PRESS region covered the majority of the contrast enhancement. The median coverage of the CEL by the PRESS box for these twelve patients was 100%

(min = 16.6%, max = 100%). According to the spectral parameters, thirty-one patients had CNI2 regions, twenty-eight patients had CNI3 regions, and twenty-nine patients had CNI4 regions.

Overlap of Anatomical Tumor Regions and Metabolically Abnormal Areas

The CEL that was covered within the PRESS box was found to reside within the CNI4 region for five patients, within the CNI3 region for three patients, and within the CNI2 region for two patients. There were only two patients who each had two CE voxels outside the CNI defined regions. For one patient 50% and for the other 75% of their CE stayed within the CNI3. The CNI defined regions resided within the T2 hyperintensity in all of the patients. The median percentage of the NEL that did not overlap with the CNI defined regions was $35.9 \pm 24\%$ (median \pm std) (min = 3.7%, max = 100%).

Spectral and Diffusion Parameters within Anatomical Tumor Regions

Figures 3.3-3.5 depict the box plots of the distribution of the median values of all the metabolite and diffusion values in the anatomical tumor regions, metabolically abnormal areas and NAWM. Several differences in the median metabolite levels, CNI, and diffusion values were found between the anatomical tumor regions and NAWM as summarized in Table 3.1.

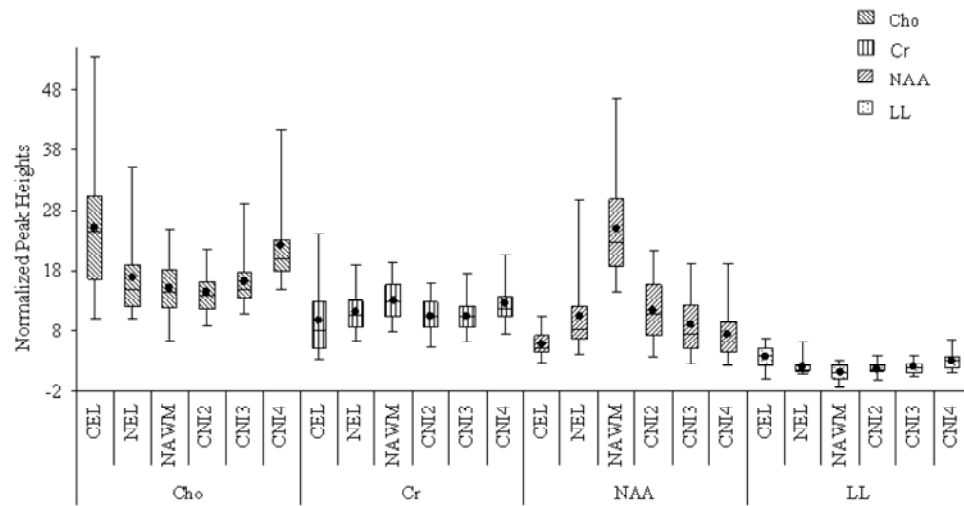


Figure 3.3. Box plots of median spectral peak heights for all the patients. The borders of the box plots are 25th and 75th percentile of the median values. The line inside the box depicts the median and the black dot depicts the mean of the median values. Error bars extending outside of the boxes indicate the minimum and maximum median values for this patient population.

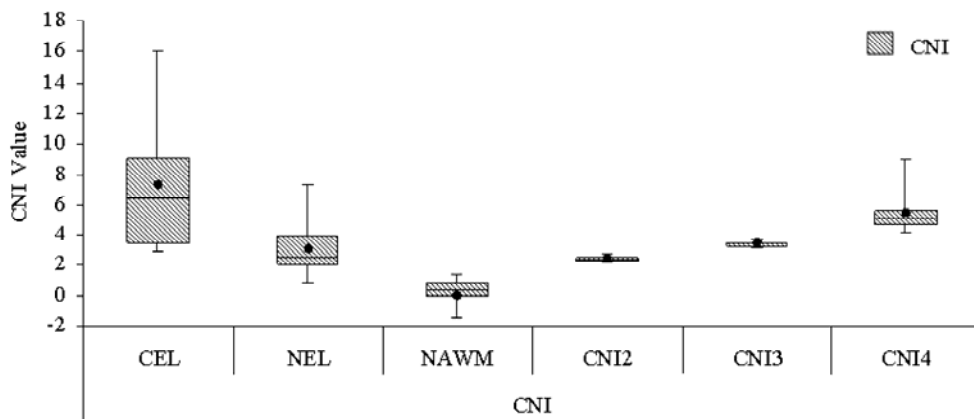


Figure 3.4. Box plots of median CNI values for all the patients.

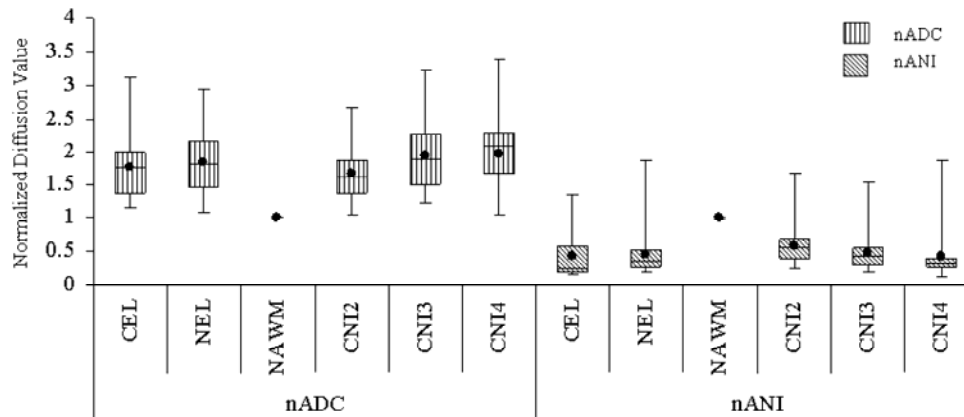


Figure 3.5. Box plots of median normalized ADC and ANI values for all the patients.

Table 3.1. Differences of spectral and diffusion parameters between NAWM, CEL, and NEL

Parameter	Region	Median±SD	N	CEL	NEL
Cho	NAWM	14.38 ± 4.68	32	p=0.003*	ns
	CEL	24.56 ± 12.26	12		p=0.03*
	NEL	14.94 ± 6.4	32		
Cr	NAWM	12.85 ± 3.16	32	ns	p=0.007*
	CEL	8.12 ± 6.15	12		ns
	NEL	10.64 ± 3.67	32		
NAA	NAWM	22.68 ± 8.72	32	p<0.001*	p<0.001*
	CEL	5.09 ± 2.14	12		p=0.001*
	NEL	8.28 ± 6.2	32		
CNI	NAWM	0.02 ± 0.62	32	p<0.001*	p<0.001*
	CEL	6.39 ± 4.56	12		p=0.001*
	NEL	2.51 ± 1.66	32		
LL	NAWM	0.95 ± 1.08	32	p=0.005*	p=0.001*
	CEL	3.79 ± 1.96	12		p=0.003*
	NEL	1.61 ± 1.03	32		
nADC	NAWM	1 ± 0	32	p<0.001*	p<0.001*
	CEL	1.76 ± 0.54	12		ns
	NEL	1.81 ± 0.46	32		
nANI	NAWM	1 ± 0.01	32	p=0.001*	p<0.001*
	CEL	0.26 ± 0.37	12		p=0.02*
	NEL	0.36 ± 0.31	32		

*: significant (p<0.05), tr: trend (0.05<p<0.10), ns: not significant

Although Cho levels were not significantly different in the NEL compared to NAWM, there was a significant increase in Cho in the CEL region compared to both the NEL and NAWM. Cr values were observed to be highly variable in different patients, but the median Cr levels were 31.9 % (min=-67.7%, max=76.1%) lower in CEL and 13.1% (min = -62.4%, max = 65%) lower in NEL compared to NAWM. The decrease was significant in the NEL when compared to NAWM. NAA levels were significantly lower in all of the anatomic lesion regions compared to NAWM. NAA levels were also significantly lower in the CEL than in the NEL. The highest Cho, lowest NAA, and accordingly highest CNI levels were observed in the CEL. Combined lipid and lactate levels were significantly higher in NEL and CEL than in NAWM, and were also significantly higher in CEL than in NEL. The highest median LL levels were observed in the CEL.

Lactate edited spectroscopic data was acquired in 9 patients. Figure 3.6 displays a Grade 3 patient whose spectral data was acquired with lactate editing. The summed spectra that display Cho, Cr and NAA are shown on the left, and the difference spectra that display lactate peaks are shown on the right. The spectral voxels that had high Cho and low NAA intensities with CNI>2 are marked with gray shading. These voxels also displayed prominent lactate doublets at 1.3 ppm. Figure 3.7 shows the box plots for median lactate values estimated from the nine patient datasets acquired with lactate editing. Table 3.2 displays the results of the corresponding sign rank test that detected significant difference in median lactate levels between the different regions.

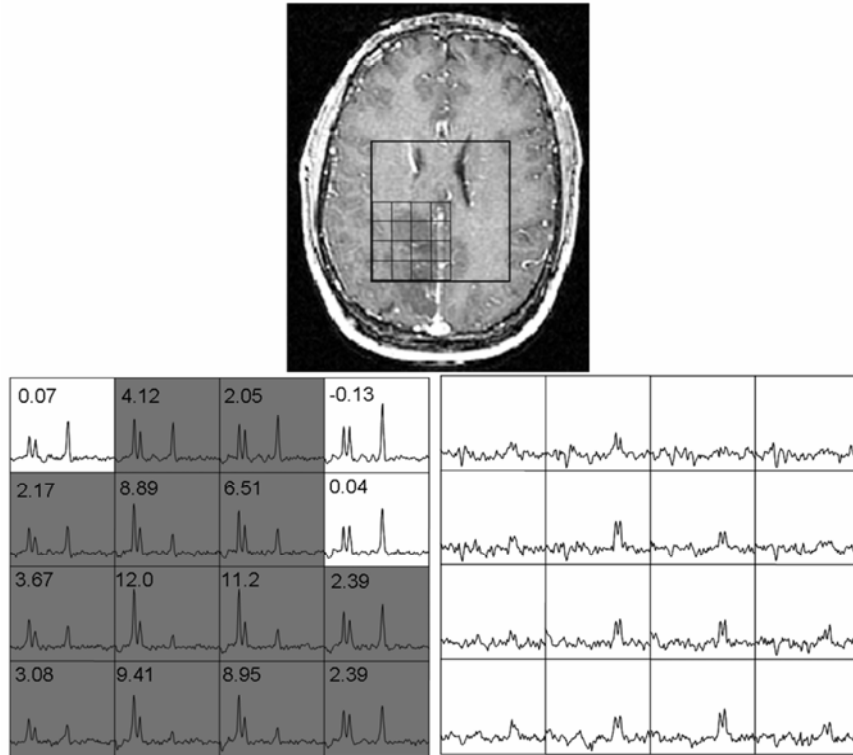


Figure 3.6. Presence of lactate within the hypointense region in a 24 years old male patient diagnosed with a grade 3 oligoastrocytoma. The spectral data was acquired with J-difference lactate editing method. Top: Post Gd-DTPA T1 weighted SPGR image with the spectral grid superimposed upon it. Bottom: Corresponding summed spectra is shown on the left with gray shaded voxels that have $CNI \geq 2$. The difference lactate spectra are shown on the right.

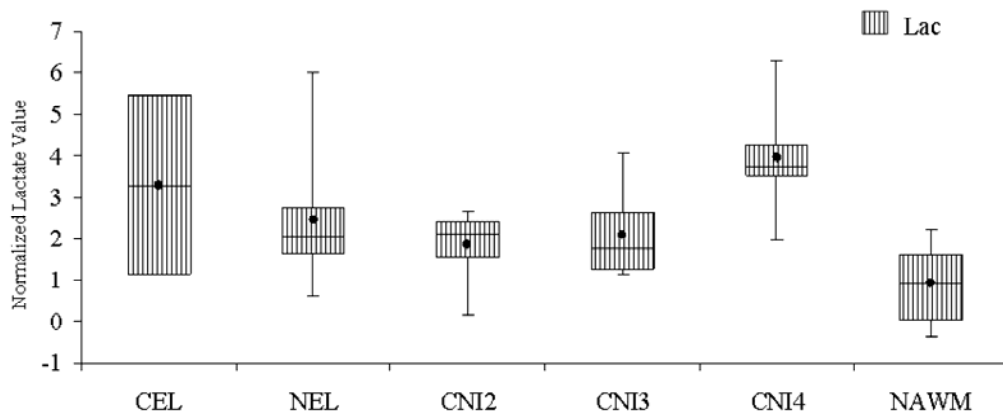


Figure 3.7. Box plots of median lactate levels estimated from the J-editing PRESS spectroscopy for all the patients in all of the regions of interest.

Table 3.2 Differences of lactate between NAWM, CEL and NEL, and between NAWM and CNI abnormal regions

Parameter	Region	Median±SD	N	CEL	NEL
Lactate	NAWM	0.90±0.95	9	-	p=0.004*
	CEL	3.29±3.06	2	-	-
	NEL	2.06±1.53	9	-	-

Parameter	Region	Median±SD	N	CNI2	CNI3	CNI4
Lactate	NAWM	0.90±0.95	9	p=0.01*	p=0.06 ^{tr}	p=0.03*
	CNI2	2.14±0.82	8		ns	p=0.03*
	CNI3	1.77±1.18	5			p=0.06 ^{tr}
	CNI4	3.77±1.39	6			

*: significant ($p < 0.05$), tr: trend ($0.05 < p < 0.10$), ns: not significant

Lactate was significantly higher in the NEL compared to NAWM. Only two patients in the lactate edited population displayed contrast enhancement. A statistical test could not be conducted to compare the lactate levels in the CEL with other regions due to the lack of enough data points for the CEL, but the median lactate level in CEL was higher than both the NEL and NAWM. The CNI2 and CNI4 regions had significantly higher lactate values than NAWM.

Normalized ADC values were significantly higher in all of the anatomical lesion regions compared to NAWM. nADC values were similar between NEL and CEL. nANI levels were significantly lower in all of the anatomic lesion regions than in NAWM. The CEL region had significantly lower nANI values than the NEL, and was the region with the lowest median nANI values.

Spectral and Diffusion Parameters within Metabolically Abnormal Areas

Table 3.3 displays the differences of spectral and diffusion parameters between the metabolically abnormal areas and NAWM.

Table 3.3. Differences of spectral and diffusion parameters in NAWM and CNI ≥ 2 regions

Parameter	Region	Median \pm SD	N	CNI2	CNI3	CNI4
Cho	NAWM	14.37 \pm 4.68	32	ns	p=0.10 ^{tr}	p<0.001*
	CNI2	13.99 \pm 3.45	31		p<0.001*	p<0.001*
	CNI3	14.79 \pm 3.67	28		p<0.001*	
	CNI4	19.72 \pm 6.56	29		p<0.001*	
Cr	NAWM	12.85 \pm 3.16	32	p<0.001*	p=0.002*	ns
	CNI2	10.33 \pm 2.80	31		ns	p<0.001*
	CNI3	10.53 \pm 2.73	28		p=0.001*	
	CNI4	11.7 \pm 3.59	29			
NAA	NAWM	22.68 \pm 8.72	32	p<0.001*	p<0.001*	p<0.001*
	CNI2	10.85 \pm 5.07	31		p=0.01*	p<0.001*
	CNI3	7.37 \pm 4.78	28		p<0.001*	
	CNI4	6.1 \pm 3.90	29			
CNI	NAWM	0.02 \pm 0.62	32	p<0.001*	p<0.001*	p<0.001*
	CNI2	2.40 \pm 0.13	31		p<0.001*	p<0.001*
	CNI3	3.43 \pm 0.17	28		p<0.001*	
	CNI4	5.10 \pm 1.12	29			
LL	NAWM	0.95 \pm 1.08	32	p=0.05 ^{tr}	p=0.02*	p<0.001*
	CNI2	1.59 \pm 0.80	31		p=0.06 ^{tr}	p<0.001*
	CNI3	1.84 \pm 0.93	28		p=0.004*	
	CNI4	2.85 \pm 1.26	29			
nADC	NAWM	1 \pm 0	32	p<0.001*	p<0.001*	p<0.001*
	CNI2	1.62 \pm 0.44	31		p<0.001*	p=0.001*
	CNI3	1.88 \pm 0.49	28		ns	
	CNI4	2.07 \pm 0.51	29			
nANI	NAWM	1 \pm 0.01	32	p<0.001*	p<0.001*	p<0.001*
	CNI2	0.56 \pm 0.31	31		p<0.001*	p=0.002*
	CNI3	0.41 \pm 0.26	28		p=0.03*	
	CNI4	0.32 \pm 0.34	29			

*: significant (p<0.05), tr: trend (0.05<p<0.10), ns: not significant

Several differences for the parameters were noted between these regions. Cho levels were not significantly different between the CNI2 and NAWM, but there was a trend of increase in Cho in the CNI3. The CNI4 had significantly higher Cho levels compared to NAWM, and there was a significant increase in Cho with increasing CNI levels. The CNI2 and CNI3 regions had significantly lower Cr levels than both NAWM and the CNI4.

NAA levels were significantly lower in all of the metabolically abnormal regions compared to NAWM. NAA values were significantly decreased between increasing CNI levels. All metabolic regions had higher LL than NAWM. LL levels showed an increasing trend in the CNI2 when compared to NAWM, and between the CNI2 and CNI3 regions. LL levels were significantly higher in both the CNI3 and CNI4 than NAWM. LL was also significantly different between the CNI2 and CNI4, and the CNI3 and CNI4. For the nine patients whose spectral data were acquired with lactate editing, there was a trend of higher lactate values in the CNI3 region compared to NAWM. The CNI4 region had significantly higher lactate levels than the CNI2, whereas the CNI2 and CNI3 regions had similar lactate levels. There was a trend towards increasing lactate values in the CNI4 compared to the CNI3 region.

Normalized ADC values were significantly higher in all of the metabolically abnormal regions compared to NAWM. nADC values were similar between CNI3 and CNI4, but CNI3 and CNI4 regions both had significantly higher nADC levels than CNI2. The CNI4 was the region that had the highest median nADC values. nANI levels were significantly lower in all of the metabolically abnormal regions than in

NAWM. The nANI values significantly decreased between all of the increasing CNI levels.

Spectral and Diffusion Parameter Correlations

Table 3.4 shows significant correlations between median diffusion and spectral parameters in all of the regions of interest.

Table 3.4. Correlations of diffusion and spectral parameters

Region	Correlation of spectral parameters and nANI (r,p)	Correlation of spectral parameters and nADC (r,p)
CEL (n=12)		Cho & nADC (r = -0.80, p<0.001) CNI & nADC (r = -0.83, p<0.001)
NEL (n=32)	NAA & nANI (r = 0.37, p = 0.04)	Cho & nADC (r = -0.52, p < 0.001) Cr & nADC (r = -0.65, p < 0.001) NAA & nADC (r = -0.67, p < 0.001)
CNI2 (n=31)	NAA & nANI (r = 0.35, p = 0.05)	NAA & nADC (r = -0.56, p < 0.001)
CNI3 (n=28)	Cr & nANI (r = 0.43, p = 0.02)	Cho & nADC (r = -0.46, p = 0.01) Cr & nADC (r = -0.71, p < 0.001) NAA & nADC (r = -0.81, p < 0.001)
CNI4 (n=29)	Cr & nANI (r = 0.4, p = 0.03)	Cho & nADC (r = -0.53, p < 0.001) Cr & nADC (r = -0.67, p < 0.001) NAA & nADC (r = -0.68, p < 0.001)

r: Spearman rank correlation coefficient, p: p value

Cho was negatively correlated with nADC in all of the abnormal regions except the CNI2 region. Cr was negatively correlated with nADC in the NEL, CNI3 and CNI4, and positively correlated with nANI in the CNI3 and CNI4. NAA was negatively correlated with nADC in all of the regions but the CEL, and was positively correlated with nANI in the NEL and CNI2. The CNI was negatively correlated with nADC in the CEL.

Discussion

All grade 3 gliomas examined in this study showed T2 hyperintensity, with moderate CE in 18/32 patients. When present, the CEL resided mostly within the metabolically abnormal regions, but these regions were not fully conjoint. This is consistent with the findings of Pirzkall et al (33). The CEL appeared to have the highest density of tumor cells, based upon highest Cho and lowest NAA among all of the tumor sub-regions. Similarly, the CEL region also had the lowest nADC compared to the NEL region and the metabolically abnormal areas, suggesting that increased tumor cellularity might be limiting the free water diffusion in this region. Highest LL and lowest Cr levels were also observed in the CEL, suggesting that this region was also the most hypoxic. The CEL also had lowest nANI, suggesting that the degree of tissue disruption was the highest in that region.

There were 14/32 patients with grade 3 gliomas who were included in our study and showed no visible contrast enhancement. The majority of these patients (13/14) had metabolically abnormal regions with CNI values higher than 2 and 12/14 patients had regions with $CNI \geq 4$. In regions with $CNI \geq 4$ there was relatively high Cho, low

NAA, high LL, high nADC, and low nANI compared with regions with intermediate CNI. This suggested that voxels with high CNI corresponded to regions of tumor with the greatest cellularity or highest proliferative potential. Regions with intermediate CNI values had fairly normal levels of Cho but increasing nADC, decreasing nANI, decreasing NAA, and higher LL when compared to NAWM. This suggested that they correspond to regions where normal brain function and structure is compromised, there is moderate tumor cellularity and poor oxygenation. It should be noted that increasing CNI reflected a reduction in normal neuronal function (decreased NAA) and an increase in cellularity or membrane turnover (increased Cho), which makes CNI likely to be more sensitive in detecting tumor than either Cho or NAA alone. A recent study which investigated correlations between the spectroscopic parameters and histological measures reported that both the ratio of Cho:NAA and the CNI correlated with MIB-1 proliferative index, cell density, and the ratio of proliferation to cell death within non-enhancing grade 2 and 3 gliomas (63).

In the 9 patients who received lactate edited spectroscopy, the CNI4 region was observed to have the highest level of lactate followed by the CEL region. This suggests that they exhibit anaerobic glycolysis and are poorly oxygenated. Combined levels of lactate and lipid (LL) were also very high in these two regions, indicating the possibility that there is some necrosis or hypoxic tissue within these voxels. CNI2, CNI3, and nonenhancing NEL regions also had lactate levels higher than NAWM, indicating poor oxygenation even in areas of relatively lower tumor invasion. This finding suggests that the MRSI data are likely to be more valuable than contrast

enhanced MRI in predicting sensitivity to radiation therapy by delineating poorly oxygenated regions.

Gliomas are known to infiltrate into the surrounding tissue by increasing the extracellular space. It has been hypothesized that the extracellular space (ECS) increases due to deregulation which is caused by loss of gap junctions between glioma cells, shrinkage of cells due to excess chloride in the ECS, tumor invasion, or neuronal cell death due to the excitotoxic effect of glutamate (64). Barriers in the form of overproduction of components of the extracellular matrix (ECM) have also been observed to increase in the enlarged ECS, which serve as a substrate for adhesion and migration of tumor cells through enlarged ECS (64). ADC values are strongly affected by the changes in the extracellular space and the higher nADC values are thought to correspond to an enlarged and edematous ECS. The CEL had decreased nADC values compared to the NEL, indicating possibly more barriers in ECS in the form of tumor cell processes and higher tumor cellularity.

The Cho and nADC were negatively correlated in all of the tumor regions except for the CNI2. This agrees with previous findings (62) and indicates that there is a restriction in the movement of free water as the relative cellularity increases. NAA and nANI were positively correlated in NEL and CNI2 regions, which suggests that tissue structure destruction and neuronal cell loss are concurrent processes and is in agreement with Goebell et al's findings (27). The range of nADC values in CNI2 and the range of nANI and NAA values in CNI3 and CNI4 were both relatively smaller, which might have caused there to be a lack of correlation between the values in those regions. In the NEL, CNI3, and CNI4 there were negative correlations between nADC

and Cr and NAA, which were thought to be a result of a reduction in normal cell density due to the presence of excess edema. Cr and ANI were positively correlated in CNI3 and CNI4, which may have indicated that structural destruction and hypermetabolism followed by hypoxia (24) coexists in these lesions.

The results of the present study suggest that MRSI and diffusion parameters provide complimentary information that may be valuable for characterizing different parts of the anatomic lesion. Edematous regions could be identified by increased water content (high nADC) and minimal disruption in normal tissue function (Cho, NAA which were close to normal). Regions of infiltrative tumor could be differentiated by their increased water content (high nADC), altered normal tissue function (high Cho, low NAA) and structure (low nANI). Regions of macroscopic tumor could be identified by high cellularity (high Cho, low ADC) with major disruptions in the tissue structure and function (low nANI, low NAA) and hypoxia (high lactate or LL, low Cr). This is expected to be particularly important for refining the procedures used to plan radiation therapy, which currently target the entire anatomic abnormality with a homogeneous dose of 60 Gy, delivered over 30 fractions. Our findings showed that grade 3 gliomas have the highest tumor density in contrast enhancing areas but that the CNI4 region is the most malignant focus for non-enhancing lesions, with CNI2 and CNI3 regions being areas of tumor infiltration. Future studies will assess the prognostic importance of these findings and explore the effect of integrating MRSI and diffusion imaging into treatment planning for grade 3 gliomas.

4 . Unaliasing Lipid Contamination for MR Spectroscopic Imaging of Gliomas at 3T Using SENSE

This chapter details a novel post-processing algorithm based on the sensitivity encoding (SENSE) method to reduce the lipid contamination in the MR spectra that happens due to the chemical shift artifact and low bandwidth of selection pulses.

Rationale

Although imaging at high field with multi-channel surface coils presents many advantages, increased chemical shift artifact due to the higher field strength and increased lipid sensitivity may result in aliasing lipid resonances in the spectral field of view (FOV). Lipid may indicate cell membrane breakdown and possible necrosis, but also may be a contaminant from aliasing of subcutaneous fat. Therefore, it is important to accurately localize lipid peaks and distinguish between pathology and aliasing artifacts. Folding of subcutaneous lipid into the selected region may also partially obscure metabolite levels inside the spectral volume of interest, especially lactate and NAA resonating close to the lipid frequency. Previous studies have suggested the use of inversion recovery sequences (65) or Very Selective Suppression (VSS) pulses (44) to suppress, variable density spiral (66) and Echo Planar Spectroscopic Imaging (EPSI) data acquisition strategies (67) to reduce, and spectral spatial pulses to exclude (68) lipid resonances. Post-processing approaches have also

been proposed to remove lipid using time domain fitting (69) or data extrapolation (70).

Spectroscopic data used in this study were acquired using an eight channel RF coil at 3T with Point RESolved Spectroscopy (PRESS) (41) localization along with CHEMical Shift selective Saturation (CHESS) pulses (42) for water suppression and VSS pulses for outer volume signal suppression. It was observed that, even with outer volume suppression techniques there may be residual unwanted lipid resonances. In this study, we propose a post-processing method that uses the sensitivity information of an eight channel phased-array coil and sensitivity encoding (SENSE) (71) for unaliasing lipid resonances originating from in-slice subcutaneous areas from the 3D MRSI of brain in patients with glioma performed at 3T. Simulations and empirical data from a phantom and glioma patients were used to assess the performance of the proposed technique.

Theory

Sensitivity Encoding (SENSE)

Sensitivity encoding (SENSE) (71) is a parallel imaging technique that has been successfully applied for faster MR data acquisition. The data for the SENSE technique is acquired by multi-channel surface RF coils. The signal induced in a surface RF coil varies by the distance between the signal source and the coil. This concept is often referred as the ‘coil sensitivity’. Figure 4.1 shows the coil sensitivity images of a brain slice acquired by the eight channel head coil. The eight coil elements all have a

spatially variant sensitivity to the signal coming from the object. It is possible to see the variation of image intensities, where the pixel intensities are higher closer to a coil element.

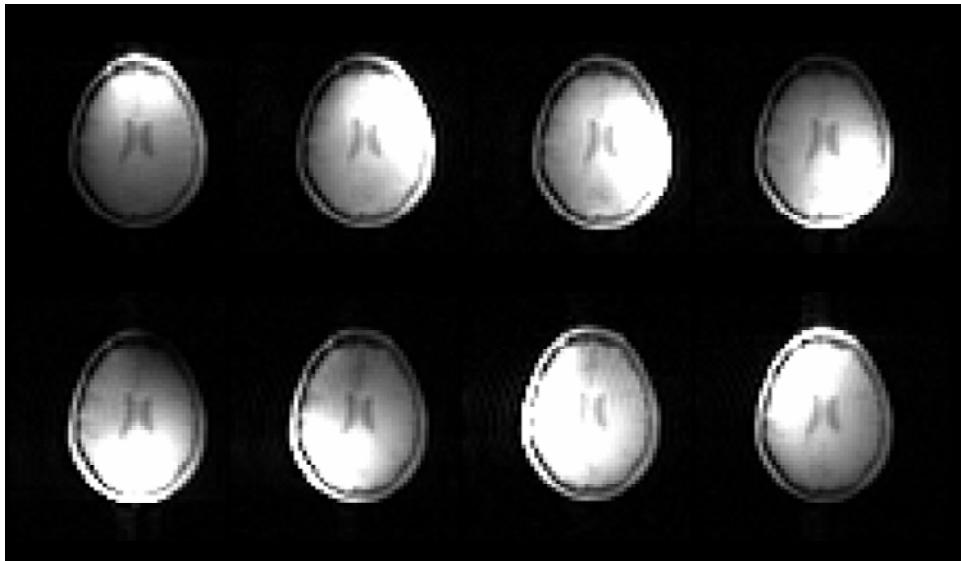


Figure 4.1. The coil sensitivity images of a brain slice acquired by the eight channel head coil.

Although the MR signal, S , is continuous, it is discretely sampled due to MR hardware and software limitations. The signal sampling can be mathematically represented as multiplying the continuous signal intensity with a comb function as,

$$S(\Delta k) = S(k) \times \text{comb}(\Delta k), \quad (4.1)$$

where Δk is the k -space sampling interval.

An image of the object is formed by Fourier transforming the MR signal, and it can be written as,

$$I(x) = FT(S(\Delta k)) \approx \rho(x) * \text{comb}(1/\Delta k), \quad (4.2)$$

where $I(x)$ is the image of the object, ‘*’ is the convolution operator, and $\rho(x)$ is the estimate of the spin density across the object. According to Eq. 4.2, sampling in k -space results in a repetition of the object in the spatial domain. The interval of this image repetition is $1/\Delta k$, or so called the ‘field of view’ (FOV).

The SENSE technique achieves fast data acquisition by reducing the number of sampled points by increasing the k -space sampling interval to cover the whole extent of the k -space. A direct Fourier transformation of this data results in reduced FOV images because of the inverse relation of FOV with the sampling interval. Common reduction factors employed for faster data scans are two and four, which would result in half FOV images in one or two spatial dimensions respectively. If the object that is being imaged is bigger than this reduced FOV, it results in an overlap of the replicated images, or wrapping of the anatomy into the other end of the MR image. This concept is called ‘aliasing’. An aliased image is formed per each coil element, that are later combined to generate the original image. Figure 4.2 shows a schematic of the aliasing phenomenon and Fig. 4.3 shows a sagittal MR image of human head that has aliasing of the nose and the forehead in the back of the reduced FOV head image.

The SENSE data reconstruction is performed on a pixel by pixel basis. For simplicity, reduction factor of two case will be explored in more detail. When k -space data is reduced by a factor of two, each pixel, a , in the resulting aliased image of a coil element is a superposition of two pixels, v_1 and v_2 , that are weighted by their respective coil sensitivities, s_1 and s_2 . This can be formulated as,

$$a = s_1 v_1 + s_2 v_2 . \quad (4.3)$$

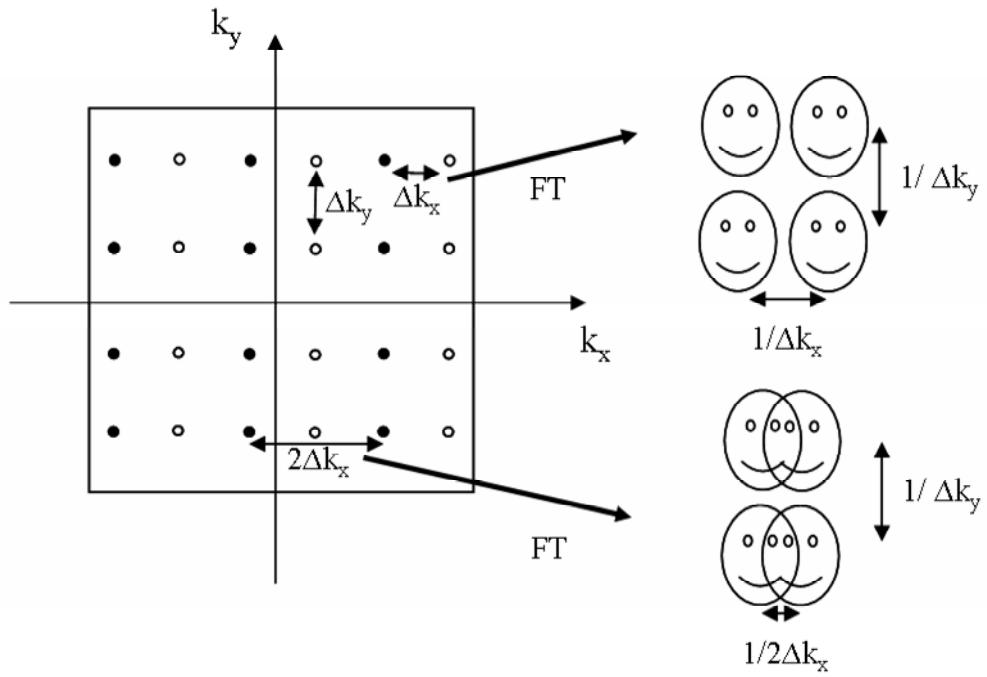


Figure 4.2. Aliasing scheme for SENSE data acquisition.

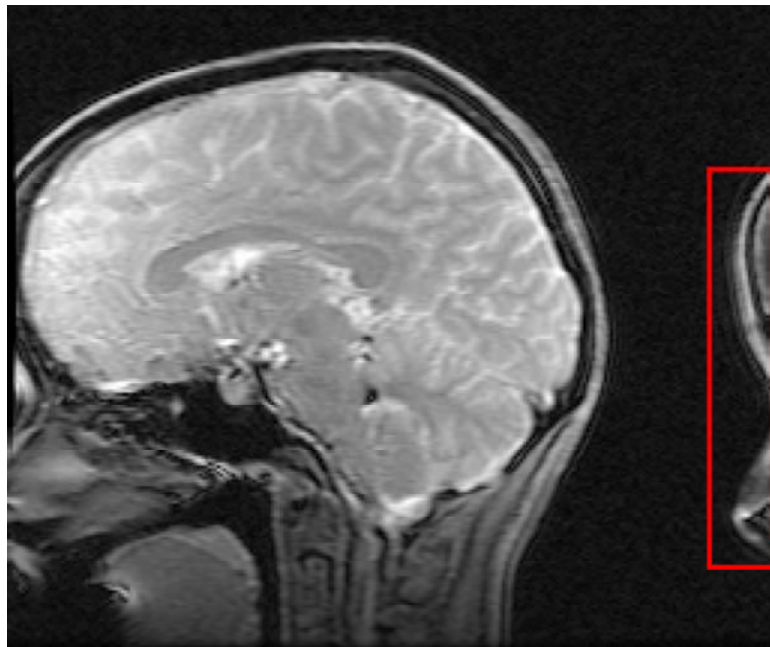


Figure 4.3. Aliasing concept in an MR image. The forehead and nose appear at the back of the head due to reduced FOV.

It is possible to form a linear equation for the data received by the individual coil elements as,

$$A = Sv, \quad (4.4)$$

where A is a $n_c \times 1$ matrix for n_c coil elements including aliased value for the pixel in consideration for all the coils, S is a $n_c \times 2$ matrix with rows of coil sensitivities for the two original pixels, and v is a 2×1 matrix with the original pixel intensities v_1 and v_2 .

To solve this linear equation we can calculate the pseudo-inverse of the matrix S as,

$$U = (S^H S)^{-1} S^H, \quad (4.5)$$

where S^H is the complex conjugate matrix of S. The pseudo-inverse of the matrix S can be extended to include the noise considerations as,

$$v = (S^H \psi^{-1} S)^{-1} S^H \psi^{-1} A, \quad (4.6)$$

where ψ is the receiver noise matrix. The noise receiver matrix is a $n_c \times n_c$ matrix in which a diagonal entry represents the noise variance from a single coil and off-diagonal entries represent the noise cross-correlation between two coils. The noise cross-correlation in two channels, γ and κ , is formulated as,

$$\psi_{\gamma,\kappa} = \frac{1}{2} \left[\sigma^2(\eta_\gamma + \eta_\kappa) + i\sigma^2(\eta_\gamma - i\eta_\kappa) - (1+i)(\sigma^2(\eta_\gamma) + \sigma^2(\eta_\kappa)) \right], \quad (4.7)$$

where σ^2 is the variance operator and η is the noise calculated from the corresponding channel.

Original pixel intensities v_1 and v_2 can be retrieved by multiplying both sides of the equation 4.4 with U as,

$$v = UA. \quad (4.8)$$

The geometry factor, g, was also introduced by Pruessmann et al (71) to estimate the noise amplification due to the data reconstruction using SENSE as,

$$g = \sqrt{(S^H \psi^{-1} S)^{-1} (S^H \psi^{-1} S)} \quad (4.9)$$

This geometry factor can be used to assess the compatibility and performance of different coil designs for SENSE type of parallel imaging applications (72).

Dydak et al. (73) reported the application of SENSE technique for MR spectroscopy, which is essentially a four dimensional version of the same formulation. An image has single pixel intensity, whereas the spectral image can be viewed to have a vector of intensities at the spectral dimension for a given spatial location. SENSE processing is still carried out voxel by voxel for the 3D spatial volume. For the spectral dimension, same unaliasing matrix U can be applied for all of the spectral frequencies at a given pixel location, because coil sensitivities change only spatially.

It is also possible to extend the same formulation for the reconstruction of full multi-channel data. For this case, there would be only one pixel intensity contributing to the spectrum at any given pixel location. v would be changed to single pixel intensity, and sensitivity matrix would only have one column of n_c sensitivity values of each coil element for the given pixel. If the coil sensitivities are real-valued, the conjugate matrix S^H would be same with S. Then, the original pixel intensity v could be estimated as,

$$v = \frac{\sum_{n=1}^8 s_n a_n}{\sum_{n=1}^8 s_n^2} \quad (4.10)$$

The above formula is essentially a coil sensitivity weighted sum.

There are some limitations of the SENSE technique. First, SENSE requires the inversion of matrices having high dimensions that might result in computational errors.

Also, SENSE is computationally expensive, because the unfolding operation is performed for each pixel. Another problem is the possible reconstruction errors due to noise and deviations of the coil sensitivity images. The SENSE reduction factor can not exceed the number of coils. Lastly, SENSE techniques result in an SNR loss that is proportional to $g\sqrt{R}$.

Chemical Shift Artifact and Lipid Aliasing at 3T

It has been discussed in chapter 2 that the electrons create a shielding effect around the protons resulting in frequency shifts depending on the shielding factor σ . Another factor affecting the frequency of a proton is the gradients applied during the RF pulse which adds a spatially varying small magnetic field to B_0 . The frequency of a shielded proton in the presence of a gradient G is defined as,

$$\omega' = \gamma(B_0(1 - \sigma) + G). \quad (4.11)$$

MR pulse sequences employ frequency selective RF pulses for localization, where a band of frequencies are excited. Frequency variations within the excited volume result in spatial misregistration, or the so called ‘chemical shift artifact’.

The PRESS sequence employs one 90° and two 180° pulses played along with gradients to create a true spin echo. These three pulses of PRESS sequence are employed to excite protons that are resonating at predefined frequency ranges. Protons of different spectral metabolites are known to resonate at different base frequencies due to the difference in their electron environments. As a result, the same frequency range of the RF pulses map themselves onto different spatial ranges for distinct

metabolites and result in excitation profiles that are different for each metabolite (43).

The spatial shift in the selected region can be quantified as,

$$\Delta x = \frac{(w - w_o)}{BW_{pulse}} \times (X_{box}), \quad [12]$$

where w is the resonance frequency for the protons of the metabolite of interest, w_o is the center frequency, BW_{pulse} is the bandwidth of the RF excitation pulse, and X_{box} is the width of the excited spectral region.

The range of metabolite frequencies at 3T is twice as large as the frequency range for 1.5 T, resulting in twice as large a spatial shift of the metabolite excitation profiles with similar RF pulses. PRESS pulses used in this study had 2400 Hz bandwidth for the 90° pulse and 933 Hz bandwidth for the 180° pulses. Center frequency is set to be 220 Hz down the water frequency. Assuming an 80 mm spectral box selection with 20% overpressing and 2000 Hz sweepwidth, lipid excitation profile can be estimated to be shifted by 22.6 mm in the 180° pulse direction, and 8.8 mm in the 90° pulse direction from the center frequency excitation profile. Once lipid signals outside the spectral FOV are excited, and suboptimally suppressed by the outer volume suppression pulses, spectral aliasing that is similar to image aliasing is observed as shown in Fig. 4.4.

Lipid Unaliasing Using SENSE

Although the SENSE method was originally proposed for unaliasing reduced FOV images arising from faster data scan approaches, it is possible to generalize the SENSE method to solve any type of image aliasing problems (74,75) , such as ghosting due to phase shift and flow errors in EPI cardiac imaging (75). In each

scenario, it is necessary to know the specific aliasing pattern to calculate the phase shift amount resulting in the spatial misregistration.

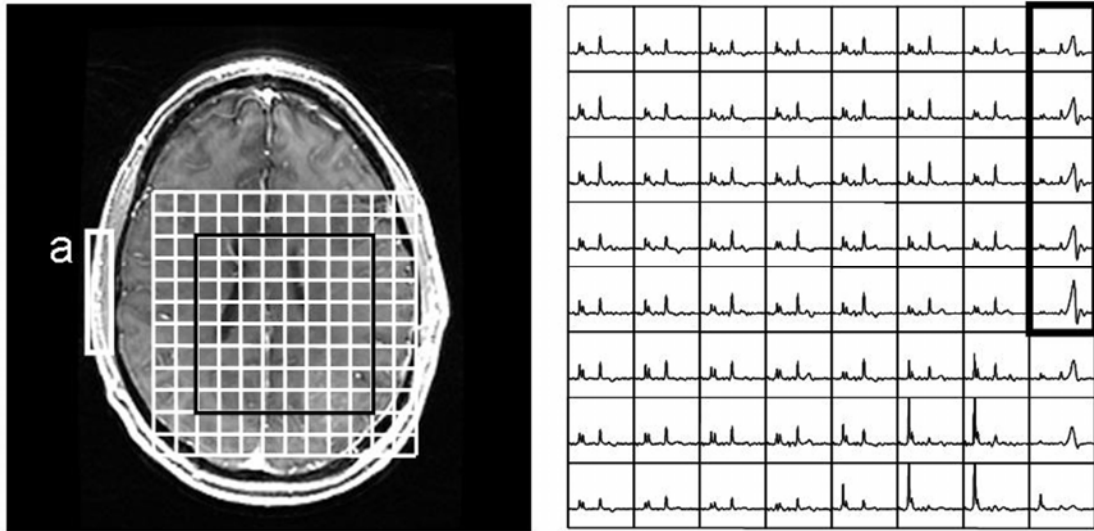


Figure 4.4. Example of the lipid aliasing problem in MR spectra. Left: T1 weighted SPGR image with the spectral FOV (white grid), and the PRESS selected region (black box within the grid). Right: MR spectra from the PRESS selected region. Spectral voxels marked with the black box have aliasing lipid resonances coming from the scalp region a FOV away within the white box marked with (a) on the image.

MR spectroscopy usually employs a small FOV for time considerations. This leads to the aliasing of subcutaneous lipid into the spectral FOV, as described in the previous section. Lipid resonances outside the FOV fold into a voxel within the spectral array that is a FOV away from that lipid voxel. Lipid unaliasing was implemented by treating the original spectral array as a half FOV representation of an extended spectral array.

A software program was implemented to remove the in-plane aliasing lipid resonances from the spectral array using Matlab 6.5 (The Mathworks Inc., Natick, MA). The reduction factor was assumed to be four for all the voxels consistent with

the observed aliasing pattern. Using the aliasing pattern information, three voxels that are a FOV away from a given voxel in the x and y directions were checked, and the ones within the head region were selected yielding the total number of aliased voxels R . The original and aliased voxels were resolved using resampled coil sensitivities and the SENSE methodology. Specifically, the sensitivity matrix S was constructed from the coil sensitivities for the R voxels contributing to the observed voxel intensity. The resulting spectral array had twice the original FOV in the in-plane directions, and included the subcutaneous lipid areas. Figure 4.5 shows an example of the lipid unaliasing for a voxel at an axial slice of a glioma patient spectra.

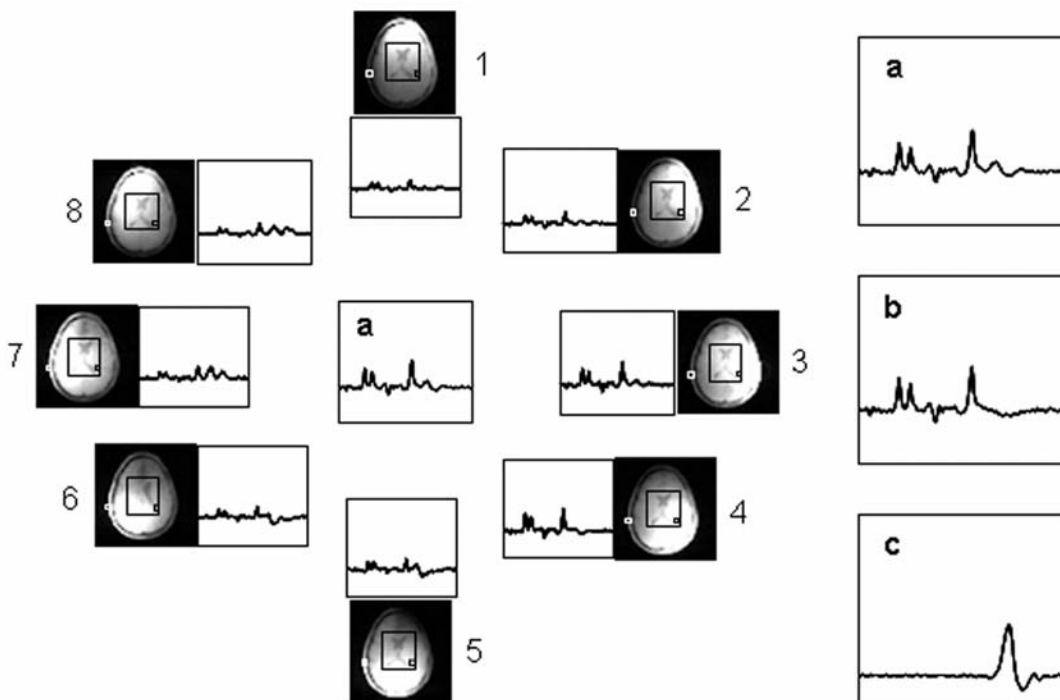


Figure 4.5. Example of lipid unaliasing for a voxel. Coil sensitivity images of a slice along with the spectrum from the black voxel are shown. (a) Conventional combination of the spectra using the coil sensitivity weighted sum results in aliasing lipid resonances. (b) Unaliased spectrum of the black voxel. (c) Unaliased lipid spectrum placed into the white voxel.

The eight channel coil sensitivity images are displayed along with the spectra acquired by that coil element from the black voxel marked on the images. The coil sensitivity weighted sum of the eight individual spectra is shown in the voxel marked with 'a'. It is possible to observe that Cho, Cr, and NAA peak heights varied linearly with the coil sensitivities at the black voxel, having much higher intensities at the closer coil elements. The lipid peak height of the black voxel was not consistent with the expected pattern, and it was observed that lipid height was much more in the coils numbered 6 and 7 compared to the coils 3 and 4 which were closer to the voxel. This indicated that the lipid peak observed in the black voxel was probably not resident, and was coming from an aliasing voxel. The lipid unaliasing algorithm resolved this problem, and unaliased the spectrum marked with 'b' for the black voxel, and the lipid spectrum marked with 'c' for the white voxel located a FOV away in the RL direction from the black voxel. This result confirmed that the unaliased lipid spectrum originated from an in-slice scalp and skull region.

Methods

Data Acquisition

Spectroscopic imaging experiments were carried out on a uniform MRS phantom and 12 glioma patients (6 Grade II, 1 Grade III, 5 Grade IV, 6 male, 6 female, mean age = 47) on a 3 T GE Signa EXCITE scanner (GE Healthcare, Milwaukee, WI)

equipped with an eight channel RF coil (MRI Devices Inc, Gainesville, FL). Informed consent was obtained from the patients prior to scanning.

The MRS phantom contained major metabolites observed in the brain, which were Cho, Cr, NAA, and lactate, and a balloon filled with cooking oil that was attached to one side of the phantom to create an artificial lipid environment. The imaging protocol included the acquisition of T1-weighted 3D SPGR (TR=26 ms, TE=3 ms, 3 mm slice thickness, 256x256 matrix, FOV=240x240 mm, flip angle = 40°), T2-weighted FLAIR (TR=10002 ms, TE=127 ms, TI=2200 ms, 3 mm slice thickness, 256x256 matrix, FOV=240x240 mm, flip angle=90°), and proton-density weighted fast gradient echo coil sensitivity images (TR=150 ms, TE=2.1 ms, 3 mm slice thickness, 64x64 matrix, FOV=300x300 mm, flip angle=20°). ¹H 3D MRSI data was acquired using PRESS volume localization with CHESS water suppression and VSS outer volume suppression. The desired PRESS volume and a 1.2 overpress region were excited to reduce the effects of chemical shift artifacts on relative peak intensities. The spectral array dimensions were 12x12x8 (n=4) or 16x16x8 (n=8) with 1 cc nominal spatial resolution. The rectilinear *k*-space sampling was restricted to a central ellipsoidal region to reduce the scan time to 9 min for the 12x12x8 and 17 min for the 16x16x8 arrays with TR=1.1s. The phantom and patient spectra were acquired with TE=144 ms, and four patients with 12x12x8 spectral array size also had another spectral acquisition with TE=40 ms for long and short echo time spectral comparison.

Data Simulations

MR brain images and spectra were simulated as described previously (47). Head images were simulated as a sum of the scalp and the brain regions. Scalp images were generated as the intersection of two ellipsoids with respective axes lengths of (170, 200, 160) mm and (150, 180, 140) mm. Brain images were generated as an ellipsoid with axes lengths of (140, 170, 130) mm. Two smaller ellipsoids were defined in the brain region to represent the ventricles with (10, 50, 20) mm axes lengths. Four different spectra were simulated in the same coordinate system as the head images with $24 \times 24 \times 16$ matrix size and $FOV = 240 \times 240 \times 16$. PRESS excitation pulse bandwidths were simulated as 933 Hz for RL and SI, and 2400 Hz for AP directions, and the chemical shift effect was also included into the simulations. The spectral datasets were generated with the default VSS band thickness of 30 mm and overpress factors of 1.2, 1.3, and 1.4. An additional dataset was generated with a VSS band thickness of 40 mm and overpress factor of 1.2. Random Gaussian noise was added to the spectra to generate NAA SNR levels of 20, 40, and 60, resulting in 12 different spectral datasets. Spectra acquired by different elements of the eight channel phased array coil were simulated by multiplying the resulting simulated spectra and the coil sensitivity maps resampled from phantom coil sensitivity images. Half of the phase encode steps were removed from the in-plane directions at the last step to generate a $12 \times 12 \times 16$ matrix size spectra with in-slice aliasing problems.

Data Processing

Proton density weighted coil sensitivity images for each of the eight coil elements were acquired with a FOV of 300×300 mm encompassing the whole head region.

Combined coil sensitivity images were also computed as the square root of the sum of squares of the individual coil sensitivities for each slice. Although the coil sensitivity maps were acquired with the proton density weighting, there were still some anatomy related non-uniformities such as darker ventricle and skull regions. For unfolding the lipid we anticipated that accurate coil sensitivity estimates were necessary in the scalp and skull region, which were the main lipid containing regions. A software program was implemented using Matlab 6.5 (The Mathworks Inc., Natick, MA) to reduce the anatomy related inhomogeneities of the coil sensitivity maps. The edges of the brain were found from the combined images using the Canny method to create a mask of the anatomy. Sensitivity images of the individual coil elements and the combined images were masked. Individual coil images were then divided by the combined images. The resulting images were filtered with median and low-pass homomorphic filters consecutively to smooth the image discontinuities. Coil sensitivities were resampled to twice the spectral resolution for the in-plane directions. The images were dilated by a 3x3 kernel to preserve the edges of the image before resampling. Figure 4.6 shows an example slice of the coil sensitivity images before and after the coil sensitivity correction.

Spectra from the eight coil elements were individually processed in parallel on a Linux cluster using software developed in our laboratory (47). Data processing was slightly modified for the higher field strength, and the spectra were filtered by a 4 Hz Lorentzian filter.

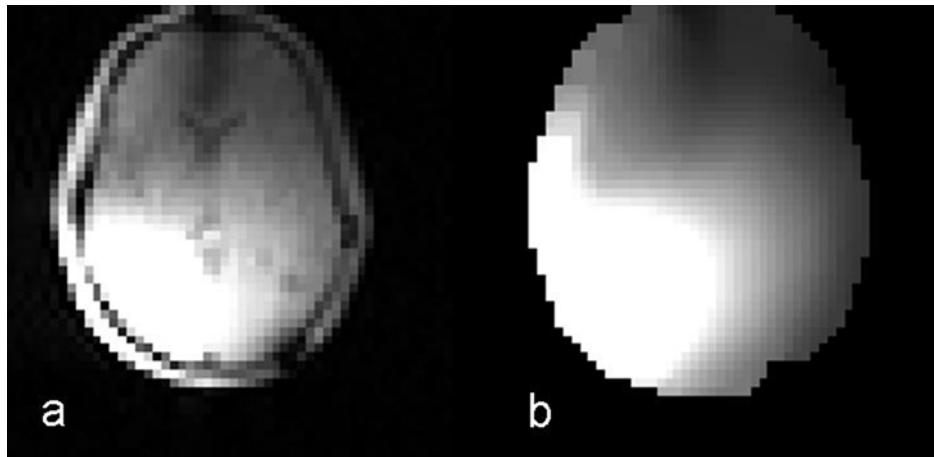


Figure 4.6. A slice from the coil sensitivity images before (a) and after (b) the coil sensitivity map correction.

Multi channel reconstructed spectra were combined using coil sensitivity weighted sum (referred to as the aliased result), and the lipid unaliasing routine (unaliased). Two sets of spectra were generated for each combined data: one by phasing on the Cho peak and the other by phasing on the lipid peak to get accurate estimates of the lipid amount in aliased voxels without affecting the other metabolite levels. Spectral peak heights were determined from these individually phased spectral sets. Phantom data had smaller lipid peaks than the other metabolite peaks. Lipid contaminated voxels were determined by selecting the voxels with a lipid peak height higher than the mean choline height for the patients' data, and higher than one fourth of the mean choline height for the phantom data within the selected PRESS box. Lipid heights were normalized with the mean choline height within the PRESS box for both the aliased and unaliased datasets. A Wilcoxon sign rank test was used to assess if the levels of normalized lipid within the contaminated voxels were significantly reduced by utilizing the unaliasing routine. A p value of less than 0.05 was considered significant.

Noise from the last 20 points of the spectra in the central $7 \times 7 \times 3$ voxels in the spectral array were used to calculate the noise receiver matrix. For each spatial location, the noise receiver matrix was estimated using Eq. 4.7. The final noise receiver matrix was calculated by averaging the noise receiver matrices of the selected central 147 voxels. Geometry factor maps were created using Eq. 4.9.

Results

Elements of the eight channel RF coil had been overlapped to minimize the mutual inductance among neighboring elements and low impedance preamplifiers were utilized to minimize the interaction with the next nearest and distant neighbors (76). Inductive decoupling solenoids were also present to further reduce coupling between an element and the next nearest neighbor. It was observed that the noise receiver matrix had high intensities ranging from 0.54-1 for the phantom, and 0.72-1 for an example glioma patient data in the diagonal entries, and much smaller values ranging from 0.08-0.34 for the phantom, and 0.004-0.27 for the glioma patient data in the off-diagonal entries. This indicated that the coils were minimally coupled.

Figure 4.7 shows the geometry factor maps that were calculated from a slice of a patient dataset before and after masking the coil sensitivity maps on the left and center, respectively, and after the coil map correction algorithm was applied on the right. Our findings confirmed that geometry factors were very high before masking the coil sensitivity images (72) with a local maximum of 24.16, because the true degree of aliasing was not correctly estimated. Geometry factors in the central 25 voxels of the brain ranged from 1.67-5.70. After masking, it was observed that the geometry factors were smaller with a range of 1-1.27 within the head region.

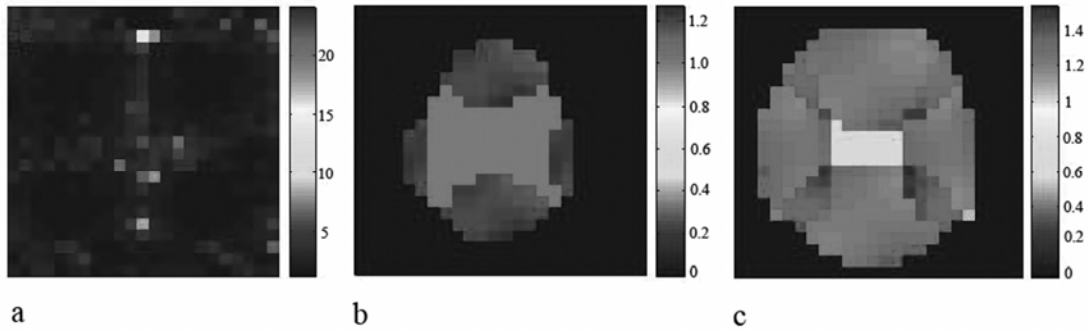


Figure 4.7. Geometry factor maps before (a) and after (b) masking the object region, and after the full coil sensitivity map correction (c).

The coil sensitivity correction algorithm was necessary to reduce anatomy related non-uniformities in the coil sensitivity images, and preserve the edges of the head region, so that lipid unaliasing could be successfully applied. It was observed that the coil sensitivity correction increased the geometry factors, especially in the coil overlapping sections, but the maximum value still stayed under 1.55, which was regarded as being relatively favorable. These findings indicated that the eight channel head coil setup was suitable for parallel imaging applications.

Simulation studies were used to assess the effect of several spectral data acquisition parameters. The results showed that with the given geometry, subcutaneous lipid was excited with overpress factors of 1.2 and above, and excited lipids were not completely suppressed by the default VSS saturation band thickness of 30mm. Total normalized lipid heights of the original aliased and lipid unaliased simulated spectra are shown in Table 4.1. SENSE unfolding significantly ($P < 0.05$) reduced the normalized lipid heights in all the simulated signals created with a VSS band thickness of 30 mm.

Table 4.1. Total normalized lipid heights from the aliased and unaliased simulated spectra. (OP: overpress; L(A): normalized lipid heights of the aliased spectra; L(UA): normalized lipid heights of the unaliased spectra.)

	<u>VSS=30 mm</u>				<u>VSS=40 mm</u>			
	<u>OP: 1.2</u>		<u>OP:1.3</u>		<u>OP:1.4</u>		<u>OP:1.2</u>	
	$\Sigma L(A)$	$\Sigma L(UA)$	$\Sigma L(A)$	$\Sigma L(UA)$	$\Sigma L(A)$	$\Sigma L(UA)$	$\Sigma L(A)$	$\Sigma L(UA)$
SNR=20	91.74	11.71	110.33	11.93	93.15	14.26	4.47	0.05
SNR=40	90.34	8.35	96.7	10.63	115.46	12.56	1.58	0.25
SNR=60	104.46	7.15	100.74	9.16	104.75	8.9	2.96	0.15

When the VSS band thickness was set to 40 mm with an overpress factor of 1.2, the majority of the excited lipid was suppressed by the saturation bands in this ideal case, and there were smaller amounts of aliased lipid to unfold. In each of the simulation cases, there were small residual lipid peaks left due to imperfect matrix inversion. The lipid unaliasing algorithm was effective for all three noise levels. Figure 4.8 shows an example spectra for the simulated signal before and after lipid unaliasing. The lipid signal inside the black box was significantly reduced after lipid unaliasing.

Figure 4.9 shows the phantom setup along with the spectral selections. An axial slice through the MRS phantom with the lipid balloon attached to the side is shown in Fig. 4.9a. Fourteen lipid contaminated voxels were identified within the PRESS volume. The PRESS excited region for the center frequency is marked with the big white box, and the corresponding lipid excited region due to the chemical shift artifact is marked with the box with dotted lines. Figure 4.9b and d show the spectra within the black box marked on Fig. 4.9a before and after the lipid unaliasing, respectively.

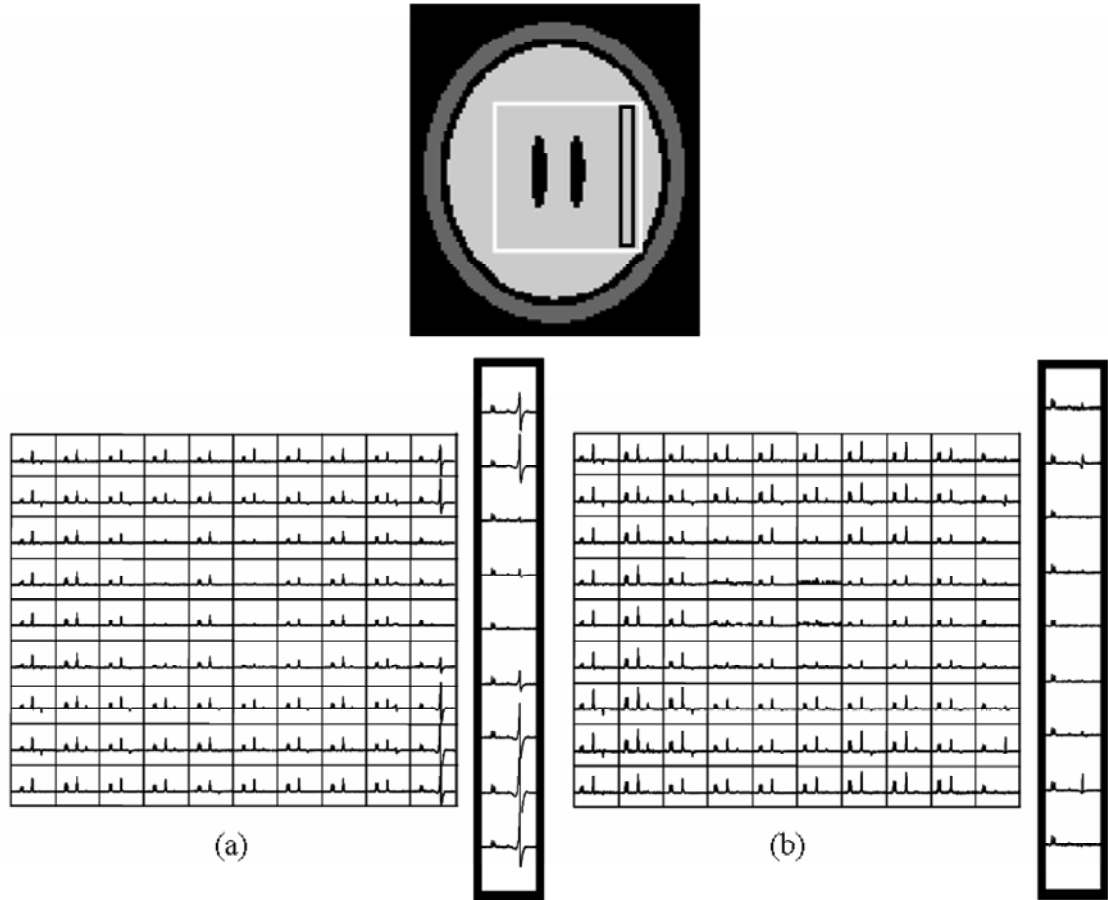


Figure 4.8. An example simulated spectra before (a) and after (b) lipid unaliasing. Spectra from the white box is shown along with the spectra at the last column (black box) zoomed in.

Figure 4.9c shows the lipid spectra within the white grid located on the lipid filled balloon region calculated by the unaliasing algorithm. It was found that the unaliasing routines significantly ($p < 0.001$) reduced the normalized lipid heights within the original spectral FOV. The normalized lipid heights were reduced by a median of $91 \pm 34\%$ (median \pm standard deviation). Maximum and minimum reduction of normalized lipid heights were 100% and 13%, respectively.

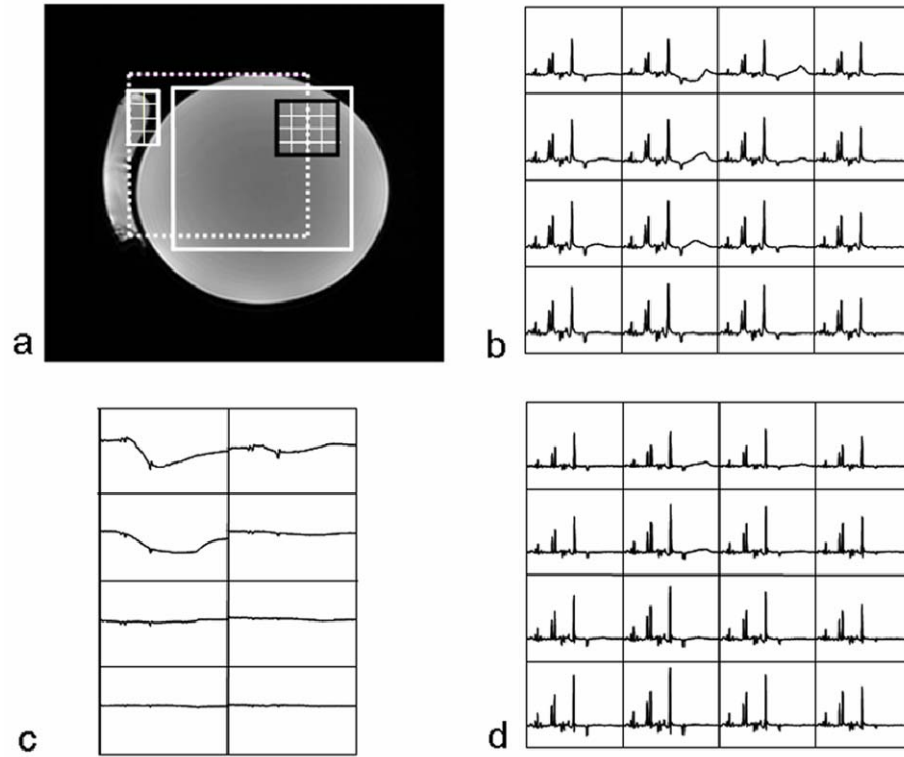


Figure 4.9. (a) Phantom with the lipid filled balloon attached to the left side. The PRESS excited region for the center frequency (white box) and the lipid frequency (dotted box), lipid contaminated region in the PRESS selection (black box), and unfolded lipid regions (small white grid on the balloon) are marked on the image. MR spectra from the black box before (b) and after (d) lipid unaliasing, and the lipid spectra unfolded into the white grid that is a FOV away from the black box region (c) are also shown.

The average number of lipid contaminated voxels across patients for the 12x12x8 array size spectra was 88 ± 37 for the short, and 76 ± 37 for the long echo time. The 16x16x8 array size resulted in much less lipid contamination overall, with an average of 14 ± 12 lipid contaminated voxels. The lipid unaliasing algorithm reduced the total normalized lipid peak height by a median of $41 \pm 7\%$ (min = 29%, max = 47%) for the 12x12x8 short echo time, $45 \pm 10\%$ (min = 41%, max = 63%) for the 12x12x8 long echo time, and $52 \pm 21\%$ (min = 19%, max = 74%) for the 16x16x8 long echo time spectra. Lipid unaliasing was significant ($p < 0.05$) for all four short echo time spectra, and for

ten out of the twelve long echo time spectra. The array size was 16x16x8 for the two cases where the lipid unaliasing was not significant, and the spectra had only one and two lipid contaminated voxels, respectively.

Figure 4.10 shows the spectral results for an example glioma patient case.

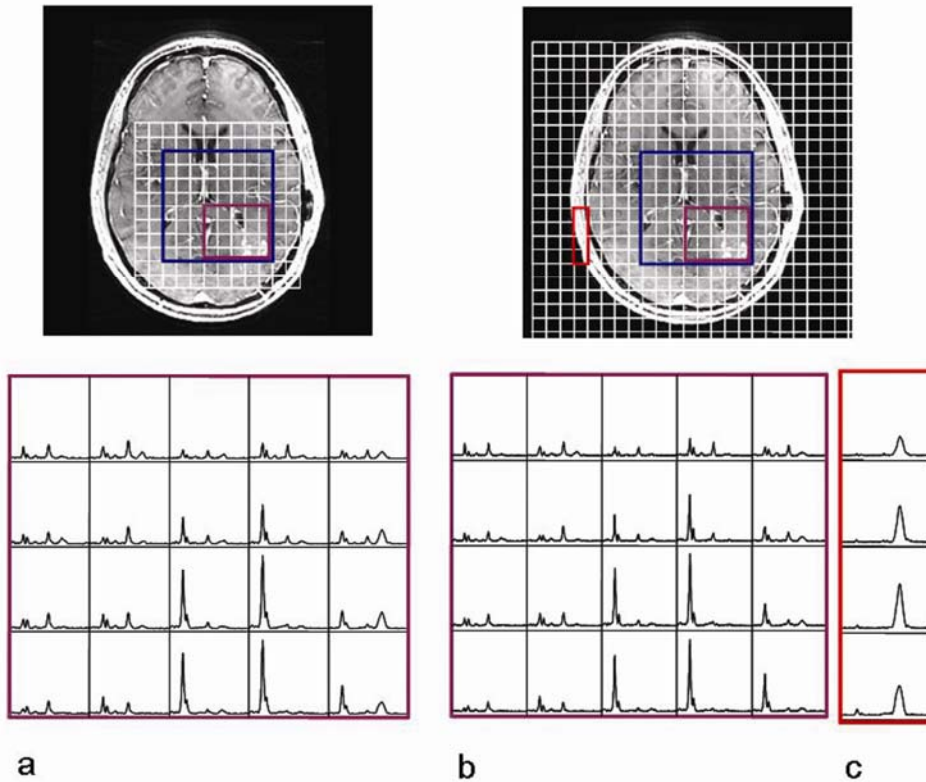


Figure 4.10. An example glioma patient case. Top left: T1 weighted SPGR image of a slice with the spectral FOV (white grid), PRESS selected region (blue box), and a region having lipid contaminated voxels (purple box). Top right: Same image slice with the extended spectral FOV through the unaliasing algorithm (white grid), and the correctly located lipid region (red box). Also shown are spectra of the purple box before (a) and after (b) lipid unaliasing, and the lipid spectra unaliasing into the red box that is a FOV away (c).

The original spectral FOV is shown on the top left, and the extended FOV is shown on the top right image with the white grids. The blue box represents the PRESS excited

volume, and the purple box marks the lipid contaminated areas. Figure 4.10a and b show the spectra obtained from the purple box region before and after the unaliasing procedure, respectively. The small red box in the scalp region on the top right image marks the lipid unfolded areas, and Fig. 4.10c shows the spectra unfolded into this region. The unaliasing algorithm significantly reduced the normalized lipid heights in individual voxels by a median of $40\pm 17\%$ for this patient case. Maximum and minimum reductions of normalized lipid heights at a given voxel were 76% and 10%, respectively.

Discussion

This study has presented a post-processing method for reducing lipid aliasing for 3D MRSI acquired with multi-channel RF coils with small FOV without requiring the implementation of special pulse sequences. The algorithm was effective in removing aliased lipid peaks for simulated and empirical data, and took only 2-3 minutes on a Sun Blade Workstation for a 12x12x8 MRSI dataset. This technique detected aliasing problems and resolved only the aliasing lipids without affecting the other metabolites resonating at similar frequencies, especially lactate. Results from phantoms showed that an underlying lipid peak tail can affect the lactate peak height and area estimates, and that removal of the nonresident lipid peaks would result in more reliable lactate quantification using the frequency domain based methods. Additionally, resident lipids that may be of biological importance would not be affected by this algorithm.

In-slice lipid contamination was observed to be more severe in the RL compared to the AP direction, due to the smaller bandwidth of the current PRESS spectral volume excitation pulse in that direction. In addition to this effect, lipid resonances on

the left side of the PRESS volume were more often excited due to the directionality of the chemical shift artifact. This resulted in more contamination on the right side of the spectral array. A higher bandwidth pulse was played along the AP direction, which meant that the lipid regions in the orbits and the narrowing scalp and skull were minimally excited. An approach to reduce the chemical shift artifact would be to use higher bandwidth volume selection pulses. Spectral spatial pulses that have high bandwidths of 5000 Hz would have reduced the chemical shift artifact by more than 4 times in 180 pulse direction, and 2 times in the 90 pulse directions.

Typical axial brain slices are ellipsoidal in shape with axes lengths of less than 16 cm in RL and 18 cm in AP directions. The usual scalp and skull thickness is 1-2 cm in an axial slice. The lipid aliasing was more prominent for smaller 12x12x8 matrix sizes, because there was lipid containing areas just outside the spectral FOV that were close enough to be affected by the chemical shift artifact. Lipid aliasing was less prominent in the 16x16x8 arrays, because the larger FOV covered the whole head in the RL direction in most cases. The chemical shift artifact was smaller in the AP direction due to the RF pulses as well, resulting in an overall lipid artifact reduction in the 16x16x8 arrays. Although increasing the matrix size is one approach to reduce the aliasing, it does increase the acquisition time. Using a 12x12x8 array provides a significant reduction in scan time and may be valuable for enabling the acquisition of multiple spectral datasets from a patient on the same day. J-difference lactate editing is an example that requires the acquisition of two spectral datasets, whose time limitations requires smaller array sizes. It would also be possible to acquire one short and a long echo time spectra from the same patient within the same time required for one

16x16x8 spectra. The location and size of the PRESS selected region was also observed to have an affect in the presentation of the lipid aliasing. More central and smaller PRESS selections resulted in less lipid excitation in the surrounding scalp and skull regions.

Shorter echo time spectra are desirable due to their higher SNR and better spectral definition of the tissue because it is possible to observe metabolites with short T2 at shorter echo times, like myoinositol, and glutamate and glutamine. For evaluation of neurological diseases it may be important to quantify and analyze these metabolites. The main problem with quantifying short TE spectra is the presence of macromolecules and of higher residual water and lipid signals. These effects result in bigger baseline problems. It was observed that the short TE spectra had higher lipid contamination in more voxels compared to longer echo spectra, but the lipid unaliasing algorithm was similarly efficient in removing the aliasing lipids for both cases.

The lipid unaliasing algorithm may be further improved by reducing matrix inversion errors caused by the possible ill-conditioning of the over-determined system using regularization techniques (77). Regularization methods, like Tikhonov's regularization or the conjugate gradient method, have been proposed to generate approximate objects compatible with the given data by using *a priori* information and energy and bias restrictions explicitly (78). Although regularization algorithms might condition the matrix inversion, it might not solve the problem completely if there are data or system definition related problems. One problem area that could cause the inversion errors would be the use of the original coil sensitivity maps, which are known to have anatomy related contrast diverging from the actual sensitivity values.

By smoothing the coil sensitivity maps as suggested, it is believed that these coil sensitivity related errors have been minimized.

In addition to matrix inversion errors, another reason for there being residual lipid peaks in the empirical data was that the coil geometry meant that our unfolding algorithm could only be applied in two dimensions. The PRESS pulses used in this study had a 180° pulse with 933 Hz bandwidth in the SI direction, and hence the scalp and skull regions in the superior or inferior directions could also cause lipid aliasing. An alternative approach for reducing lipid contamination in the SI direction is to increase the FOV in that direction using alternative spatial encoding, such as echo planar spectroscopic imaging (EPSI). This approach would reduce the acquisition time while still allowing the use of a larger data matrix. The combination of an enlarged FOV and the lipid unaliasing algorithm would further enhance the overall performance on empirical data.

The SENSE algorithm was previously applied for enabling scan time reduction for MR spectroscopy (73), and resolving image aliasing problems (74,75). This study combined these two approaches to resolve the problem of lipid aliasing in the RL and AP directions. Combining the data reduction and lipid unaliasing, and applying the SENSE algorithm twice to solve for both of these two types of aliasing may result in inaccurate results, because it has been recently published that SENSE algorithm might not perform optimally when there is existing aliasing due to small FOV in the data prior to reduction (79). Unaliasing lipid resonances is likely to help in the more reliable quantification of MR spectroscopic data, allow more accurate assessment of

the metabolic state of brain tumor, and improve characterization of changes due to therapy and progression for patients with gliomas.

5 . Quantitative 3D SENSE MRSI in Comparison to Ellipsoidal MRSI of Gliomas at 3T

This chapter details the implementation of the data acquisition and reconstruction of the sensitivity encoding (SENSE) method for fast MR spectroscopic imaging of patients diagnosed with glioma at 3T. The results of the SENSE spectra were quantitatively compared with the clinically accepted ellipsoidal sampling.

Rationale

One limitation of acquiring MRSI data for brain tumor patients is the long minimum data acquisition time for conventional PRESS localized spectroscopy, which is proportional to the total number of phase encode steps. For clinical applications, it is desirable to achieve spectroscopic imaging in less than 10 minutes. Restricting the k -space sampling to acquire low spatial frequency MRSI data in an ellipsoid region of the k -space has been used to achieve a fifty-five percent scan time reduction in clinical setting with good spectral data quality (80). Sensitivity encoding (SENSE) has been another method that was proposed to reduce the scan time for MR spectroscopic imaging (73). SENSE MRSI acquires fewer phase encoding steps and later resolves the resulting aliasing using the coil sensitivity information of the phased array coils. The application of SENSE MRSI has been reported on phantoms and human brain in healthy volunteers (73).

In this study, we implemented and investigated the feasibility of SENSE spectroscopic imaging of brain tumor patients. The second aim of the study was to

compare the signal to noise ratio, nominal voxel size, metabolite intensities and distribution of the SENSE MRSI data with the ellipsoidal and full rectangular k -space sampling in brain tumor patients using an eight channel phased array coil at 3T.

Materials and Methods

Data Acquisition

Five volunteers (5 females, mean age=25) and thirteen patients (11 Grade IV, 1 Grade III, 1 Grade II, 5 female, 8 male, mean age=49) were scanned on a 3T clinical MR scanner (GE Healthcare, Milwaukee, WI) equipped with an eight channel RF coil (MRI Devices Inc, Gainesville, FL). The imaging protocol included the acquisition of axial T1 weighted SPGR (TR=26 ms, TE=3 ms, 3 mm slice thickness, 256x256 matrix, FOV=240x240 mm, flip angle = 40°), T2-weighted FLAIR (TR=10002 ms, TE=127 ms, TI=2200 ms, 3 mm slice thickness, 256x256 matrix, FOV=240x240 mm, flip angle=90°), and proton-density weighted fast gradient echo coil sensitivity images (TR=150 ms, TE=2.1 ms, 3 mm slice thickness, 64x64 matrix, FOV=300x300 mm, flip angle=20°).

All ^1H 3D MRSI data were acquired using PRESS volume localization with CHESS water suppression and VSS pulses for outer volume suppression (TR/TE=1.1s/144 ms, 1cc voxel size). The SENSE spectral acquisition was implemented on the traditional PRESS sequence and data were acquired using a reduction factor (R) of 2 in both x and y directions resulting in a total 4-fold scan time reduction. Three types of ^1H 3D MRSI, which were full (12x12x8 matrix, 21:12 min), ellipsoidal (12x12x8 matrix, 9:28 min) and SENSE (16x16x8 matrix, R=4, 9:28 min),

were acquired for all volunteers. Due to clinical scan time limitations, only ellipsoidal and SENSE spectra were acquired for each patient.

Data Reconstruction and Analysis

Normal appearing white matter (NAWM) regions were selected from the white matter on the contralateral side of the tumor. Contrast enhancing (CE) and regions of hyperintensity on the FLAIR (FL) images were segmented using an in-house semi-automated region growing algorithm (81) for the patients. Proton density weighted coil sensitivity images for each coil element were divided by the square root of the sum of squares of the coil sensitivities from all the coil elements, and smoothed to reduce the anatomy related inhomogeneities by applying median and low-pass homomorphic filters (3).

Ellipsoidal and full spectra from individual coil elements were apodized with a 4 Hz Lorentzian filter, Fourier transformed into spatial-frequency domain and combined using coil sensitivity weighting as described previously (82). SENSE spectra were pre-processed in a similar manner to the ellipsoidal and full spectra to generate aliased spectral images for each coil element. The resulting spectra were unaliased and combined with SENSE spectral data reconstruction implemented using MATLAB 7.0 (The Mathworks Inc., Natick, MA). The spectra were unaliased to generate an array with double the original size (32x32 matrix) to take into account the lipid aliasing problem of small FOV spectroscopy (3). Tikhonov's simple regularized inversion was used to condition the SENSE matrix inversion (77).

For each spectrum, frequency and phase corrections were applied and the water baseline was removed using in-house software (25). The signal to noise ratio (SNR) of Cho, Cr, NAA and lipid peaks were estimated by normalizing their heights with the standard deviation of the spectral noise calculated from the left end of the spectrum. Geometry factor (g) maps were computed for the SENSE spectra to estimate the noise amplification due to the coil geometry. Previous studies have reported a higher nominal voxel size for the ellipsoidal sampling due to the point spread function (PSF) effect (80). The ratio of full to ellipsoidal nominal spectral voxel sizes ($\Delta x_{Full}/\Delta x_{Ellipsoidal}$) was estimated from the volunteer data. Metabolite SNRs of the SENSE spectra were compared with that of the fully and ellipsoidally sampled spectra in volunteers by using the following formula,

$$SNR_{SENSE} * g / \sqrt{time_{SENSE}} = SNR_{Full} / \sqrt{time_{Full}} = SNR_{Ellip} * (\Delta x_{Full} / \Delta x_{Ellip}) / \sqrt{time_{Ellip}}. \quad (5.1)$$

Spearman rank correlation coefficients were computed to assess if the Cho, Cr or NAA ratios between the tumor and NAWM were similar for the ellipsoidal and the SENSE spectra. A Mann-Whitney rank sum test was utilized to assess if the FL and CE regions had significantly higher Cho/NAA values than NAWM for SENSE or ellipsoidal spectra for the patients.

Results

Figure 5.1 shows spectral data from a patient with a glioma that were acquired with the SENSE and ellipsoidal sampling. The data quality and relative metabolite intensities are similar in both cases, with both spectra depicting a region of tumor that

exhibits high Cho and low NAA in comparison with adjacent normal appearing white matter.

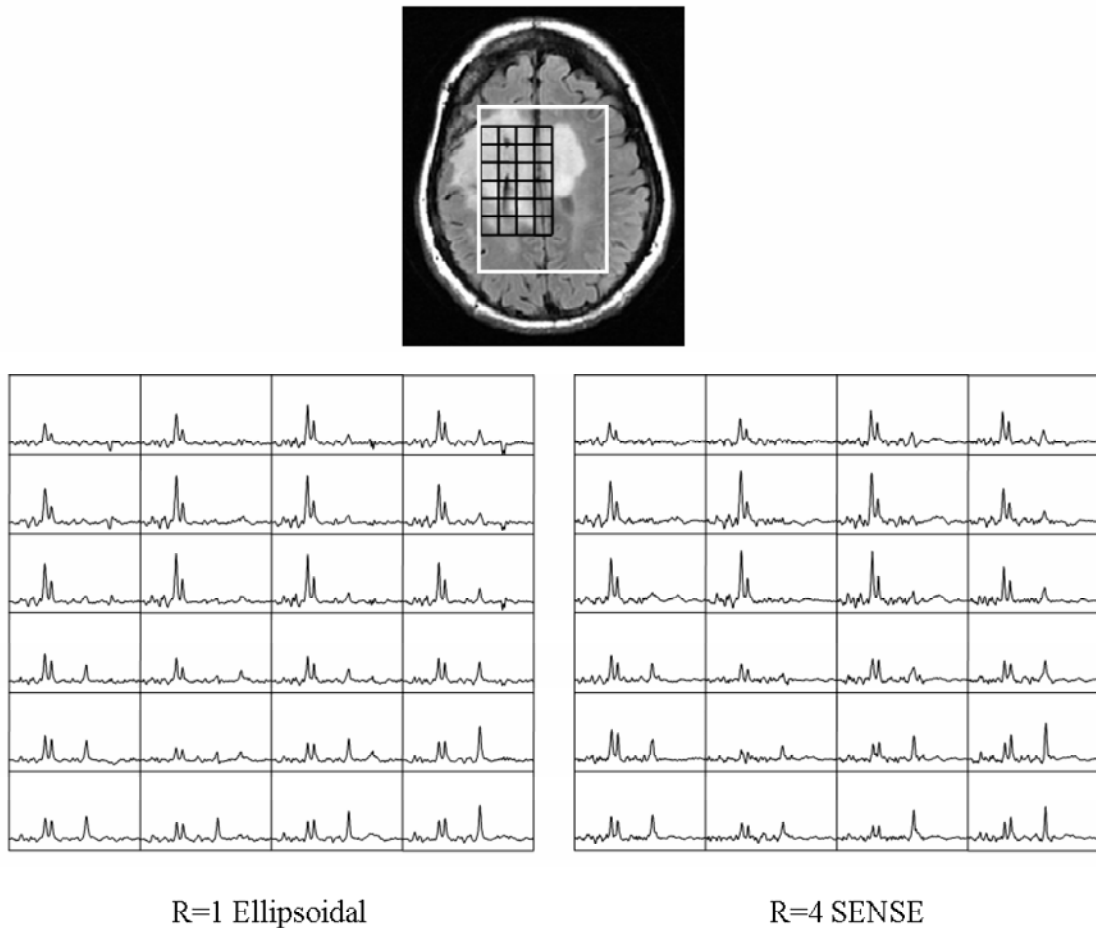


Figure 5.1. Twenty-six year old female patient diagnosed with grade 3 oligodendroglioma. T2 weighted FLAIR image is shown on the top. Spectra from the black grid acquired by ellipsoidal sampling are shown on the left and SENSE with R=4 are shown on the right.

Figure 5.2 shows the SNR values for Cho, Cr, NAA and lipid that were estimated directly from the three kinds of spectra from normal volunteers. The median SNR for Cho, Cr and NAA were (14, 12.2 and 31.2) for SENSE spectra, (34, 29.7 and 73.6) for ellipsoidal spectra and (20.4, 19.8 and 47.4) for the fully encoded spectra. Median

absolute lipid SNR values were below 3 for all three spectral datasets. The median of the geometry factors was 1.59 ± 0.11 (max = 2.38) for unregularized and 1.20 ± 0.09 (max = 1.38) for regularized SENSE spectra for the volunteers and 1.58 ± 0.10 (max = 2.72) for unregularized and 1.21 ± 0.19 (max = 1.87) for regularized SENSE data for the patients.

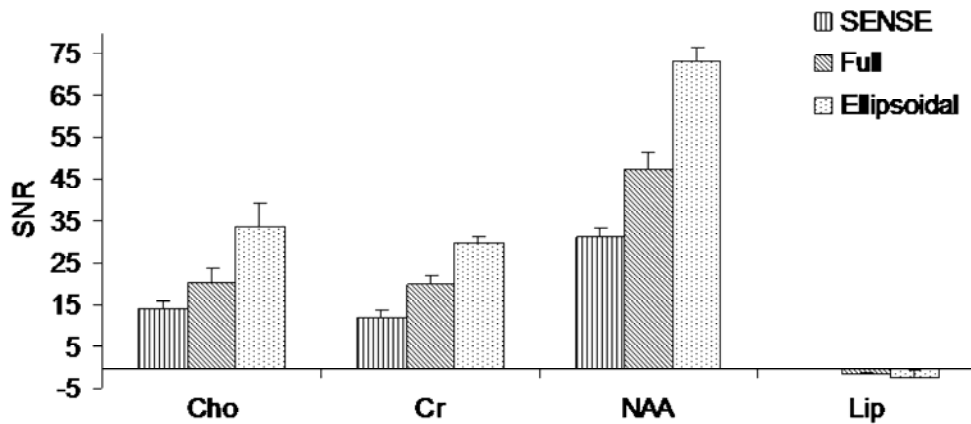


Figure 5.2. Median signal to noise ratios of the major brain metabolites calculated from the three different spectra in the volunteers.

Table 5.1 shows the median ratio of the metabolite intensities calculated from the SENSE and ellipsoidal spectra and the full spectra after correcting for the time difference and the effect of the geometry factor.

Table 5.1 Time and g factor corrected median SNR ratios of the full and regularized and unregularized SENSE and ellipsoidal spectra in the volunteers.

	Cho	Cr	NAA
Full/SENSE _{unreg}	0.98 ± 0.14	0.99 ± 0.14	0.96 ± 0.17
Full/SENSE _{reg}	0.73 ± 0.05	0.75 ± 0.06	0.75 ± 0.06
Full/Ellipsoidal	0.40 ± 0.07	0.41 ± 0.06	0.40 ± 0.07

The median ratio of the full SNR to the unregularized SENSE SNR in volunteers was 0.96 for Cho, 0.98 for Cr, and 0.99 for NAA. This observation suggested that the effective spatial resolution of the SENSE spectra matched that of the full spectra (1cc). Regularization was observed to reduce the noise in the spectra resulting in 30 % higher corrected SNR values for SENSE spectra in comparison to full spectra.

Figure 5.3 displays the NAA SNR calculated from the SENSE spectra versus the full spectra after they were corrected for time difference and the effect of the geometry factors for a volunteer from the whole PRESS box.

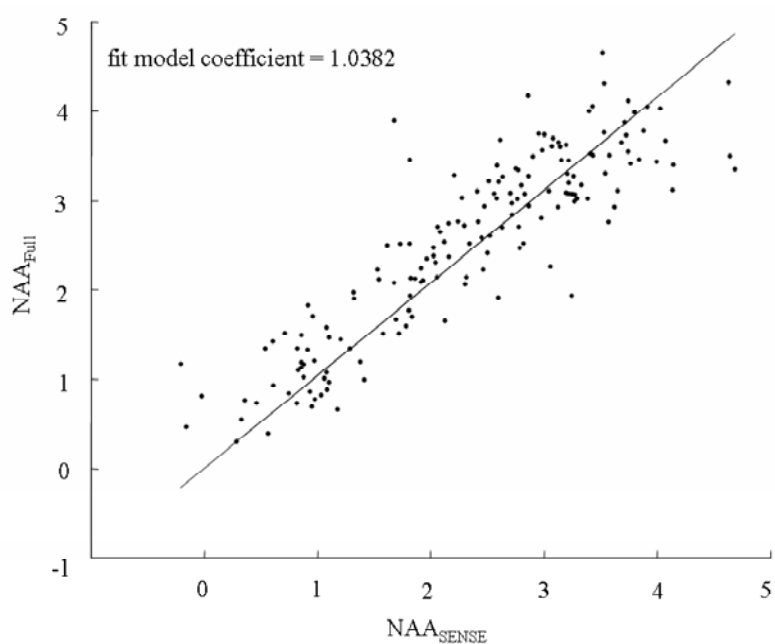


Figure 5.3. Linear fit of the NAA intensities calculated from a volunteer's SENSE versus full spectra. The fit model coefficient was 1.0382 indicating high similarity between the intensities calculated from the two datasets.

It was observed that the slope of the regression was 1.0382 in this case, leading to a conclusion that the expected spectral SNR for SENSE was correctly met. The median ratio of the full to the ellipsoidal SNR was 0.40 for Cho, Cr and NAA. This observation suggested that the effective spectral voxel size was 2.5 times larger for the ellipsoidal case than the full case ($\Delta x_{Full}/\Delta x_{Ellipsoidal}=0.40$), which was also discussed in previous studies (80).

Table 5.2 displays the median Cho/NAA values in FL, CE and NAWM regions for the patients as well as the p values of the Mann-Whitney rank sum test to detect the differences of Cho/NAA ratios of tumor and normal regions.

Table 5.2. Median Cho/NAA values in the regions, and the p values of the Cho/NAA difference between NAWM and FL and NAWM and CE regions for the patients.

	Ellipsoidal	SENSE
	Median±std Cho/NAA	
NAWM	0.54±0.07	0.49±0.12
FL	0.96±0.19	0.89±0.18
CE	1.36±0.3	1.26±0.32
	p values	
NAWM versus FL	4.09e-05	2.08e-05
NAWM versus CE	1.07e-04	1.07e-04

Both CE and FL regions had significantly higher ($p<0.05$) Cho/NAA ratios than NAWM for both SENSE and the ellipsoidal spectra. During visual assessment of the spectra for tumor presence, NAWM is often taken as the reference, and the ratio of the peaks in tumor possible regions to the peaks in NAWM region is important. Table 5.3 displays the ratios of the median Cho, Cr and NAA levels in the FL and CE regions versus the NAWM region calculated from the ellipsoidal and SENSE spectra, as well

as their correlations. All metabolite results were highly correlated between the ellipsoidal and SENSE spectra.

Table 5.3. Median ratio of the median values of Cho, Cr and NAA in FL versus NAWM, and CE versus NAWM regions as calculated from the ellipsoidal and SENSE spectra and their correlations for the patients.

		Cho	Cr	NAA
FL/NAWM	Ellipsoidal	0.87±0.23	0.66±0.30	0.41±0.21
	SENSE	0.96±0.41	0.71±0.36	0.41±0.18
	(r,p)	(0.67, 0.01)	(0.65, 0.01)	(0.91, 1.40e-05)
		Cho	Cr	NAA
CE/NAWM	Ellipsoidal	0.77±0.29	0.44±0.26	0.23±0.12
	SENSE	0.81±0.43	0.46±0.23	0.24±0.10
	(r,p)	(0.98, 7.76e-09)	(0.95, 1.12e-06)	(0.95, 1.12e-06)

Figure 5.4 displays another glioma patient whose spectra were acquired with SENSE and ellipsoidal methods consecutively. Cho levels were observed to be higher and NAA levels were observed to be smaller in tumor than normal regions. The tumor appeared to be more energetic with high creatine levels. Both spectra depicted the tumor region clearly, and the metabolite peak height distribution was similar for both datasets.

Discussion

SENSE MRSI was implemented for imaging gliomas at 3T, and was quantitatively compared to ellipsoidal k -space sampling which resulted in the same scan time. Spectra obtained using SENSE were calculated to have a better effective spatial resolution than ellipsoidal k -space sampling but were obtained with the same acquisition time.

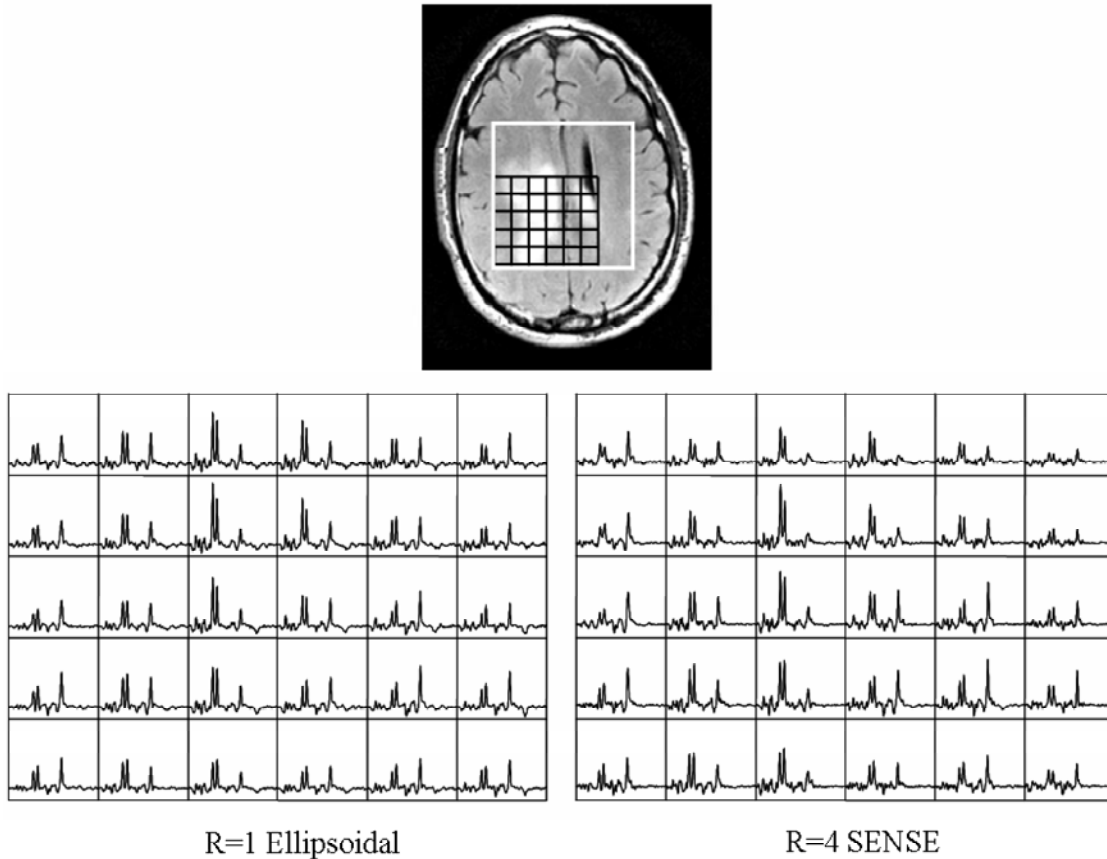


Figure 5.4. 40 years old male patient diagnosed with glioblastomamultiforme. T2 weighted FLAIR image is shown on the top, and ellipsoidal and SENSE spectra from the black grid are shown on the bottom. Both spectra depict similar tumor regions with high Cho and Cr and low NAA.

Previous studies reported a 1.7-fold loss in spatial resolution for ellipsoidal spectra at 1.5 T using a volume head coil (80). Our results indicated a higher 2.5-fold loss at 3T with the eight-channel phased array coil due to the point spread function of ellipsoidal sampling. Both SENSE and ellipsoidal spectra resulted in similar spectral patterns that were well correlated over the PRESS box, and had the ability to distinguish tumor from normal tissue for this patient population.

As anticipated, reducing the scan time did result in a loss in SNR for the SENSE MRSI. The effect of the geometry factor resulted in an additional 1.2-fold SNR loss for the regularized case than would be expected based purely upon scan time. Addition of regularization to the SENSE inversion resulted in noise reduction, and more accurate matrix inversion. Another problem of the SENSE MRSI was residual aliasing of lipid peaks in some voxels. Higher regularization factors were able to reduce the magnitude of residual lipid peaks in the SENSE spectra.

In conclusion, SENSE spectra reduced the scan time from 37:42 min to a clinically acceptable 9:28 min for a 16x16x8 spectral array with better effective spatial resolution than the ellipsoidal sampling, while preserving the interpretability of the brain tumor spectra. Higher magnetic field scanners are becoming more commonly available and SENSE MRSI would benefit from the availability of higher SNR at the high field, and higher reduction factors for SENSE data would be possible. Faster MRSI data acquisition is expected to result in reduced patient discomfort, and motion artifacts as well as higher throughput for the MR scanners.

6 . Simulated Ellipsoidal SENSE and Ellipsoidal GRAPPA MRSI of Gliomas at 3T

This chapter investigates the feasibility of reducing the MR spectroscopic scan time by combining the ellipsoidal sampling with two parallel imaging techniques, SENSE and generalized autocalibrating partially parallel acquisitions (GRAPPA), using simulations.

Rationale

One way of reducing the MRSI scan time has been to restrict the k -space data acquisition to a central ellipsoidal portion (80). This approach reduced the scan time from 37.5 minutes to 17.5 minutes with a repetition time (TR) of 1.1 s for a 16x16x8 array. Although the scan time has been reduced by 50% with this approach, it was still long for a patient to keep still. In this study, we have investigated the feasibility of further reducing the MRSI scan time by sub-sampling ellipsoidally acquired data, and reconstructing these spectra using sensitivity encoding (SENSE) and generalized autocalibrating partially parallel acquisitions (GRAPPA) techniques.

Materials and Methods

Generalized Autocalibrating Partially Parallel Acquisitions (GRAPPA)

The generalized autocalibrating partially parallel acquisitions (GRAPPA) is

another parallel imaging technique that reconstructs the reduced k -space data by least squares fitting in the Fourier domain. The missing k -space lines are estimated as a combination of the acquired additional auto calibration (AC) lines (83). The interpolation weights for an individual coil j are obtained by least square fitting of the acquired lines from all the coils to the AC lines of the j^{th} coil as,

$$S_j(k_y - m\Delta k_y) = \sum_{l=1}^L \sum_{b=0}^{N_b-1} n(j, b, l, m) S_l(k_y - bR\Delta k_y), \quad (6.1)$$

where $S_j(k_y - m\Delta k_y)$ is the signal in the j^{th} coil at $k_y - m\Delta k_y$ position of k -space, b is the number of blocks used for the reconstruction, L is the number of coil elements, and $n(j, b, l, m)$ is the weighting of $S_l(k_y - bR\Delta k_y)$ for synthesis of $S_j(k_y - m\Delta k_y)$. Once the weighting factors are estimated, they are used in generating all the missing lines for a particular coil. In GRAPPA, uncombined images are generated for each coil, and these images are later combined by using the sum of squares method.

Data Acquisition and Preparation

Spectroscopic imaging experiments were carried out on a uniform MRS phantom, 1 volunteer, and 5 glioma patients on a 3 T GE Signa EXCITE scanner (GE Healthcare, Milwaukee, WI) equipped with an eight channel RF coil (MRI Devices Inc, Gainesville, FL). Informed consent was obtained from the volunteer and patients prior to scanning. The MRS phantom contained major metabolites observed in the brain, which were Cho, Cr, NAA, and lactate. The imaging protocol included the acquisition of T1-weighted 3D SPGR (TR=26 ms, TE=3 ms, 3 mm slice thickness, 256x256 matrix, FOV=240x240 mm, flip angle = 40°), T2-weighted FLAIR

(TR=10002 ms, TE=127 ms, TI=2200 ms, 3 mm slice thickness, 256x256 matrix, FOV=240x240 mm, flip angle=90°), and proton-density weighted fast gradient echo coil sensitivity images (TR=150 ms, TE=2.1 ms, 3 mm slice thickness, 64x64 matrix, FOV=300x300 mm, flip angle=20°). ¹H 3D MRSI data was acquired using PRESS volume localization with CHESS water suppression and VSS outer volume suppression. The spectral array dimensions were 16x16x8 with 1 cm³ nominal spatial resolution. The rectilinear *k*-space sampling was restricted to a central ellipsoidal region in order to reduce the scan time to 17 min with TR=1.1s and TE=144 ms.

Spectroscopic data were sub-sampled to simulate a reduction factor (R) of two in *k_x* and *k_y* directions (R=4) for both SENSE and GRAPPA approaches. For the GRAPPA data, 2 full lines of data in *k_x* and another 2 lines in *k_y* were used as autocalibration lines. Figure 6.1 shows the sampled voxels in a given slice for ellipsoidal, SENSE and GRAPPA methods. Black voxels represent the *k*-space data that are not sampled. The white lines in the GRAPPA sampling pattern represent the autocalibration lines. The original ellipsoidal *k*-space sampling acquired 952 out of the full 2048 (16*16*8) voxels within 17:45 minutes with a TR=1.1s. SENSE ellipsoidal datasets were composed of 238 acquired voxels, that would result in 4:36 minutes of scan time. GRAPPA ellipsoidal datasets had 582 acquired voxels that would take 10:67 minutes.

Data Processing and Analysis

Regions of hyperintensity on FLAIR (T2L) images were segmented using an in-house region growing algorithm to differentiate tumor areas (81). Voxels in the PRESS

box outside of the T2 hyperintensity were assumed to represent normal brain (Normal).

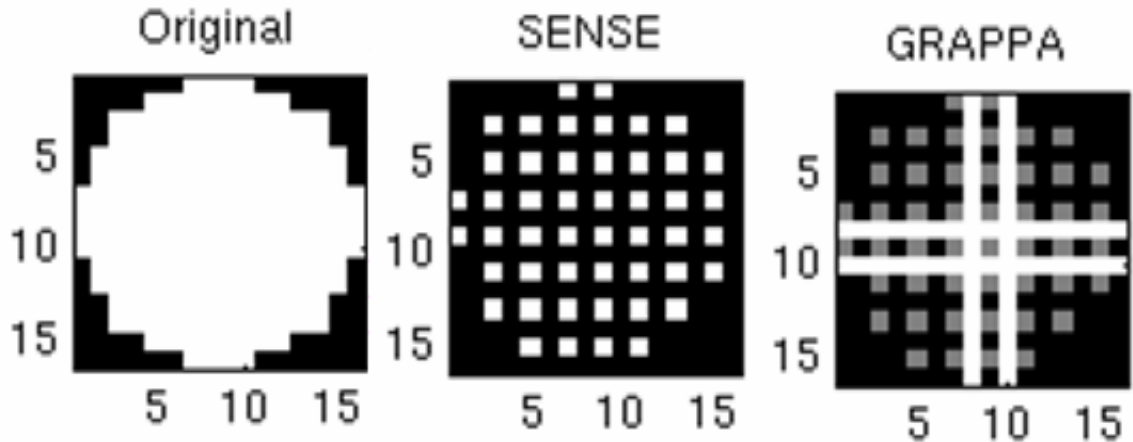


Figure 6.1. The k -space sampling patterns for the ellipsoidal, ellipsoidal SENSE, and ellipsoidal GRAPPA approaches.

Individual proton density weighted images from the coils were divided by their combined sum of squares images. The resulting images were filtered with median and low-pass homomorphic filters consecutively to smooth the image discontinuities. Coil sensitivities were resampled to twice the spectral resolution for the in-plane directions. The images were dilated by a 3x3 kernel to preserve the edges of the image before resampling.

The spectral data for each coil were separately filtered by a 4 Hz Lorentzian filter, and Fourier transformed from k -space to the spatial domain and from time to frequency. After this pre-processing, each voxel was analyzed separately, and the spectra were phased, frequency shifted to match a template peak file, and water baseline was removed using in-house developed software (47). The spectra from each

channel were then combined as a weighted sum using the smoothed coil sensitivity maps.

SENSE reduced ellipsoidal spectra were processed like the original ellipsoidal spectra. The resultant spectral images had aliasing artifact due to their half FOV in both x and y directions. The spectra were unaliased by four fold using the SENSE algorithm (71) developed in Matlab 6.5 (The Mathworks Inc., Natick, MA) as described in Chapter 4. GRAPPA prepared ellipsoidal data were processed by least squares fitting in the Fourier domain to reconstruct the missing k -space lines as a combination of the acquired lines as described earlier in this chapter. A multi-column multi line interpolation (MCMLI) that uses the nearest neighboring points in the unaccelerated direction as well for synthesis of missing lines has been used for GRAPPA fitting (84).

Choline, creatine, and NAA heights were estimated in the frequency domain from the real spectra (47). Lipid peaks often had a different phase than the other peaks if they were a result of aliasing. NAA, and lipid heights were also separately estimated from the absolute spectra, and lipid contaminated voxels were detected as the ones that had $\text{abs(Lip)} > \text{abs(NAA)}$ within the Normal regions for the volunteer and patient data. Signal to noise ratio (SNR) was estimated as the height of a peak divided by the standard deviation of the noise calculated from the right hand end of the spectra. Median Cho/NAA ratios were estimated in the normal and tumor regions. A Spearman rank correlation coefficient was used to detect if Cho/NAA results were correlated between the original ellipsoidal data, and SENSE or GRAPPA reduced ellipsoidal data. P values of less than 0.05 were considered significant.

Results

Table 6.1 lists the SNR values of the three metabolites of interest, Cho, Cr, and NAA and Table 6.2 lists the ratio of the SNR values as estimated from the original, SENSE, and GRAPPA ellipsoidal datasets.

Table 6.1. SNR values of the spectral metabolites for the original, GRAPPA and SENSE ellipsoidal datasets for the patients (median±std).

	Original	GRAPPA	SENSE
Cho	38.43±6.14	28.2±5.92	12.55±2.27
Cr	33.38±8.37	25.6±7.16	10.23±2.96
NAA	59.26±15.47	48.26±13.44	19.06±5.46

Table 6.2. SNR ratios of the metabolites calculated from the original (O), SENSE (S), and GRAPPA (G) median±std ellipsoidal spectra for the patients (median±std).

	O/G	O/S	G/S
Cho	1.33±0.13	3.02±0.25	2.37±0.11
Cr	1.37±0.14	2.98±0.25	2.30±0.11
NAA	1.30±0.13	2.92±0.20	2.31±0.07

SNR is directly proportional to the square root of the data acquisition time. According to the theoretical estimates, the fully sampled ellipsoidal spectra should have had 1.28 ($\sqrt{952}/\sqrt{582}$) times more SNR than the GRAPPA ellipsoidal spectra, and 2 ($\sqrt{952}/\sqrt{582}$) times more SNR than the SENSE ellipsoidal spectra. The theoretical expectation was roughly met for the GRAPPA ellipsoidal spectra. SENSE spectra had almost had one third of the original ellipsoidal SNR which was around 1.5 times less than the expected value. This loss of SNR was due to the noise amplification as a result of the geometry factor effect.

Table 6.3 shows the median and maximum of the g factors for the volunteer, phantom, and patients' spectra. Median of the median g factors was 1.65±0.05 for the patients.

Table 6.3. Geometry factor (g) values for the SENSE reconstruction in tumor and normal regions for the patients and the whole PRESS box region for volunteer and phantom (median±std, and maximum)

	Normal		Tumor	
	median+std	max	median+std	max
Volunteer	1.57±0.15	1.98	-	-
Phantom	1.69±0.34	3.03	-	-
Patient1	1.65±0.20	2.37	1.56±0.11	1.90
Patient2	1.64±0.14	2.26	1.65±0.11	1.87
Patient3	1.7±0.15	2.24	1.57±0.11	1.84
Patient4	1.74±0.17	2.32	1.84±0.18	2.15
Patient5	1.6±0.23	2.33	1.69±0.07	1.91

Table 6.4 shows the total number of lipid contaminated voxels for the original, SENSE, and GRAPPA ellipsoidal spectra. It was observed that both GRAPPA and SENSE increased the amount of lipid within the normal regions of the spectra. But, this effect was more pronounced for the SENSE reconstruction.

Table 6.4. Number of voxels that have an absolute lipid height bigger than the absolute NAA height for the three different data types in the normal regions.

	Original	GRAPPA	SENSE
Volunteer	0	0	5
Patient1	6	23	61
Patient2	0	0	11
Patient3	0	0	5
Patient4	29	50	69
Patient5	1	29	51

Table 6.5 shows the median Cho/NAA within the tumor and normal regions. It was observed that SENSE and GRAPPA results were similar to the original data results for all the cases. All the patients except patient 2 had increased Cho/NAA levels within the tumor region in comparison to the normal regions.

Table 6.5. Median Cho/NAA values within the normal and tumor regions for patients, and within the whole PRESS box for the volunteer and phantom data as calculated from the original (O), GRAPPA (G), and SENSE (S) spectra.

	Normal			Tumor		
	O	G	S	O	G	S
Volunteer	0.48	0.48	0.49	-	-	-
Phantom	0.56	0.57	0.56	-	-	-
Patient1	0.73	0.74	0.69	1.71	1.64	1.69
Patient2	0.62	0.6	0.6	0.63	0.61	0.60
Patient3	0.62	0.64	0.58	1.45	1.09	1.23
Patient4	0.84	0.83	0.82	2.54	1.52	1.72
Patient5	0.53	0.54	0.53	1.25	0.75	0.78

Spearman rank correlation coefficient results showed a significant ($p < 0.05$) correlation of the Cho/NAA ratios between the original and SENSE, and original and GRAPPA ellipsoidal spectra for all the cases within normal regions, and for most of the cases within the tumor regions. Table 6.6 shows all the rank correlation coefficients (r) within normal and tumor regions. Cho/NAA ratio was not found significantly correlated between GRAPPA and original spectra for patient 4, and it was not significant between SENSE and original spectra for patient 5.

Table 6.6. Spearman rank correlation coefficient values (r) for the Cho/NAA ratio correlation in the normal and tumor regions between original and GRAPPA (O & G), and original and SENSE (O & S) spectral results (*: $p < 0.05$).

	Normal		Tumor	
	O & G	O & S	O & G	O & S
Volunteer	0.84*	0.85*	-	-
Phantom	0.4*	0.57*	-	-
Patient1	0.63*	0.68*	0.84*	0.82*
Patient2	0.67*	0.72*	0.66*	0.52*
Patient3	0.69*	0.66*	0.69*	0.8*
Patient4	0.45*	0.44*	0.11, $p=0.6$	0.5*
Patient5	0.66*	0.73*	0.75*	0.26, $p=0.11$

Figure 6.2 shows a slice from the phantom data. T1w SPGR image with the spectral PRESS box and spectral selection is shown along with the three different spectra estimates. It was observed that both techniques resulted in spectra that were similar to the original dataset. GRAPPA had some signal variation across the voxels, and SENSE had some voxels that are not fully unaliased like the top right corner voxel.

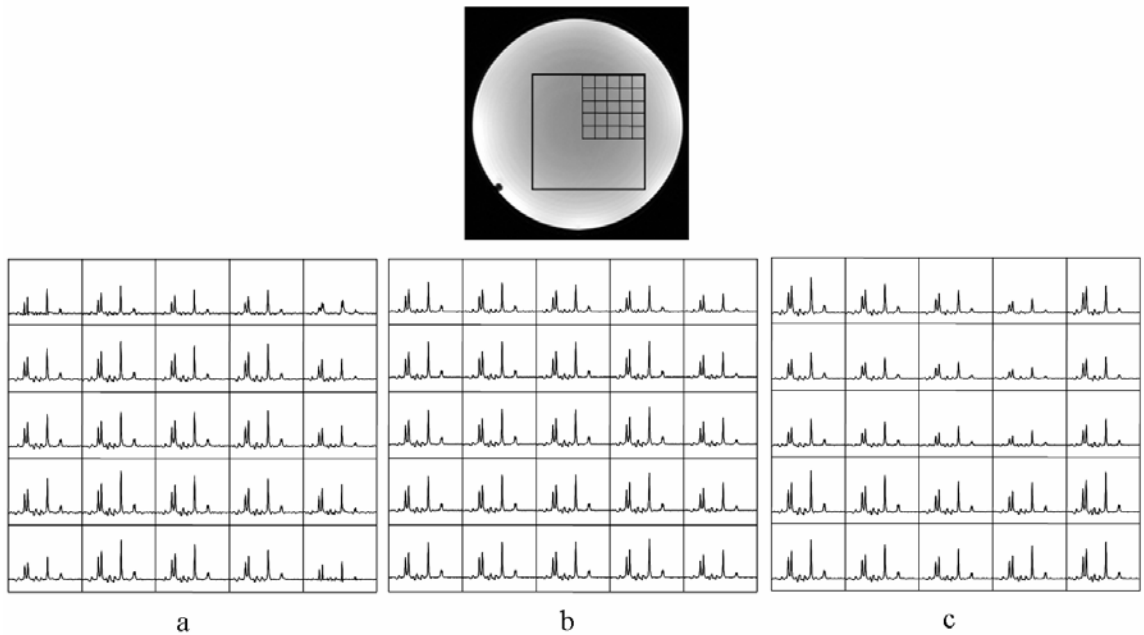


Figure 6.2. T1w SPGR image of the phantom is shown at the top row. a. SENSE, b. Original, and c. GRAPPA ellipsoidal spectra.

Figure 6.3 shows an example patient case. T1w SPGR post Gd, and T2w FLAIR images are shown at the top left and right respectively. The PRESS box is shown with yellow, and the spectra from the black box is shown at the bottom row as calculated from the SENSE(a), original (b) and GRAPPA (c) ellipsoidal data. The voxels marked with gray are the ones that had a CNI [2] value bigger than 2, which are typically considered to be tumor voxels. Both spectra showed higher Cho and lower NAA

intensities for tumor areas as for the original spectra. GRAPPA intensities were lower at the edge of the cavity, and SENSE had a closer approximation of the tumor areas than GRAPPA in this case.

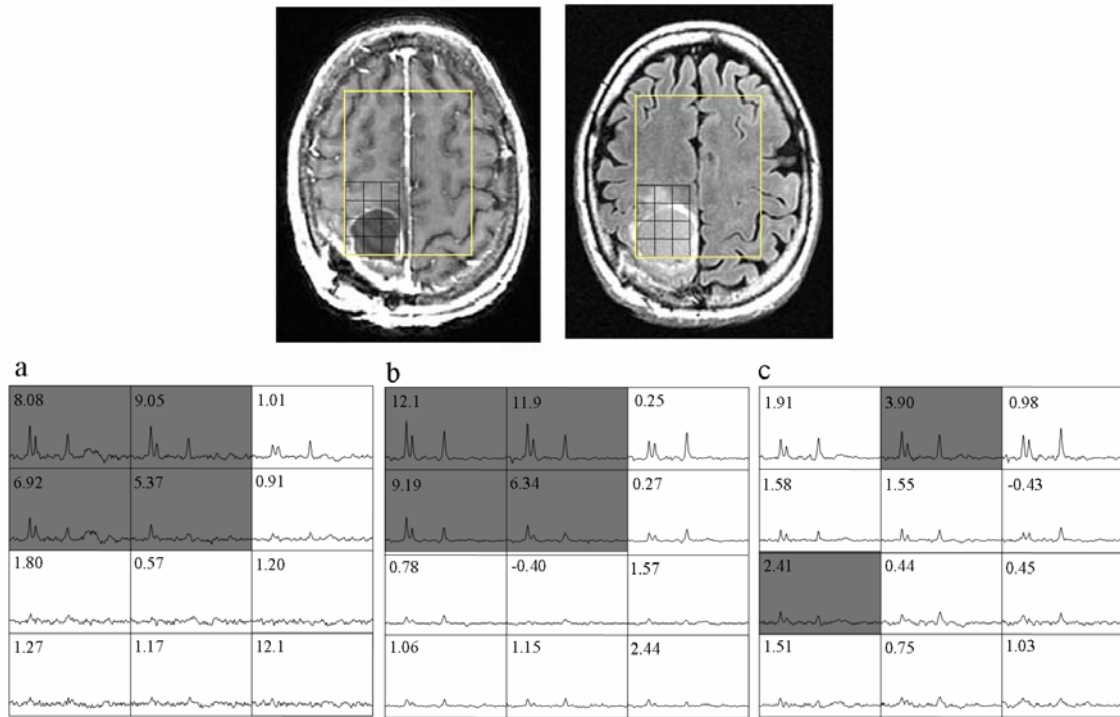


Figure 6.3. Top left: T1w SPGR image, and top left: T2w FLAIR image along with the PRESS box (yellow), and some spectral voxels (black box) for a glioma patient. Spectra from the black box is shown at the bottom row as it was estimated by the SENSE (a), original (b), and GRAPPA (c) ellipsoidal datasets.

Discussion

This study investigated the feasibility of using GRAPPA or SENSE parallel imaging approaches on the ellipsoidally reduced k -space datasets of phantom, volunteer, and patients. Our results showed that both GRAPPA and SENSE ellipsoidal spectra Cho/NAA ratio results had significant correlation with the original ellipsoidal

spectra results. An increased lipid artifact was observed in the SENSE ellipsoidal data, due to imperfect unaliasing. GRAPPA ellipsoidal spectra had more intensity variation across the slices than the SENSE spectra, and it resulted in lower intensities around the cavities for tumors. Both spectra would reduce the MRSI scan time significantly, and would therefore alleviate patient discomfort. Further studies will investigate the reasons of GRAPPA intensity variations, and methods of reducing residual lipid artifact for SENSE. The implementation of the GRAPPA technique could also be improved by acquiring a reduced set of autocalibration lines.

7 . Ellipsoidal SENSE with Effective 9 Fold Scan Time Reduction for Small FOV 3D MR Spectroscopic Imaging of Glioma Patients at 3T

This chapter details the implementation of the data acquisition and reconstruction of the combinatory ellipsoidal SENSE sampling for a nine fold scan time reduction for fast MR spectroscopic imaging of gliomas at 3T. The results were quantitatively compared with the ellipsoidal sampling.

Rationale

Although 3D MRSI provides a vast of molecular information, conventional PRESS localized spectroscopy results in a long data acquisition time ranging up to 30+ minutes. It is desirable to reduce the scan time for MRSI to less than 10 minutes while preserving the data quality for effectively incorporating it into the clinical protocols. Ellipsoidal k -space sampling is a fast MRSI data acquisition strategy, which acquires an ellipsoidal central portion of the k -space and it has been shown to result in accurate spectral definition for imaging brain tumor patients with slightly lower spatial resolution (80). Sensitivity encoding (SENSE) is another fast data acquisition method proposed for reducing the MRSI scan time by acquiring fewer phase encodes, and later resolving the resulting aliasing using the coil sensitivity information of the phased array coils (71,73). Application of SENSE method for spectroscopic imaging of human brain at 1.5 T (73) and glioma patients at 3T (4) has been reported. Other fast MRSI data acquisition methods include echo planar and spiral spectroscopic imaging which utilize readout gradients (85,86). A recent study also reported that combining the

SENSE and echo planar sampling schemes resulted in drastic data acquisition time reduction (87).

Chapter 5 discussed the application of SENSE MRSI in glioma patients at 3T. Chapter 6 presented the feasibility of combining the ellipsoidal sampling with the GRAPPA and SENSE techniques for faster data acquisition on simulations. In this chapter, implementation of a combined ellipsoidal SENSE data acquisition strategy with an effective 9-fold reduction in scan time that results in 4:36 min scan time for a 16cm in plane small FOV (16x16x8) spectral array will be discussed. The feasibility of its application for imaging brain tumors will also be investigated. A quantitative analysis of the resulting SNR, Cho/NAA ratio within tumor and normal regions and comparison of lipid contamination in the ellipsoidal SENSE spectra with that in the current clinical ellipsoidal MRSI protocol will be detailed using phantom, volunteer and brain tumor patient data acquired by an eight channel phased array coil at 3T.

Materials and Methods

Data Acquisition

One phantom, 3 volunteers (2 females, 1 male, mean age =26), and six glioma patients (4 Grade IV, 2 Grade III, 1 female, 5 male, mean age=53) were scanned on a 3 T clinical MR scanner (GE Healthcare, Milwaukee, WI) equipped with an eight channel RF coil (MRI Devices Inc, Gainesville, FL). The imaging protocol included the acquisition of T1-weighted SPGR (TR=26 ms, TE=3 ms, 3 mm slice thickness, 256x256 matrix, FOV=240x240 mm, flip angle = 40°), T2-weighted FLAIR (TR=10002 ms, TE=127 ms, TI=2200 ms, 3 mm slice thickness, 256x256 matrix,

FOV=240x240 mm, flip angle=90°) and proton-density weighted fast gradient echo coil sensitivity images (TR=150 ms, TE=2.1 ms, 3 mm slice thickness, 64x64 matrix, FOV=300x300 mm, flip angle=20°). Ellipsoidal SENSE spectral data acquisition was implemented on the traditional PRESS MRSI sequence with CHES water and VSS outer volume suppression (TR/TE=1.1s/144 ms). Figure 7.1 shows the sampling schemes for the ellipsoidal and ellipsoidal SENSE for a 16x16x8 k -space array.

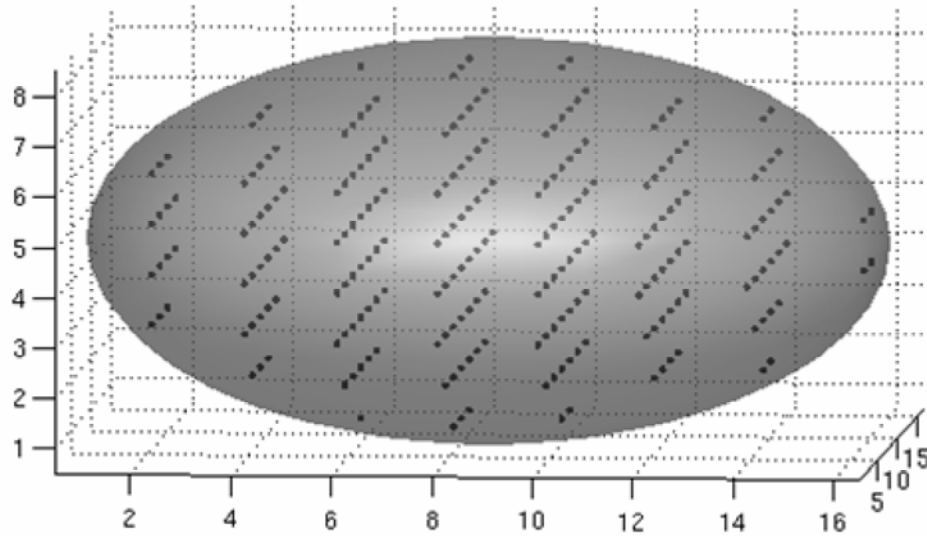


Figure 7.1. Sampling schemes for the ellipsoidal and ellipsoidal SENSE for a 16x16x8 k -space array. The gray ellipsoidal region corresponds to the sampled k -space frequencies for the ellipsoidal scheme, and the black dots represent the k -space points sampled for the ellipsoidal SENSE with $R_x=2$ and $R_y=2$. For ellipsoidal SENSE, only the even points were sampled along both k_x and k_y .

The gray ellipsoidal region represents the k -space sampling area for the ellipsoidal scheme. The black dots represent the k -space points sampled for the ellipsoidal SENSE

($R_x=2$, $R_y=2$), and only the even k -space points were sampled along k_x and k_y . The central low spatial-frequency k -space locations were more fully sampled for both techniques. Ellipsoidal SENSE (16x16x8, $R_x=2$, $R_y=2$, 4:36 min) and original ellipsoidal (16x16x8, 17:32 min) data were acquired with the same FOV from phantom and volunteers. Ellipsoidal spectral array size was reduced to 12x12x8 (9:28 min) for patients due to scan time limitations. The total number of k -space points sampled were equal to 238 (16x16x8) for the ellipsoidal SENSE, and 952 (16x16x8) and 516 (12x12x8) for the ellipsoidal sampling.

Data Reconstruction and Analysis

T2 hyperintensity excluding the cavity areas for the patients were segmented as regions of hyperintensity on the FLAIR (FL) images using an in-house semi-automated region growing algorithm, and were regarded as possible tumor containing areas (81). The brain parenchyma outside the FL abnormality was considered as the normal brain tissue. Proton density weighted coil sensitivity images for each coil element were divided by the square root of the sum of squares of the coil sensitivities from all the coil elements, and smoothed to reduce the anatomy related inhomogeneities by applying median and low-pass homomorphic filters (3).

Ellipsoidal spectra from individual coil elements were apodized with a 4 Hz Lorentzian filter, Fourier transformed into spatial-frequency domain and combined using regular coil sensitivity weighting. Ellipsoidal SENSE spectra were also pre-processed in the same manner as the ellipsoidal spectra to generate aliased spectral images for each coil element. The resulting spectra were unaliased and combined with

SENSE spectral data reconstruction implemented using MATLAB 7.0 (The Mathworks Inc., Natick, MA). The spectra were unaliased to double the original size (32x32 matrix) to take into account the lipid aliasing problem of small FOV spectroscopy (3). Tikhonov's simple regularized inversion was used to condition the SENSE matrix inversion (77). The effect of regularization in data reconstruction was assessed on the previously acquired ellipsoidal spectra of four other glioma patients. Ellipsoidal SENSE sampling was simulated on these datasets and the resulting spectra were reconstructed with and without regularization. The similarity and differences of the regularized and unregularized spectra were investigated.

Frequency and phase corrections were applied for each spectrum and the residual water and baseline was removed using in-house software (47). The signal to noise ratio (SNR) of Cho, Cr, NAA and lipid were estimated by normalizing their peak heights with the standard deviation of the spectral noise calculated from the left end of the spectrum. Geometry factor (g) maps were computed for ellipsoidal SENSE spectra. SNRs of metabolites from the ellipsoidal SENSE spectra were compared with that of the ellipsoidal spectra by using the following formula,

$$SNR_{EllipsoidalSENSE} * g / \sqrt{time_{EllipsoidalSENSE}} = SNR_{Ellipsoidal} / \sqrt{time_{Ellipsoidal}}. \quad (7.1)$$

Lipid contaminated voxels were detected as the ones that had absolute lipid peak height bigger than the absolute NAA peak height within the normal regions for the volunteer and patient data. Spearman rank correlation coefficients were computed to assess the similarity of Cho/NAA ratio between the ellipsoidal and the ellipsoidal SENSE spectra over the whole PRESS selected region. A Mann-Whitney rank sum test was utilized to assess if the tumor regions had significantly different Cho/NAA

values than normal regions for ellipsoidal SENSE or ellipsoidal spectra for the patients.

Results

Table 7.1 reports the effect of adding regularization to the SENSE data reconstruction by comparing the SNR of metabolites, median Cho/NAA ratio and number of lipid contaminated voxels with or without regularization for the simulated patient data.

Table 7.1. The effect of regularization in terms of SNR, median Cho/NAA and the number of lipid contaminated voxels for the simulated patient data.

		SNR			med(Cho/NAA)	# Lipid voxels
		Cho	Cr	NAA		
patient1	Unreg	14.7	12	17.5	0.69	61
	Reg	14.5	12	20.5	0.67	11
patient2	Unreg	17.4	18	29.1	0.6	11
	Reg	25.6	26	45.6	0.59	0
patient3	Unreg	13.2	12	23.3	0.58	5
	Reg	19	16	31.6	0.59	0
patient4	Unreg	14.8	14	27.9	0.53	51
	Reg	19	19	35.9	0.52	4

The median geometry factors were 1.65 ± 0.05 before and 1.33 ± 0.11 after regularization for these data. The SNR of metabolites increased on average by 30% after regularization due to the noise and g-factor reduction. The median Cho/NAA ratio did not change significantly (2-3%) with the addition of regularization. Regularization also resulted in less residual lipid contamination in ellipsoidal SENSE data. This effect was more pronounced in patients 1 and 4 whose spectra had high lipid aliasing.

Table 7.2 reports the SNR of metabolites for the empirical data. The average SNR ratio of the ellipsoidal to the ellipsoidal SENSE spectra for all the metabolites, median of the geometry factors and the expected SNR ratio are also reported. The median of the geometry factors was 1.25 ± 0.04 (max = 1.3) for the volunteers and 1.33 ± 0.11 (max = 1.55) for the patients. The SNR of the ellipsoidal SENSE was slightly higher than the theoretical expectation for all the subjects, because the regularization reduced the noise in the spectra, and affected the noise estimate. Average SNR deviation from the theoretical expectation was 10.5% for the volunteers and 8.5% for the patients.

Table 7.2. The SNR of metabolites and average SNR ratio of the ellipsoidal (E) and ellipsoidal SENSE (ES) along with the median g factor values and expected SNR ratio ($\sqrt{t_{ES}/t_E} * g$) for empirical volunteer (v) and patient (p) data.

	E			ES			Avg(E/ES)	median(g)	Exp(E/ES)
	Cho	Cr	NAA	Cho	Cr	NAA			
v1	29.44	28.72	66.12	15.30	14.50	33.75	1.95	1.30	2.60
v2	39.98	38.28	77.35	19.87	18.30	35.46	2.10	1.23	2.46
v3	34.04	30.76	74.35	17.19	15.89	39.89	1.93	1.25	2.50
p1	33.18	21.24	40.07	17.73	11.90	23.01	1.80	1.35	1.98
p2	19.77	18.55	34.33	10.41	10.32	21.07	1.78	1.28	1.88
p3	24.67	18.62	32.46	13.94	9.98	19.88	1.76	1.55	2.28
p4	17.73	12.55	22.17	9.13	6.98	14.04	1.77	1.44	2.12
p5	31.25	22.98	47.38	21.73	15.03	34.53	1.45	1.27	1.87
p6	23.76	23.78	35.45	13.54	13.68	19.38	1.77	1.31	1.93

Table 7.3 shows the median Cho/NAA ratio for ellipsoidal and ellipsoidal SENSE data and the Spearman rank correlation coefficient and corresponding p-value for the correlation of this ratio over the whole PRESS box for the two spectra. The number of lipid contaminated voxels for all the subjects are also reported in this table. The Cho/NAA ratios of the two spectra were significantly ($p < 0.001$) correlated for all the subjects. Neither the ellipsoidal nor the ellipsoidal SENSE spectra had any lipid contamination for the volunteers. The ellipsoidal SENSE spectra had less lipid contamination than the ellipsoidal spectra for four patients with the same number of lipid contaminated voxels for one patient and two more voxels for another patient.

Table 7.3. Median Cho/NAA ratios for ellipsoidal (E) and ellipsoidal SENSE (ES) spectra, the Spearman rank correlation coefficient (r) and corresponding p-value (p) of this ratio over the whole PRESS box, and the number of lipid contaminated voxels.

	E med(Cho/NAA)	ES med(Cho/NAA)	r	p	E/ES # Lipid voxels
phantom	0.53	0.52	0.9	<0.001	0/0
volunteer1	0.46	0.45	0.82	<0.001	0/0
volunteer2	0.53	0.55	0.73	<0.001	0/0
volunteer3	0.45	0.45	0.88	<0.001	0/0
patient1	0.87	0.83	0.75	<0.001	1/3
patient2	0.55	0.5	0.6	<0.001	1/0
patient3	0.79	0.69	0.25	<0.001	13/8
patient4	0.8	0.71	0.29	<0.001	24/23
patient5	0.68	0.64	0.71	<0.001	1/1
patient6	0.68	0.7	0.79	<0.001	26/13

Figure 7.2 shows the median Cho/NAA ratio within normal and FL abnormality regions for the patients. FL abnormal regions had significantly higher ($p < 0.05$) Cho/NAA for both techniques for the second, third, fourth, and sixth patients. The ellipsoidal spectra had significantly higher ($p = 0.02$) Cho/NAA in the FL abnormal region for the first patient, but the ellipsoidal SENSE spectra did not show a significant difference ($p = 0.17$) between the two regions. The Cho/NAA ratio was not significantly different ($p > 0.05$) between normal and FL regions for both techniques in the fifth patient.

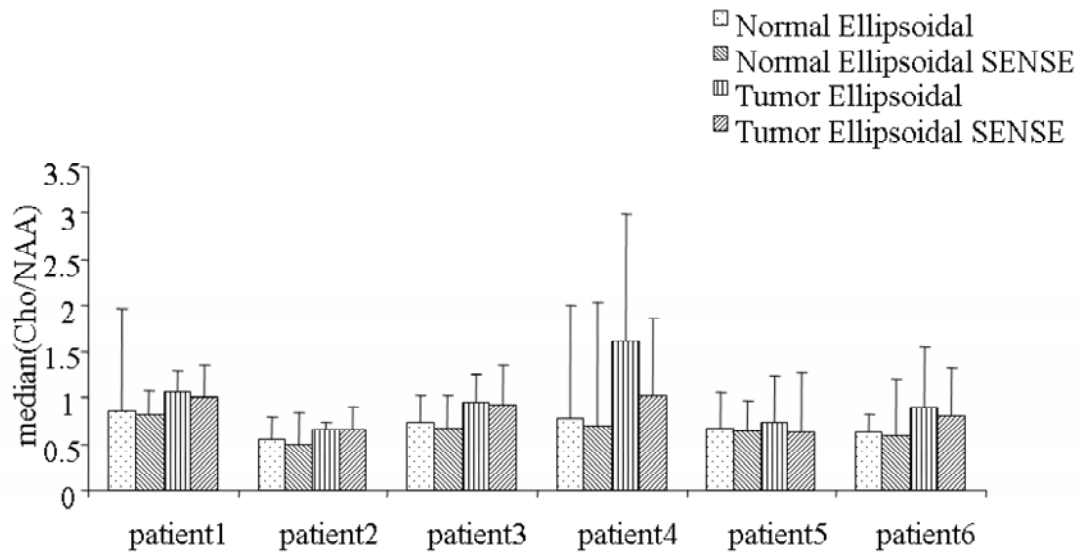


Figure 7.2. Median Cho to NAA ratio for the patients within normal and tumor regions as calculated from ellipsoidal and ellipsoidal SENSE spectra.

Figure 7.3 shows a slice of the T2-weighted FLAIR images of a volunteer along with the PRESS box selection (white) and the ellipsoidal and ellipsoidal SENSE

spectra from the black grid. Both spectra display a spectral pattern of a healthy brain and they were highly correlated ($r = 0.88, p < 0.001$).

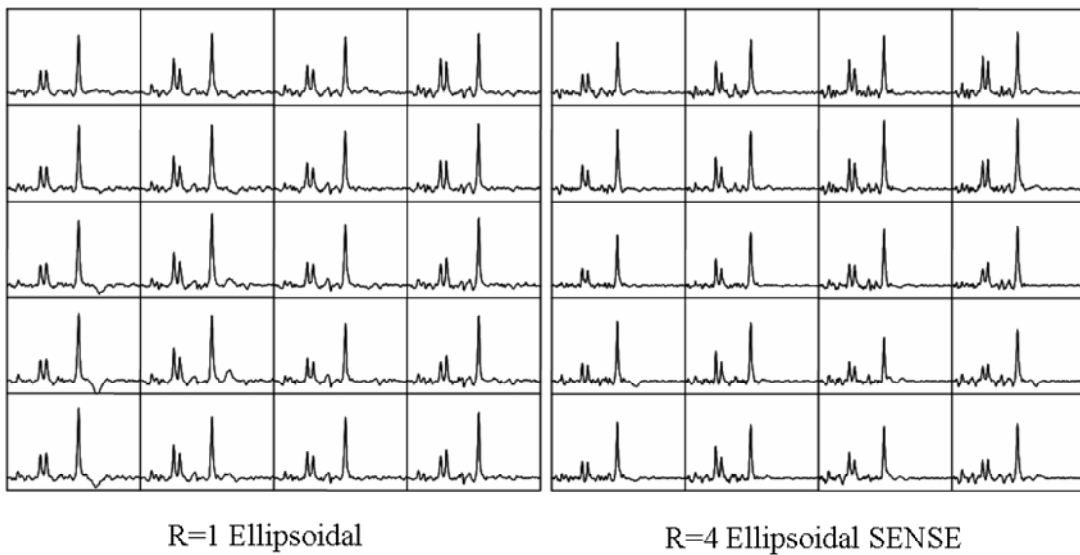
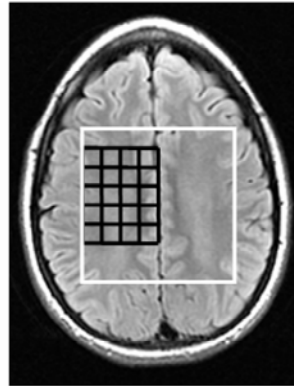


Figure 7.3. Ellipsoidal and acquired ellipsoidal SENSE spectra from the black grid on the T2-weighted FLAIR image of a volunteer are shown at the bottom left and right, respectively.

Figure 7.4 displays ellipsoidal SENSE and ellipsoidal spectra from a patient diagnosed with glioblastoma multiforme, where both ellipsoidal SENSE and ellipsoidal spectra depict the tumor region with high Cho and low NAA clearly and they were highly correlated ($r = 0.86, p < 0.001$).

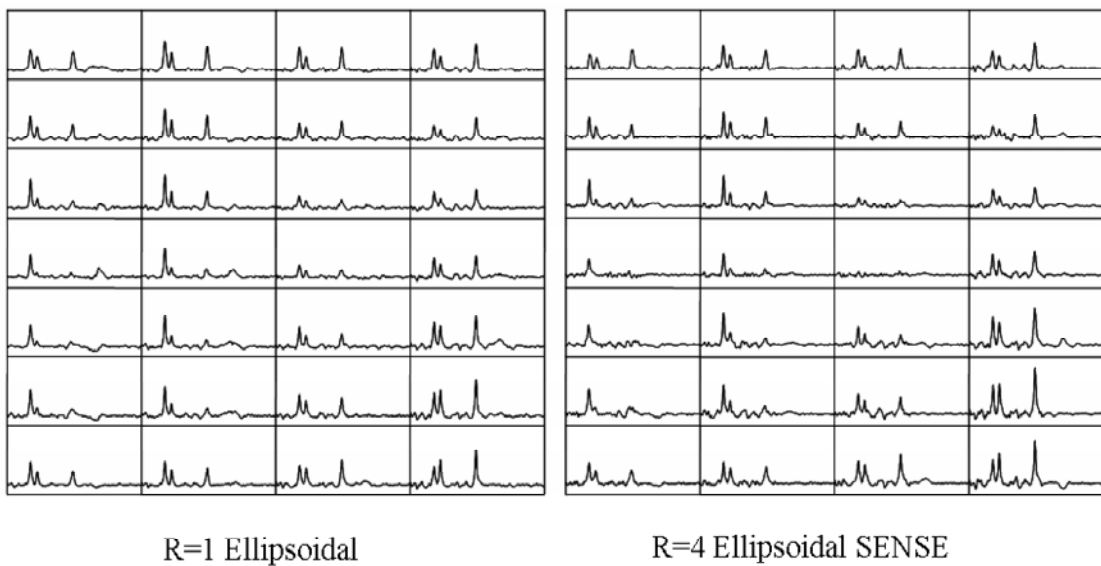
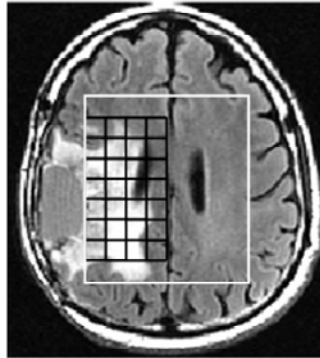


Figure 7.4. 53 years old male patient diagnosed with glioblastoma multiforme. T2 weighted FLAIR image is shown on the top. Ellipsoidal and ellipsoidal SENSE spectra from the black grid are shown at the bottom left and right, respectively.

Discussion

Ellipsoidal SENSE MRSI was implemented for imaging gliomas in less than 5 minutes with an effective 9 fold reduction in scan time at 3T. The peak height ratio results of ellipsoidal SENSE spectra were highly correlated with the clinically accepted ellipsoidal spectra. Both ellipsoidal SENSE and ellipsoidal spectra resulted in

similar spectral patterns over the PRESS box and had the ability to distinguish tumor regions from normal regions for this limited patient population.

Tikhonov's simple regularized inversion conditioned the SENSE matrix inversion, and resulted in lower geometry factors and subsequently higher SNR. The addition of regularization to the data reconstruction also reduced the residual lipid contamination in the spectra, while it did not significantly affect the metabolite intensities.

The ellipsoidal SENSE spectra had high signal to noise ratio resulting in high quality and clinically interpretable spectra. However, one parameter affecting the high SNR was the point spread function effect of the ellipsoidal sampling which reduced the spatial resolution. Our previous results indicated a 2.2-2.5 fold spatial resolution loss for the ellipsoidal spectra, while the spatial resolution was same for the SENSE spectra in comparison to full sampling {Ozturk-Isik, 2006 #185}. Ellipsoidal SENSE spectra suffered from a similar spatial resolution loss as the ellipsoidal spectra.

In conclusion, ellipsoidal SENSE k -space sampling reduced the scan time from 37:42 min to 4:36 min for a 16x16x8 array. Reduced scan time can enable multiple spectral scans in a single patient visit. For example, additional short TE spectra can be acquired for the quantification of short T2 brain metabolites like glutamate and myoinositol. Faster MRSI techniques are expected to reduce the patient discomfort and motion artifacts while increasing the MR scanner throughput.

8 . Summary

The goals of this dissertation were to characterize the spatial heterogeneity of gliomas using MR spectroscopic and diffusion imaging techniques, to generate a post-processing algorithm to reduce the amount of lipid contamination in MR spectra, and to develop new means of acquiring and reconstructing faster MR spectroscopic data.

This thesis first evaluated the spatial heterogeneity and correlations of spectroscopic and diffusion parameters in contrast enhancing, T2 hyperintense and metabolically abnormal areas in treatment naïve grade 3 glioma patients. According to the spectral and diffusion parameters, the contrast enhancement appeared to be the most malignant component of the grade 3 gliomas. However, only eighteen of the thirty-two patients studied had contrast enhancement. In patients with non-enhancing lesions, thirteen of the fourteen showed an abnormality with $CNI \geq 2$ and twelve of these thirteen patients had metabolically abnormal regions with $CNI \geq 4$. These regions reflected similar metabolic and diffusion characteristics as the contrast enhancement, indicating that $CNI \geq 4$ may be the most malignant part of the tumor in non-enhancing patients. Intermediate CNI levels appeared to be regions where normal brain function and structure was compromised but which had only moderate tumor activity. The results of the study suggested that MRSI and diffusion parameters provide complimentary information that may be valuable for characterizing different parts of the anatomic lesion. Treatment planning can also be improved using the results of this study especially for non-enhancing patients, where the spectroscopic imaging can delineate a more specific target than the T2-weighted images.

This thesis also consisted of the development of a post-processing method for unaliasing lipid resonances originating from in-slice subcutaneous lipids from the MR spectroscopic data of gliomas using an eight channel phased-array coil and the sensitivity encoding method at 3T. The lipid peaks that appear in the spectra might be due to the cell membrane breakdown, or a data acquisition artifact that would misrepresent the location of the subcutaneous lipid. The lipid unaliasing algorithm was effective in partially removing aliased lipid peaks for simulated and empirical data and only required 2-3 minutes of processing time on a Sun Blade Workstation. This technique detected aliasing problems and resolved only the aliasing lipids without affecting the other metabolites resonating at similar frequencies, especially lactate. Additionally, resident lipids that may be of biological importance would not be affected by this algorithm. The removal of aliasing lipid peaks can enable better spectroscopic quantification while using frequency domain methods.

The main limitation of acquiring the MRSI data for patients is the long data acquisition time. A current approach for faster MRSI data acquisition is to limit the data acquisition to a central ellipsoidal portion of k -space. For this thesis, a SENSE acquisition and reconstruction for spectroscopic imaging of gliomas was implemented to reduce the scan time by a factor of four. The SNR and metabolite intensity distributions of SENSE MRSI were compared with the fully or ellipsoidally sampled spectra in tumor and normal regions. Our results suggested that SENSE MRSI produced clinically interpretable and good quality spectra within less than 10 minutes scan time, and its results were highly correlated with the ellipsoidally sampled spectra. The nominal spatial resolution of SENSE spectra was also calculated to be same with

the full spectra, while ellipsoidal spectra acquired within the same scan time suffered from a 2.5-fold spatial resolution loss due to the PSF effect of the sampling.

This work next investigated the feasibility of reducing the data acquisition time further by combining ellipsoidal sampling with two parallel imaging techniques, SENSE and GRAPPA. The results of this study showed that both simulated SENSE and GRAPPA ellipsoidal spectra resulted in similar spectral patterns over the PRESS box with the original ellipsoidal spectra. The Cho/NAA ratios calculated from the GRAPPA and SENSE ellipsoidal spectra were highly correlated with that of the original ellipsoidal spectra. The SENSE spectra were observed to have a higher lipid artifact than the GRAPPA spectra due to imperfect unaliasing. However, there was a higher intensity variation across the slices for GRAPPA than SENSE ellipsoidal spectra, which resulted in lower intensities around the cavities of tumors in the GRAPPA spectra. Both SENSE and GRAPPA ellipsoidal spectra resulted in a significant reduction in scan time which would alleviate patient discomfort.

In the last part of this thesis, ellipsoidal SENSE MRSI data acquisition and reconstruction were implemented for small field of view spectral imaging of gliomas at 3T, and was quantitatively compared to spectra acquired with ellipsoidal k -space sampling. The ellipsoidal SENSE method drastically reduced the spectral scan time from 37:42 min (full sampling) by nine fold to 4:36 min in comparison to much longer clinically accepted ellipsoidal sampling (17:32 min) for a 16x16x8 array. The results indicated that both ellipsoidal SENSE and original ellipsoidal k -space spectra resulted in similar spectral patterns over the PRESS box that were highly correlated. The ellipsoidal SENSE spectra had distinguishable tumor and normal spectra similarly to

the ellipsoidal spectra. The scan time was less than five minutes for this technique, which would result in much less patient discomfort and motion artifacts. The scanner throughput would also be improved by scanning each patient faster. It would also be possible to acquire multiple spectra with different echo times within reasonable scan times.

The main disadvantage of fast MRSI data acquisition is the loss of signal to noise ratio. Future work will investigate the application of parallel imaging theories at higher field strength of 7T, which would enable higher SNR and better spectral dispersion. The SENSE based unaliasing methods can also be further improved by optimizing the regularization methods used for the spectral reconstruction. Another area of improvement for SENSE methods can be achieved by reducing the additional aliasing from outside the PRESS box using better signal saturation outside the area of interest. MR spectroscopic imaging is an important tool in brain tumor diagnosis, treatment planning, and monitoring the effects of therapy. The results of this dissertation can be utilized to both improve tumor characterization and acquire more accurate and faster spectroscopic data.

References

1. American Cancer Society. Cancer Facts and Figures 2007. Access Date:18 February 2007.
http://www.cancer.org/docroot/CRI/content/CRI_2_4_1X_What_are_the_key_statistics_for_brain_and_spinal_cord_tumors_3.asp?sitearea=.
2. Ozturk-Isik E, Pirzkall A, Lamborn KR, Chang SM, Nelson SJ. Spatial Characteristics and Correlations of Newly Diagnosed Grade 3 Gliomas Using MRI, 3D MR Spectroscopic Imaging, and Diffusion Tensor Imaging. (In Preparation) 2007.
3. Ozturk-Isik E, Crane JC, Cha S, Chang SM, Berger MS, Nelson SJ. Unaliasing lipid contamination for MR spectroscopic imaging of gliomas at 3T using sensitivity encoding (SENSE). *Magn Reson Med* 2006;55(5):1164-1169.
4. Ozturk-Isik E, Chen AP, Crane J, Xu D, Han E, Vigneron D, Cha S, Chang SM, Nelson S. Quantitative SENSE Spectroscopy of Gliomas at 3T. Proceedings 14th Scientific Meeting, International Society for Magnetic Resonance in Medicine. 2006 May; Seattle. p 1779.
5. Ozturk-Isik E, Chen AP, Crane JC, Xu D, Ha ET, Vigneron DB, Cha S, Chang SM, Nelson SJ. Quantitative 3D SENSE MRSI in Comparison to Ellipsoidal MRSI of Gliomas at 3T. *NMR in Biomedicine* (In Preparation) 2007.
6. Ozturk-Isik E, Banerjee S, Majumdar S, Nelson SJ. Partially Parallel MR Spectroscopic Imaging of Gliomas at 3T. Proceedings of the 28th IEEE EMBS Annual International Conference. 2006 August; New York City, NY.
7. Ozturk-Isik E, Chen AP, Crane JC, Han ET, Xu D, Vigneron DB, Chang SM, Nelson SJ. Elliptical SENSE with Effective 9 Fold Scan Time Reduction for Small FOV 3D MR Spectroscopic Imaging of Glioma Patients at 3T. Proceedings 15th Scientific Meeting, International Society for Magnetic Resonance in Medicine. 2007 May; Berlin, Germany.
8. Ozturk-Isik E, Chen AP, Crane JC, Han ET, Xu D, Vigneron DB, Chang SM, Nelson SJ. Ellipsoidal SENSE with Effective Nine-Fold Scan Time Reduction for Small FOV 3D MR Spectroscopic Imaging of Patients with Glioma at 3T. *Journal of Magnetic Resonance Imaging* (In Preparation) 2007.

9. Canadian Institutes of Health Research: Institute of Neurosciences, Mental Health and Addiction. The Brain From Top to Bottom: Anatomy and Function. Access Date: December 7, 2006. http://thebrain.mcgill.ca/flash/a/a_01/a_01_cr/a_01_cr_ana/a_01_cr_ana.html.
10. Afifi AK, Bergman RA. Functional Neuroanatomy: Text and Atlas. Hefta J, Melvin S, editors. New York: McGraw-Hill; 1998. 730 p.
11. Norden AD, Wen PY. Glioma therapy in adults. *Neurologist* 2006;12(6):279-292.
12. Liang ZP, Lauterbur PC. Principles of Magnetic Resonance Imaging, A Signal Processing Perspective. Akay M, editor. New York, NY: IEEE Press; 2000. 416 p.
13. Nishimura DW. Principles of Magnetic Resonance Imaging. Nishimura DW, editor. Palo Alto, CA: Stanford University; 2002. 223 p.
14. Haacke EM, Brown RW, Thompson MR, Venkatesan R. Magnetic Resonance Imaging - Physical Principles and Sequence Design. New York, NY: John Wiley & Sons Inc.; 1999. 914 p.
15. Wansapura JP, Holland SK, Dunn RS, Ball WS, Jr. NMR relaxation times in the human brain at 3.0 tesla. *J Magn Reson Imaging* 1999;9(4):531-538.
16. Whittall KP, MacKay AL, Graeb DA, Nugent RA, Li DK, Paty DW. In vivo measurement of T2 distributions and water contents in normal human brain. *Magn Reson Med* 1997;37(1):34-43.
17. Stanisz GJ, Odobina EE, Pun J, Escaravage M, Graham SJ, Bronskill MJ, Henkelman RM. T1, T2 relaxation and magnetization transfer in tissue at 3T. *Magn Reson Med* 2005;54(3):507-512.
18. Mlynarik V, Gruber S, Moser E. Proton T (1) and T (2) relaxation times of human brain metabolites at 3 Tesla. *NMR Biomed* 2001;14(5):325-331.
19. Elster AD, Burdette JH. Questions and Answers in Magnetic Resonance Imaging. Gailard J, editor. St. Louis, MO: Mosby Inc.; 2001. 333 p.

20. Nelson SJ. Multivoxel magnetic resonance spectroscopy of brain tumors. *Mol Cancer Ther* 2003;2(5):497-507.
21. Nelson SJ, McKnight TR, Henry RG. Characterization of untreated gliomas by magnetic resonance spectroscopic imaging. *Neuroimaging Clin N Am* 2002;12(4):599-613.
22. Pirzkall A, Li X, Oh J, Chang S, Berger MS, Larson DA, Verhey LJ, Dillon WP, Nelson SJ. 3D MRSI for resected high-grade gliomas before RT: tumor extent according to metabolic activity in relation to MRI. *Int J Radiat Oncol Biol Phys* 2004;59(1):126-137.
23. Vigneron D, Bollen A, McDermott M, Wald L, Day M, Moyher-Noworolski S, Henry R, Chang S, Berger M, Dillon W, Nelson S. Three-dimensional magnetic resonance spectroscopic imaging of histologically confirmed brain tumors. *Magn Reson Imaging* 2001;19(1):89-101.
24. Li X, Lu Y, Pirzkall A, McKnight T, Nelson SJ. Analysis of the spatial characteristics of metabolic abnormalities in newly diagnosed glioma patients. *J Magn Reson Imaging* 2002;16(3):229-237.
25. Dowling C, Bollen AW, Noworolski SM, McDermott MW, Barbaro NM, Day MR, Henry RG, Chang SM, Dillon WP, Nelson SJ, Vigneron DB. Preoperative proton MR spectroscopic imaging of brain tumors: correlation with histopathologic analysis of resection specimens. *AJNR Am J Neuroradiol* 2001;22(4):604-612.
26. Chan AA, Lau A, Pirzkall A, Chang SM, Verhey LJ, Larson D, McDermott MW, Dillon WP, Nelson SJ. Proton magnetic resonance spectroscopy imaging in the evaluation of patients undergoing gamma knife surgery for Grade IV glioma. *J Neurosurg* 2004;101(3):467-475.
27. Li X, Jin H, Lu Y, Oh J, Chang S, Nelson SJ. Identification of MRI and 1H MRSI parameters that may predict survival for patients with malignant gliomas. *NMR Biomed* 2004;17(1):10-20.
28. Graves EE, Nelson SJ, Vigneron DB, Verhey L, McDermott M, Larson D, Chang S, Prados MD, Dillon WP. Serial proton MR spectroscopic imaging of recurrent malignant gliomas after gamma knife radiosurgery. *AJNR Am J Neuroradiol* 2001;22(4):613-624.

29. McKnight TR, Noworolski SM, Vigneron DB, Nelson SJ. An automated technique for the quantitative assessment of 3D-MRSI data from patients with glioma. *J Magn Reson Imaging* 2001;13(2):167-177.
30. Graves EE, Nelson SJ, Vigneron DB, Chin C, Verhey L, McDermott M, Larson D, Sneed PK, Chang S, Prados MD, Lamborn K, Dillon WP. A preliminary study of the prognostic value of proton magnetic resonance spectroscopic imaging in gamma knife radiosurgery of recurrent malignant gliomas. *Neurosurgery* 2000;46(2):319-326; discussion 326-318.
31. Graves EE, Pirzkall A, Nelson SJ, Larson D, Verhey L. Registration of magnetic resonance spectroscopic imaging to computed tomography for radiotherapy treatment planning. *Med Phys* 2001;28(12):2489-2496.
32. Nelson SJ, Graves E, Pirzkall A, Li X, Antiniw Chan A, Vigneron DB, McKnight TR. In vivo molecular imaging for planning radiation therapy of gliomas: an application of 1H MRSI. *J Magn Reson Imaging* 2002;16(4):464-476.
33. Pirzkall A, McKnight TR, Graves EE, Carol MP, Sneed PK, Wara WW, Nelson SJ, Verhey LJ, Larson DA. MR-spectroscopy guided target delineation for high-grade gliomas. *Int J Radiat Oncol Biol Phys* 2001;50(4):915-928.
34. Pirzkall A, Nelson SJ, McKnight TR, Takahashi MM, Li X, Graves EE, Verhey LJ, Wara WW, Larson DA, Sneed PK. Metabolic imaging of low-grade gliomas with three-dimensional magnetic resonance spectroscopy. *Int J Radiat Oncol Biol Phys* 2002;53(5):1254-1264.
35. Nelson SJ, Huhn S, Vigneron DB, Day MR, Wald LL, Prados M, Chang S, Gutin PH, Sneed PK, Verhey L, Hawkins RA, Dillon WP. Volume MRI and MRSI techniques for the quantitation of treatment response in brain tumors: presentation of a detailed case study. *J Magn Reson Imaging* 1997;7(6):1146-1152.
36. Nelson SJ. Imaging of brain tumors after therapy. *Neuroimaging Clin N Am* 1999;9(4):801-819.
37. Nelson SJ, Vigneron DB, Dillon WP. Serial evaluation of patients with brain tumors using volume MRI and 3D 1H MRSI. *NMR Biomed* 1999;12(3):123-138.

38. Wald LL, Nelson SJ, Day MR, Noworolski SE, Henry RG, Huhn SL, Chang S, Prados MD, Sneed PK, Larson DA, Wara WM, McDermott M, Dillon WP, Gutin PH, Vigneron DB. Serial proton magnetic resonance spectroscopy imaging of glioblastoma multiforme after brachytherapy. *J Neurosurg* 1997;87(4):525-534.
39. Pavia DL, Lampman GM, Kriz GS. *Introduction to Spectroscopy*. Bellingham, Washington: Brooks/Cole; 2001. 579 p.
40. Salibi N, Brown MA. *Clinical MR Spectroscopy: First Principles*. New York, NY: Wiley-Liss, Inc.; 1998. 220 p.
41. Bottomley PA. Spatial localization in NMR spectroscopy in vivo. *Ann N Y Acad Sci* 1987;508:333-348.
42. Haase A, Frahm J, Hanicke W, Matthaei D. ^1H NMR chemical shift selective (CHESS) imaging. *Phys Med Biol* 1985;30(4):341-344.
43. Star-Lack J, Vigneron DB, Pauly J, Kurhanewicz J, Nelson SJ. Improved solvent suppression and increased spatial excitation bandwidths for three-dimensional PRESS CSI using phase-compensating spectral/spatial spin-echo pulses. *J Magn Reson Imaging* 1997;7(4):745-757.
44. Tran TK, Vigneron DB, Sailasuta N, Tropp J, Le Roux P, Kurhanewicz J, Nelson S, Hurd R. Very selective suppression pulses for clinical MRSI studies of brain and prostate cancer. *Magn Reson Med* 2000;43(1):23-33.
45. Star-Lack J, Nelson SJ, Kurhanewicz J, Huang LR, Vigneron DB. Improved water and lipid suppression for 3D PRESS CSI using RF band selective inversion with gradient dephasing (BASING). *Magn Reson Med* 1997;38(2):311-321.
46. Star-Lack J, Spielman D, Adalsteinsson E, Kurhanewicz J, Terris DJ, Vigneron DB. In vivo lactate editing with simultaneous detection of choline, creatine, NAA, and lipid singlets at 1.5 T using PRESS excitation with applications to the study of brain and head and neck tumors. *J Magn Reson* 1998;133(2):243-254.

47. Nelson SJ. Analysis of volume MRI and MR spectroscopic imaging data for the evaluation of patients with brain tumors. *Magn Reson Med* 2001;46(2):228-239.
48. Dehais C, Laigle-Donadey F, Marie Y, Kujas M, Lejeune J, Benouaich-Amiel A, Pedretti M, Polivka M, Xuan KH, Thillet J, Delattre JY, Sanson M. Prognostic stratification of patients with anaplastic gliomas according to genetic profile. *Cancer* 2006;107(8):1891-1897.
49. Catalaa I, Henry R, Dillon WP, Graves EE, McKnight TR, Lu Y, Vigneron DB, Nelson SJ. Perfusion, diffusion and spectroscopy values in newly diagnosed cerebral gliomas. *NMR Biomed* 2006;19(4):463-475.
50. Bassler PJ, Pierpaoli C. A simplified method to measure the diffusion tensor from seven MR images. *Magn Reson Med* 1998;39(6):928-934.
51. Oh J, Cha S, Aiken AH, Han ET, Crane JC, Stainsby JA, Wright GA, Dillon WP, Nelson SJ. Quantitative apparent diffusion coefficients and T2 relaxation times in characterizing contrast enhancing brain tumors and regions of peritumoral edema. *J Magn Reson Imaging* 2005;21(6):701-708.
52. Bulakbasi N, Guvenc I, Onguru O, Erdogan E, Tayfun C, Ucoz T. The added value of the apparent diffusion coefficient calculation to magnetic resonance imaging in the differentiation and grading of malignant brain tumors. *J Comput Assist Tomogr* 2004;28(6):735-746.
53. Provenzale JM, McGraw P, Mhatre P, Guo AC, Delong D. Peritumoral brain regions in gliomas and meningiomas: investigation with isotropic diffusion-weighted MR imaging and diffusion-tensor MR imaging. *Radiology* 2004;232(2):451-460.
54. Lu S, Ahn D, Johnson G, Law M, Zagzag D, Grossman RI. Diffusion-tensor MR imaging of intracranial neoplasia and associated peritumoral edema: introduction of the tumor infiltration index. *Radiology* 2004;232(1):221-228.
55. Tsuchiya K, Fujikawa A, Nakajima M, Honya K. Differentiation between solitary brain metastasis and high-grade glioma by diffusion tensor imaging. *Br J Radiol* 2005;78(930):533-537.

56. van Westen D, Latt J, Englund E, Brockstedt S, Larsson EM. Tumor extension in high-grade gliomas assessed with diffusion magnetic resonance imaging: values and lesion-to-brain ratios of apparent diffusion coefficient and fractional anisotropy. *Acta Radiol* 2006;47(3):311-319.
57. Goebell E, Fiehler J, Ding XQ, Paustenbach S, Nietz S, Heese O, Kucinski T, Hagel C, Westphal M, Zeumer H. Disarrangement of fiber tracts and decline of neuronal density correlate in glioma patients--a combined diffusion tensor imaging and 1H-MR spectroscopy study. *AJNR Am J Neuroradiol* 2006;27(7):1426-1431.
58. Calvar JA, Meli FJ, Romero C, Calcagno ML, Yanez P, Martinez AR, Lambre H, Taratuto AL, Sevlever G. Characterization of brain tumors by MRS, DWI and Ki-67 labeling index. *J Neurooncol* 2005;72(3):273-280.
59. Gupta RK, Cloughesy TF, Sinha U, Garakian J, Lazareff J, Rubino G, Rubino L, Becker DP, Vinters HV, Alger JR. Relationships between choline magnetic resonance spectroscopy, apparent diffusion coefficient and quantitative histopathology in human glioma. *J Neurooncol* 2000;50(3):215-226.
60. Kono K, Inoue Y, Nakayama K, Shakudo M, Morino M, Ohata K, Wakasa K, Yamada R. The role of diffusion-weighted imaging in patients with brain tumors. *AJNR Am J Neuroradiol* 2001;22(6):1081-1088.
61. Stadlbauer A, Ganslandt O, Buslei R, Hammen T, Gruber S, Moser E, Buchfelder M, Salomonowitz E, Nimsky C. Gliomas: histopathologic evaluation of changes in directionality and magnitude of water diffusion at diffusion-tensor MR imaging. *Radiology* 2006;240(3):803-810.
62. Gupta RK, Sinha U, Cloughesy TF, Alger JR. Inverse correlation between choline magnetic resonance spectroscopy signal intensity and the apparent diffusion coefficient in human glioma. *Magn Reson Med* 1999;41(1):2-7.
63. McKnight T, Love T, Lamborn K, Berger M, Chang S, Dillon W, Bollen A, Nelson S. Correlation of MR spectroscopic and growth characteristics of Grades II and III glioma. *Journal of Neurosurgery* 2006.
64. Zamecnik J. The extracellular space and matrix of gliomas. *Acta Neuropathol (Berl)* 2005;110(5):435-442.

65. Spielman DM, Pauly JM, Macovski A, Glover GH, Enzmann DR. Lipid-suppressed single- and multisection proton spectroscopic imaging of the human brain. *J Magn Reson Imaging* 1992;2(3):253-262.
66. Adalsteinsson E, Star-Lack J, Meyer CH, Spielman DM. Reduced spatial side lobes in chemical-shift imaging. *Magn Reson Med* 1999;42(2):314-323.
67. Ebel A, Maudsley AA. Comparison of methods for reduction of lipid contamination for in vivo proton MR spectroscopic imaging of the brain. *Magn Reson Med* 2001;46(4):706-712.
68. Star-Lack JM, Adalsteinsson E, Gold GE, Ikeda DM, Spielman DM. Motion correction and lipid suppression for 1H magnetic resonance spectroscopy. *Magn Reson Med* 2000;43(3):325-330.
69. de Beer R, Michels F, van Ormondt D, van Tongeren BP, Luyten PR, van Vroonhoven H. Reduced lipid contamination in in vivo 1H MRSI using time-domain fitting and neural network classification. *Magn Reson Imaging* 1993;11(7):1019-1026.
70. Haupt CI, Schuff N, Weiner MW, Maudsley AA. Removal of lipid artifacts in 1H spectroscopic imaging by data extrapolation. *Magn Reson Med* 1996;35(5):678-687.
71. Pruessmann KP, Weiger M, Scheidegger MB, Boesiger P. SENSE: sensitivity encoding for fast MRI. *Magn Reson Med* 1999;42(5):952-962.
72. Weiger M, Pruessmann KP, Leussler C, Roschmann P, Boesiger P. Specific coil design for SENSE: a six-element cardiac array. *Magn Reson Med* 2001;45(3):495-504.
73. Dydak U, Weiger M, Pruessmann KP, Meier D, Boesiger P. Sensitivity-encoded spectroscopic imaging. *Magn Reson Med* 2001;46(4):713-722.
74. Winkelmann R, Bornert P, Nehrke K, Dossel O. Efficient foldover suppression using SENSE. *Magma* 2004.
75. Kellman P, McVeigh ER. Ghost artifact cancellation using phased array processing. *Magn Reson Med* 2001;46(2):335-343.

76. Roemer PB, Edelstein WA, Hayes CE, Souza SP, Mueller OM. The NMR phased array. *Magn Reson Med* 1990;16(2):192-225.
77. Lin FH, Kwong KK, Belliveau JW, Wald LL. Parallel imaging reconstruction using automatic regularization. *Magn Reson Med* 2004;51(3):559-567.
78. Bertero M, Boccacci P. *Introduction to Inverse Problems in Imaging*. Bristol and Philadelphia: IOP Publishing Ltd; 1998. 351 p.
79. Griswold MA, Kannengiesser S, Heidemann RM, Wang J, Jakob PM. Field-of-view limitations in parallel imaging. *Magn Reson Med* 2004;52(5):1118-1126.
80. Li X, Vigneron DB, Cha S, Graves EE, Crawford F, Chang SM, Nelson SJ. Relationship of MR-derived lactate, mobile lipids, and relative blood volume for gliomas in vivo. *AJNR Am J Neuroradiol* 2005;26(4):760-769.
81. Saraswathy S, Crawford F, Nelson S. Semi-automated segmentation of brain tumor lesions in MR Images. *Proceedings 14th Scientific Meeting, International Society for Magnetic Resonance in Medicine*. 2006 May; Seattle. p 1609.
82. Li Y, Osorio JA, Ozturk-Isik E, Chen AP, Xu D, Crane JC, Cha S, Chang S, Berger MS, Vigneron DB, Nelson SJ. Considerations in applying 3D PRESS H-1 brain MRSI with an eight-channel phased-array coil at 3 T. *Magn Reson Imaging* 2006;24(10):1295-1302.
83. Griswold MA, Jakob PM, Heidemann RM, Nittka M, Jellus V, Wang J, Kiefer B, Haase A. Generalized autocalibrating partially parallel acquisitions (GRAPPA). *Magn Reson Med* 2002;47(6):1202-1210.
84. Wang Z, Wang J, Detre JA. Improved data reconstruction method for GRAPPA. *Magn Reson Med* 2005;54(3):738-742.
85. Posse S, Tedeschi G, Risinger R, Ogg R, Le Bihan D. High speed 1H spectroscopic imaging in human brain by echo planar spatial-spectral encoding. *Magn Reson Med* 1995;33(1):34-40.

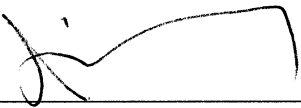
86. Adalsteinsson E, Irarrazabal P, Topp S, Meyer C, Macovski A, Spielman DM. Volumetric spectroscopic imaging with spiral-based k-space trajectories. *Magn Reson Med* 1998;39(6):889-898.
87. Lin FH, Tsai SY, Otazo R, Caprihan A, Wald LL, Belliveau JW, Posse S. Sensitivity-encoded (SENSE) proton echo-planar spectroscopic imaging (PEPSI) in the human brain. *Magn Reson Med* 2007;57(2):249-257.

Publishing Agreement

It is the policy of the University to encourage the distribution of all theses and dissertations. Copies of all UCSF theses and dissertations will be routed to the library via the Graduate Division. The library will make all theses and dissertations accessible to the public and will preserve these to the best of their abilities, in perpetuity.

Please sign the following statement:

I hereby grant permission to the Graduate Division of the University of California, San Francisco to release copies of my thesis or dissertation to the Campus Library to provide access and preservation, in whole or in part, in perpetuity.



Author Signature

03/23/07

Date